Universidad de Huelva

Departamento de Física Aplicada

Computer simulation of the phase diagram of Gaussian overlap models

Memoria para optar al grado de doctora
presentada por:

Ramona Georgeta Marguta

Fecha de lectura: 30 de enero de 2009

Bajo la dirección de los doctores:

Enrique de Miguel Agustino
Elvira Martín del Río

Huelva, 2009

ISBN: 978-84-92679-94-2
D.L.: H 98-2009

UNIVERSIDAD DE HUELVA

COMPUTER SIMULATION OF THE PHASE DIAGRAM OF GAUSSIAN OVERLAP MODELS

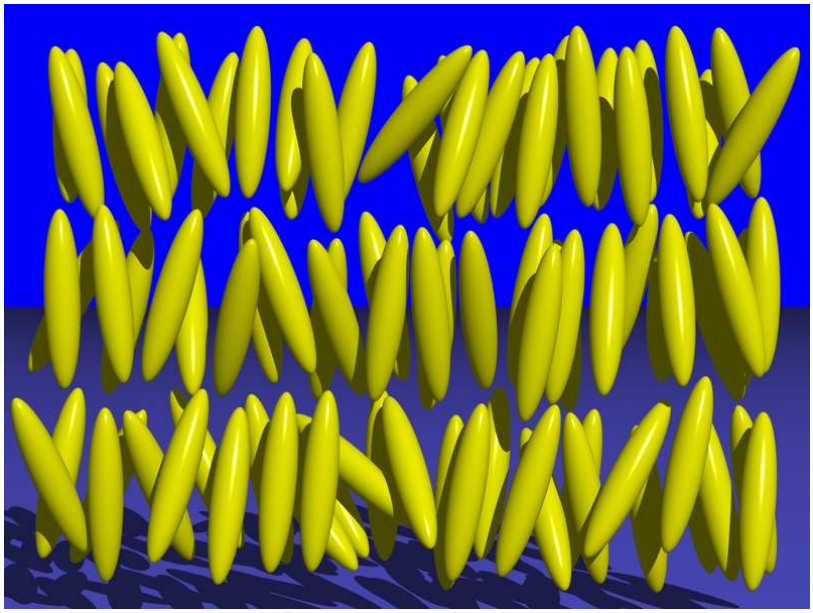

Ramona Georgeta Mărguţă

UNIVERSIDAD DE HUELVA

COMPUTER SIMULATION OF THE PHASE DIAGRAM OF GAUSSIAN OVERLAP MODELS

Memoria presentada por
Ramona Georgeta Mărguţă

al
Departamento de Física Aplicada de la
Universidad de Huelva
para optar al grado de Doctor en Ingeníeria Ambiental

Directores
Dr. Enrique de Miguel Agustino
Dr. Elvira Martín del Río

Huelva, Noviembre 2008

Agradecimientos

En primer lugar, quisiera expresar mi agradecimiento y gratitud a los directores de esta tesis, Enrique de Miguel Agustino y Elvira Martín del Río por guiar mis pasos en el tumultuoso camino de la simulación, por su apoyo constante y su comprensión.

Agradezco a mi familia por apoyarme en mi decisión de venir a España y por darme ánimo constantemente.

A Felipe Jimenez Blas por haber sido mi puente hacia el complicado mundo del Linux, espero no haberle causado demasiadas molestias.

A todos y cada uno de mis amigos de la sala de becarios de la cuarta planta del Departamento de Física Aplicada por ayudarme a mejorar mi español, por hacer agradables y relajantes las horas de trabajo.

A mis amigas y amigos (antiguos y mas nuevos) de España y del otro lado del Atlántico, por devolverme a la realidad cada vez que la preocupación se adueñaba de mi.

A los profesores y amigos del Departamento de Física Aplicada por hacer mas fácil mi integración en el Departamento.

Agradezco a la Universidad de Huelva por la concesión de una beca de investigación dentro del Plan Propio de Investigación. El trabajo realizado ha sido financiado por el proyecto de investigación FIS2004-06627-C0-01 de la Dirección General de Investigación (Ministerio de Educación y Ciencia).

Contents

Chapter 1

Introduction

Computer simulation is midway between experimental and theoretical approaches of condensed matter. The aim of a theory is to predict the properties of a system considering the interactions between molecules. However, these molecular interactions need to be modelled in some way. Computer simulation offers the appropriate framework to test the reliability of a molecular model. The aim of computer simulation is to obtain the static and dynamic equilibrium properties of the model system [1]. Two types of simulations are commonly used: Monte Carlo (MC), which involves sampling configurations of the system in phase space, and molecular dynamics (MD), based on following the time evolution of the system. In this work, only MC techniques will be used.

Since the first simulation of a liquid, carried out at the Los Alamos National laboratories [2], computer simulation has proved to be a very useful tool in understanting the physical phenomena occurring in atomic and molecular systems. Furthermore, it offers the possibility to investigate the system under temperatures and pressures which are not accessible in experiment, or to study the behaviour of the system under artificially modified Hamiltonians. The first works in this field focused on simulations of atomic systems in which the particles interact through an spherically symmetric potential [3]. Most of these simulations were performed for systems of hard spheres. In spite of being a highly idealized model potential, it has proved useful for investigating general properties of simple systems [4]. Simulations of more complex, molecular systems helped to gain insight into the ordering phenomena characteristic of some compounds named liquid crystals.

The term liquid crystal designates a state of matter that is intermediate between the liquid phase and the crystalline solid. Liquid crystals flow like ordinary liquids but also exhibit anisotropic properties as solid crystals do. In

all liquid crystal phases the molecules diffuse like in fluids but they maintain some degree of orientational and sometimes positional order also [5]. The amount of order in liquid crystals is smaller than in crystals. Molecules that form liquid crystals are usually characterized by the fact that the building blocks are anisotropic [6]. They exhibit a complex phase diagram as they are heated from the solid:

- both types of order (orientational and positional) are lost at the same time. The resulting phase is an isotropic molecular liquid;
- only the orientational order is lost. The resulting phase is called plastic solid;
- the positional order disappears, fully or partially, while some degree of orientational order survives. The resulting phase is a liquid crystal.

Liquid crystals obtained by purely thermal processes are called thermotropic liquid crystals. They have been classified by Friedel in 1922 as nematics, cholesterics, and smectics. In the **nematic** liquid crystals the long molecular axes are (on average) paralel to a preferred direction **n** (named director of the phase), see Fig. 1. There is no positional order, as the centers of mass of the molecules are randomly distributed. Owing to this property, nematics are characterized by fluidity. The name comes from the Greek word for thread, since in a polarising microscope there are often many dark lines visible in thick film samples. These lines are deffects in the orientational order and are called disclinations [5]. **Cholesteric** liquid crystals can be described as twisted nematics. The molecules are parallel to the director of the phase, as in the nematic phase, but when proceeding in a direction normal to the plane, **n** rotates continuously resulting in an helical structure. This structure is characterized by the pitch which defines the distance necessary to rotate **n** by 2π when proceeding along the director. **Smectic** liquid crystals are denominated by A, B, C, ... etc. They are characterized by the fact that the centers of mass of the molecules are arranged in layers. The long molecular axes are parallel to the director, as in the nematic phase, which can be normal to the plane or tilted by a certain angle. The arrangement of the centers of mass within the planes can be random or regular. In the smectic A (SmA) phase, there is no positional order within the layers and the director is perpendicular to the smectic layers. This is schematically shown in Fig. 2. The smectic C (SmC) phase is similar, but the director and the normal to the layers do not coincide. The smectic B (SmB) phase is more ordered than the SmA phase. The constituent molecules adopt a hexagonal ordering inside the layers but these hexagonal lattices do not exhibit long-range positional order.

Figure 1.1: Schematic representation of the nematic phase.

Figure 1.2: Schematic representation of the smectic A phase.

In the last years there have been many studies on liquid crystal materials motivated by the applicability of their anisotropic properties in technology. Liquid crystal phases have been studied theoretically and from computer simulation. Theories used to describe liquid crystal phases are divided in two groups: phenomenological theories due to Landau and de Gennes [7], and molecular theories. The first molecular theory was due to Onsager [8], who assumed that the stabilization of nematic ordering is due to short-range repul-

sive interactions. A second theory due to Maier Saupe [9] states that nematic ordering is due to long-range attractive interactions. In van der Waals [10] type theories both anisotropic hard-core repulsions and angle-dependent attractions are considered to be responsible for the onset of orientational and/or positional order.

As far as computer simulation is concerned, liquid crystalline phases can be simulated using relatively simple hard-core models. Two of the most extensively studied hard-core models are the hard ellipsoid (HE) and the hard spherocylinder (HSC) systems. Frenkel and Mulder [11] have shown that the phase diagram of HEs exhibits plastic solid and nematic phases between the solid and isotropic phases. The plastic phase is stable at small molecular elongations, while the nematic phase is stabilized at relatively high molecular elongations. As for the question if smectic ordering can occur in systems with purely repulsive interactions, the MC simulations of Frenkel [12] demonstrated that a system of HSCs exhibits a smectic-like phase in addition to isotropic, nematic, and solid phases. One should bear in mind that attractive interactions must also be present in real liquid crystals. Simulations including attractive interactions in addition to hard core repulsions have been performed. Whether or not the contribution of the attractive interactions to the stability of liquid crystals is relevant when compared with the repulsive contributions is still an open question. For example, a system of HEs does not promote the formation of the smectic phase, but the addition of an attractive square well to the interactions stabilizes smectic ordering [13].

In spite of the simple (geometric) way in which the repulsive interactions are incorporated in these hard-core models, the corresponding mathematical form of the interactions is far from simple. A more tractable model, from a mathematical and computational point of view, is the so called Gaussian overlap model. This model provides a realistic approach of the anisotropic repulsive part of the interaction potential. A Gaussian distribution function is associated with each molecule. We consider in this work the hard version of the model. The isotropic phase of the hard Gaussian overlap (HGO) model has been previously studied theoretically and from computer simulation [14, 15]. The I–N transition has been recently studied in a range of relatively high molecular elongations [16]. Our aim is to determine the phase diagram of the HGO model from computer simulation. First, we explore the phase behaviour at chosen values of the molecular elongation. We find that, depending on the molecular anisotropy, the system exhibits isotropic, plastic solid, nematic, and solid phases. The plastic solid and nematic phases are not stable for all of the molecular anisotropies. The next step is to determine the range of stability of each phase. At given thermodynamic conditions, the

most stable phase is the one with the lowest free energy. This involves the computation of the free energy of each phase. We select in each case appropriate reference states and compute their free energies by using different techniques. Once the free energy at a reference state point is known, the free energy at any other state point is typically computed from thermodynamic integration methods. The transitions between different phases are located by solving the coexistence conditions: equality of pressure, temperature, and chemical potential. For hard-core models, these conditions amount to the calculation of the pressure at which the Gibbs free energy of both phases become equal. Once the coexistence properties are determined at a particular set of conditions, the full coexistence curve is obtained from the integration of the Clausius-Clapeyron equation (Gibbs-Duhem integration method).

The structure of this thesis is as follows: a detailed overview of the methods used for the computation of the free energy is presented in chapter 2. These methods include thermodynamic integration, parametric integration, expanded ensemble, Einstein crystal, and particle-insertion methods. We present in chapter 3 a computer simulation study of the solid phase of the hard-sphere system. We consider a path at constant density which connects the solid under study with the Einstein crystal. The free energy along this path is computed from simulations in the expanded ensemble. We analyze the effect of system size on the free energy of the solid phase. It is found that the free energy exhibits a strong dependence with system size. Two solid structures, the face-centered cubic (fcc) and hexagonal close-packed (hcp) of the hard-sphere system are studied at a density close to melting. We analyze a possible dependence of the free energy with the shape of the simulation box. The effect of the orientation of the close-packed planes with respect to the simulation box on the free energy is investigated. Chapters 4 and 5 include a thorough study of the HGO model. The coexistence lines between different phases are determined by integration of the Clausius-Clapeyron equation starting from previously determined coexistence points. It is shown that for small molecular elongations the model exhibits isotropic, plastic solid, and solid phases. As the molecular elongation is increased, a nematic phase becomes stable between the isotropic and solid phases. We study in chapter 6 the effect of the attractive interactions on the phase diagram of the HGO model. The attractive interactions are modelled by a square-well potential. It is shown that the main effect is the onset of smectic order. It is found that the smectic phase becomes unstable at sufficiently high pressure and temperature. The range of stability of the nematic phase increases with increasing temperature.

Chapter 2

Methodology

As stated in the Introduction, the main goal of this thesis is to determine the phase diagram of different models of elongated molecules by computer simulation. This is a non-trivial task, mainly due to the fact that it generally (though not always) involves the computation of the free energy of each phase. We give in this chapter a description of the simulation techniques that have been employed to compute the free energy and, hence, to trace the corresponding phase boundaries of two molecular models. We will focus on the study of two molecular models: the hard Gaussian overlap (HGO) model, characterized by purely repulsive intermolecular interactions; and the HGOSW model in which, in addition to the HGO repulsive interactions, attractive interactions described by the square-well potential are considered. In addition to the usual (isotropic) fluid and solid phases, these molecular models may exhibit phases with intermediate order, such as plastic, nematic, and smectic (the latter only when attractive interactions are explicitly considered).

We will give in this chapter a description of simulation techniques, such as thermodynamic integration, parametric integration, expanded ensemble, and particle-insertion, that have been employed to compute the free energy. A description of the Gibbs-Duhem integration method used to construct the full coxistence line, once the coexistence properties at one state point are known, is presented.

2.1 Introduction

In order to determine the phase diagram of a given molecular model one must determine the thermodynamic equilibrium conditions under which the different phases coexist. Two arbitrary phases coexist when the temperature

T, pressure P, and Gibbs free energy of both phases are equal[1]. For the particular case of hard-core models, for which there is no explicit energy scale, the temperature is known to play no role in the thermodynamic description of the system. In this case, the coexistence condition between phases I and II can be written as

$$G_{\mathrm{I}}(P) = G_{\mathrm{II}}(P)\,. \tag{2.1}$$

The solution of this equation yields the coexistence pressure.

According to the coexistence condition embodied in Eq. (2.1), the Gibbs free energy of the two phases must be known. But this is a quantity that, in general, can not be calculated directly in a simulation. In the following, we describe the methods employed in the present work to calculate the free energy of fluid and solid phases. These methods are essentially based on the computation of the free energy difference between the system of interest and a reference system for which the free energy can be computed exactly. Once the free energy of one state point is known, the free energy at any other state pertaining to the same phase can be determined by thermodynamic integration. Finally, one can calculate the coexistence pressure (as well as the rest of transition properties) by imposing the coexistence condition Eq. (2.1). In the case of first-order transitions, the full coexistence line can be traced out using the Gibbs-Duhem integration method once the coexistence properties at one point have been previously determined.

2.2 Monte Carlo simulation

Computer simulation is nowdays one of the most widely used approaches to the study of interacting systems in condensed matter. Excellent reviews on the subject abound in the literature [4, 17, 18]; here, we will highlight the essential features behind Monte Carlo simulation and focuss on those aspects relevant to the present work.

The main goal in a simulation is the calculation of the expected value of macroscopic properties of a simplified model of a many-body interacting system. The interaction model itself is the main input in a simulation. The target properties range from those that are relatively easy to measure in a experiment (i.e., most of the thermodynamic observables), to those which are more difficult to measure in the laboratory (free energy, order parameters, or structural functions).

[1] We are only concerned here with one-component systems. For these type of systems, the condition of equality of the Gibbs free energy is fully equivalent to the condition of equality of the chemical potential.

In a sense, simulation can be regarded as an experiment carried out on the computer, the experiment being performed on a model system that, hopefully, mimics the complex molecular interactions in real systems. This computer experiment can be carried out in different ways. There are two fundamental classes of techniques for implementing a computer simulation: molecular dynamics, which involves following the time evolution of the system; and Monte Carlo (MC), which involves sampling configurations of the system in phase space. The former is closer in spirit to a Newtonian (mechanical) point of view, while the latter follows much closer the realm of Statistical Mechanics. As molecular dynamics has not been used in this project, we will limit ourselves to describe MC techniques.

2.2.1 Computation of ensemble averages

We consider in the following a classical system of N interacting particles defined by a Hamiltonian $\mathcal{H}(\Gamma^p, \Gamma^c) = \mathcal{K}(\Gamma^p) + \mathcal{U}(\Gamma^c)$, where $\mathcal{K}$ and $\mathcal{U}$ are the kinetic and configurational energy, respectively. Here, Γ^p is used as a shorthand notation for all of the translational and angular momenta of the particles, $\Gamma^p \equiv \mathbf{p}^N, \mathbf{J}^N$, where $\mathbf{p}^N = (\mathbf{p}_1, \ldots, \mathbf{p}_N)$, and $\mathbf{J}^N = (\mathbf{J}_1, \ldots, \mathbf{J}_N)$. Similarly, $\Gamma^c \equiv \mathbf{r}^N, \mathbf{\Omega}^N$, with $\mathbf{r}^N = (\mathbf{r}_1, \ldots, \mathbf{r}_N)$, and $\mathbf{\Omega}^N = (\mathbf{\Omega}_1, \ldots, \mathbf{\Omega}_N)$. $\mathbf{r}_i$ specifies the translational coordinates of particle i, and $\mathbf{\Omega}_i$, its orientational coordinates. Any particular realization $\Gamma = \Gamma^p, \Gamma^c$ of the coordinates and momenta of the N particles compatible with the macroscopic constraints of the system constitutes a microstate; the whole set of such microstates define an ensemble, and the corresponding multi-dimensional space is known as the phase space of the system.

The probability density $\rho_{\text{ens}}(\Gamma)$ of finding the system in a particular microstate depends, among other factors, on the macroscopic constraints that define the statistical ensemble. In the canonical ensemble, where the number of particles, volume V, and temperature T are constant, the probability density for a system in equilibrium is given by

$$\rho_{NVT}(\Gamma) = \frac{1}{Q_{NVT}} \exp[-\beta \mathcal{H}(\Gamma)] \,,$$

where β is the inverse temperature, $\beta = (k_{\text{B}} T)^{-1}$, with k_{B} being the Boltzmann constant. Q_{NVT} is the canonical partition function of the system. For a classical system of N identical particles with f degrees of freedom per molecule, Q_{NVT} is explicitly given by

$$Q_{NVT} = \int d\Gamma \exp[-\beta \mathcal{H}(\Gamma)] = \frac{1}{N!} \frac{1}{h^{fN}} \int d\mathbf{r}^N d\mathbf{p}^N d\mathbf{\Omega}^N d\mathbf{J}^N \exp[-\beta \mathcal{H}(\Gamma)] \,, \tag{2.2}$$

where h is the Planck constant. The integration over the momenta can be performed analytically, which allows the partition function to be expressed as

$$Q_{NVT} = \frac{1}{N!}\frac{1}{\Lambda_t^{3N}\Lambda_r^N} Z_{NVT}\,, \tag{2.3}$$

where Λ_t and Λ_r are the translational and rotational de Broglie wavelengths, respectively

$$\Lambda_t = \left(\frac{\beta h^2}{2\pi m}\right)^{1/2}, \qquad \Lambda_r = \left(\frac{\beta h^2}{8\pi I}\right).$$

Here, m is the mass of a molecule and I is its moment of inertia.[2] In Eq. (2.3), we have defined the configurational (canonical) integral Z_{NVT} as

$$Z_{NVT} = \int d\Gamma^c \exp[-\beta\mathcal{U}(\Gamma^c)]\,, \tag{2.4}$$

with $d\Gamma^c = d\mathbf{r}^N d\boldsymbol{\Omega}^N$.

The connection with thermodynamics is established through the fundamental relation between the partition function and the Helmholtz free energy

$$F_{NVT} = -k_{\mathrm{B}}T \ln Q_{NVT}\,. \tag{2.5}$$

The canonical ensemble average of any property $\mathcal{A}(\Gamma)$ can be formally expressed as

$$\langle\mathcal{A}\rangle_{NVT} = \int d\Gamma \mathcal{A}(\Gamma)\rho_{NVT}(\Gamma) = \frac{\int d\Gamma \mathcal{A}(\Gamma)\exp[-\beta\mathcal{H}(\Gamma)]}{\int d\Gamma \exp[-\beta\mathcal{H}(\Gamma)]}\,.$$

In general, $\mathcal{A}(\Gamma)$ can be divided into two contributions: one that only depends on the momenta, and a second one that only depends on the translational and rotational coordinates of the particles. In this case, the integration over the momenta is straightforward and yields the ideal-gas contribution to the average. The actual difficulty lies in the integration over the set of coordinates Γ^c, which defines the configurational (or excess) contribution to the average. This can be written as

$$\langle\mathcal{A}\rangle^c_{NVT} = \int d\Gamma^c \mathcal{A}(\Gamma^c)\varrho_{NVT}(\Gamma^c) = \frac{\int d\Gamma^c \mathcal{A}(\Gamma^c)\exp[-\beta\mathcal{U}(\Gamma^c)]}{\int d\Gamma^c \exp[-\beta\mathcal{U}(\Gamma^c)]}\,, \tag{2.6}$$

where

$$\varrho_{NVT}(\Gamma^c) = \frac{1}{Z_{NVT}}\exp[-\beta\mathcal{U}(\Gamma^c)]\,. \tag{2.7}$$

[2] We are assuming rigid, linear molecules, for which there are two orientational degrees of freedom per molecule.

The final goal in a MC simulation is the evaluation of integrals of the type given in Eq. (2.6). Note that the integrations are not extended over the whole phase space, but over a restricted subspace, typically known as the configuration space of the system. Also note that no kinetic contribution appears now in the Boltzmann weight given in Eq. (2.6). To ease the notation, we will omit the superscript c and use Γ to denote a point in configuration space. One of such points are usually named as a configuration of the system. With this convention, $\varrho_{NVT}(\Gamma)$ in Eq. (2.7) represents the probability that the system is found in a particular configuration Γ with (configurational) energy $\mathcal{U}(\Gamma)$, irrespective of the translational and rotational momenta.

In principle, one could easily devise a computer code to evaluate the average defined in Eq. (2.6) according to the following "brute-force" MC algorithm:

1. Sample the configuration space by generating a random sequence of, say, M configurations Γ_n $(n = 1, \ldots, M)$ of the system.

2. Compute the interaction energy, $\mathcal{U}_n \equiv \mathcal{U}(\Gamma_n)$, the value of property $\mathcal{A}$, $\mathcal{A}_n \equiv \mathcal{A}(\Gamma_n)$, and the Boltzmann weight, $\exp[-\beta\mathcal{U}_n]$, in each configuration.

3. Estimate the expected ensemble average by the mean value $\langle\mathcal{A}\rangle_{\text{run}}$ over the sequence of configurations as

$$\langle\mathcal{A}\rangle_{NVT} \approx \langle\mathcal{A}\rangle_{\text{run}} = \frac{\sum_n \mathcal{A}_n \exp[-\beta\mathcal{U}_n]}{\sum_n \exp[-\beta\mathcal{U}_n]} \,. \tag{2.8}$$

This is essentially what lies behind the MC technique: an integral is approximated by a finite sum (two, in the case we are considering here), with evaluations of the integrand at randomly chosen values of the argument upon which the integrand depends. Anyone familiar with MC techniques as applied to condensed matter must recognize that the above scheme, as has been presented, is absolutely useless. The main reason is that under the typical thermodynamic conditions at which a simulation of a liquid state is performed, the overwhelming majority of configurations will be characterized by very large (positive) values of $\mathcal{U}$, with correspondingly low (actually, negligible) values of the Boltzmann weight. There is an extremely small fraction of configurations that makes a significant contribution to the integrals appearing in Eq. (2.6). Had this scheme worked, one could have directly determined the configuration integral (denominator), from wich we could have obtained the free energy, and hence the thermodynamics of the system.

The brute-force MC fails due to our choice of sampling strategy: the configurations have been randomly selected with equal probability, but the set contains no information. A much smarter sampling approach would involve selecting a set of configurations expected to make a significant contribution to the configurational integral. This strategy is known as importance sampling. This is best understood by considering the general approach to the evaluation of an integral by the MC technique (see, for instance, Ref. [19]). Assume we are interested in the computation of the following integral

$$I = \int_D dx\, f(x)\,,$$

defined over some domain D. Consider an arbitrary (distribution) function $g(x)$ such that $g(x) > 0$ and normalized to unity in the integration domain D. Define the function $F(x) = f(x)/g(x)$ and express I in the form

$$I = \int_D dx \left[\frac{f(x)}{g(x)}\right] g(x) = \int_D dx\, F(x) g(x)\,.$$

One now generates a set of M random variables ξ_n $(n = 1, \ldots, M)$ in the domain D distributed according to $g(x)$, and compute the arithmetic mean

$$\langle F \rangle_{\rm run} = \frac{1}{M} \sum_n F_n\,,$$

where $F_n \equiv F(\xi_n)$. The MC integration method amounts to consider the above average as an estimate of the integral I, i.e.,

$$I = \int_D dx\, F(x) g(x) \approx \langle F \rangle_{\rm run} = \frac{1}{M} \sum_n F_n\,. \tag{2.9}$$

Using the above considerations, one can recast the configurational average of property $\mathcal{A}$ [see Eq. (2.6)] as (recall that we are omitting the superscript c)

$$\langle \mathcal{A} \rangle_{NVT} = \int d\Gamma\, \mathcal{A}(\Gamma) \varrho_{NVT}(\Gamma) = \int d\Gamma \left[\frac{\mathcal{A}(\Gamma) \varrho_{NVT}(\Gamma)}{g(\Gamma)}\right] g(\Gamma)\,.$$

Following Metropolis *et al.* [2], the distribution g is chosen as $g(\Gamma) \equiv \varrho_{NVT}(\Gamma)$ (this choice fulfills the requirements demanded to the distribution function g), and $F(\Gamma)$ defined as the term in parenthesis appearing in the above integrand. Using Eq. (2.9), one arrives to

$$\langle \mathcal{A} \rangle_{NVT} \approx \langle \mathcal{A} \rangle_{\rm run} = \frac{1}{M} \sum_n \mathcal{A}_n\,. \tag{2.10}$$

This is the usual approach to compute ensemble averages in a MC simulation. It simply amounts to obtain the arithmetic mean of property $\mathcal{A}$ evaluated over a set of "important" configurations randomly drawn from the Boltzmann distribution. At variance with the expression emerging from the brute-force MC algorithm, Eq. (2.8), there is now no explicit computation of the partition function and, therefore, no possibility of computing the average of properties that depend directly on the partition function (or the configurational integral), the free energy being the most clear example. Averages in any ensemble other than the canonical are calculated exactly in the same manner; in this case, the chain of random configurations should be drawn from the appropriate probability density distribution that defines the ensemble.

There still remains the problem of generating a sequence (or chain) of configurations according to the desired probability distribution: this is essentially the heart of a MC program. In the next section, we briefly describe the solution given by Metropolis *et al.* [2].

2.2.2 Metropolis algorithm in the NVT ensemble

Consider that the system is in a given configuration Γ_m (for example, the initial configuration). A proper MC algorithm should answer the following two questions:

1. How to ensure that, in equilibrium, configurations in the chain appear with the appropriate Boltzmann weight.

2. How the next configuration Γ_n of the chain is generated (i.e., what are the rules for generating the full sequence of configurations).

In the following, $p_m \equiv \varrho_{\text{ens}}(\Gamma_m)$ denotes the probability that the system is in a particular configuration Γ_m (which is known to be proportional to the appropriate Boltzmann weight of the ensemble if the system is in equilibrium). The probability of generating the configuration Γ_n once the system is in Γ_m is denoted by $\pi_{m\to n}$. The product of these two probabilities gives the overall rate at which $\Gamma_m \to \Gamma_n$ transitions occur in the system. It can be shown [4] that the set of configurations will be distributed according to the distribution p_n if the transition probabilities are chosen such that

$$p_m \pi_{m\to n} = p_n \pi_{n\to m} \,.$$

This condition is called microscopic reversibility and simply states that the $\Gamma_m \to \Gamma_n$ transition should occur, on average, with the same frecuency as

the $\Gamma_n \to \Gamma_m$ transition. Therefore, the answer to question 1 posed earlier, is that the transition probabilites should be chosen so that their ratio satisfies

$$\frac{\pi_{m\to n}}{\pi_{n\to m}} = \frac{p_n}{p_m}\,. \tag{2.11}$$

There still remains the question of how the chain of configurations should be generated. We define $S_{m\to n}$ as the probability of selecting a configuration Γ_n when the system is in Γ_m; this is usually known as the underlying matrix of the Markov chain. We also define $\mathcal{P}_{m\to n}$ as the probability that the transition be accepted (acceptance probability). One has that $\pi_{m\to n} = S_{m\to n}\mathcal{P}_{m\to n}$. In the original Metropolis algorithm, the selection probability is chosen to be symmetric (i.e., $S_{n\to m} = S_{m\to n}$), which allows condition (2.11) to be expressed as

$$\frac{\mathcal{P}_{m\to n}}{\mathcal{P}_{n\to m}} = \frac{p_n}{p_m}\,.$$

One still has the freedom to choose the acceptance probabilites so as to fulfill the above condition. The Metropolis algorithm is based on the choice

$$\mathcal{P}_{m\to n} = \begin{cases} p_n/p_m & \text{if} \quad p_n < p_m, \\ 1 & \text{if} \quad p_n \geq p_m, \end{cases}$$

which can also be written as

$$\mathcal{P}_{m\to n} = \min\{1, p_n/p_m\}\,. \tag{2.12}$$

With all these considerations, the Metropolis solution for the probability that the system will move from configuration Γ_m to Γ_n (with $m \neq n$) is given by

$$\pi_{m\to n} = \begin{cases} S_{m\to n}(p_n/p_m) & \text{if} \quad p_n < p_m, \\ S_{m\to n} & \text{if} \quad p_n \geq p_m. \end{cases}$$

The system also has a non-vanishing probability of staying in the same state ($m = n$) given by

$$\pi_{m\to m} = 1 - \sum_{n\neq m} \pi_{m\to n}\,.$$

One still has the freedom to choose the selection probability. The proposal of Metropolis *et al.* goes as follows. A new trial configuration is generated by moving the center of mass of a molecule (translational displacement) to a neighbouring position $\mathbf{r}$ within a cube $\mathcal{C}$ centred at the old position. There is a large number (say, N_{trial}) of possible new positions, and all are given the same chance to be chosen. It then follows that

$$S_{m\to n} = \begin{cases} 1/N_{\text{trial}} & \text{if} \quad \mathbf{r} \in \mathcal{C}, \\ 0 & \text{otherwise.} \end{cases}$$

The trial move will be accepted according to the probability given in Eq. (2.12). In the canonical ensemble, where p_m is given by Eq. (2.7), the acceptance probability can be written as

$$\mathcal{P}_{m\to n} = \min\{1, \exp(-\beta\Delta\mathcal{U})\}\,, \tag{2.13}$$

where $\Delta\mathcal{U} = \mathcal{U}_n - \mathcal{U}_m$. If the move is rejected, the old configuration Γ_m is recounted as the new configuration in the sequence of configurations. The size of the cube $\mathcal{C}$ determines what fraction of the attempted moves will be accepted. We typically set this size so as to obtain 30–35% of accepted moves.

For molecular systems, the chain of configurations should also include configurations generated from a random reorientation of the molecules. This can be achieved in different ways [4]. Here, we follow the scheme considered by Frenkel and Smit [17] (appropriate for rigid, linear molecules) to carry out orientational moves. Let $\hat{\mathbf{u}}$ be a unit vector that specifies the orientation of a molecule. A unit vector $\hat{\mathbf{v}}$ is generated with random orientations (following algorithm 40 in Ref. [17]). This vector is multiplied by a scale factor γ (which will determine the magnitude of the trial rotation) and added to the original vector. The resulting vector $\hat{\mathbf{u}} + \gamma\hat{\mathbf{v}}$, once normalized to unity, is taken as the trial orientation. The new configuration is accepted according to the acceptance/rejection criterium given by Eq. (2.13).

For systems consisting of hard particles, where the energy of a given configuration is either zero or infinity, the acceptance criterium in the canonical ensemble simply amounts to checking whether overlaps are generated in a trial (translational or rotational) move. No overlaps will result in accepting the trial configuration, while the detection of a pair of overlaping molecules results in the rejection of the trial configuration.

2.2.3 Metropolis algorithms in the NPT ensemble

Most of the MC simulations performed in this work have been carried out in the isothermal-isobaric ensemble, where the total number of particles N, the pressure P, and the temperature T are constant (for the case of systems of hard particules, the temperature does not play any role). The partition function in the NPT ensemble can be written as

$$Q_{NPT} = \int dV \exp(-\beta PV) Q_{NVT}\,. \tag{2.14}$$

The appropriate configuration integral can be expressed as

$$Z_{NPT} = \int dV \exp(-\beta PV) Z_{NVT}\,. \tag{2.15}$$

The above expressions suggest that the volume of the system should also enter the specification of the different configurations of the system. Therefore, a point in this augmented phase space is defined by a particular realization of the translational and rotational coordinates, as well as by a particular value of V. One should note that there is an implicit dependence of the volume in the positional coordinates. This dependence is made explicit by considering a set of scaled coordinates. Assuming a rectangular box, with sides L_x, L_y, and L_z, the scaled coordinates are defined as $s_{i\alpha} = r_{i\alpha}/L_\alpha$, with $\alpha = x, y, z$, and $i = 1, \ldots, N$. Considering that $V = L_x L_y L_z$, the change to scaled variables involves $d\mathbf{r}^N = V^N d\mathbf{s}^N$. The corresponding probability density in the NPT ensemble now reads

$$\varrho_{NPT}(\Gamma; V) = \frac{1}{Z_{NPT}} V^N \exp\{-\beta[PV + \mathcal{U}(\Gamma)]\} \,. \tag{2.16}$$

A Metropolis algorithm can now be devised to sample configurations in the NPT ensemble in much the same way as it was done in the previous section for the canonical ensemble. Succesive configurations are generated according to Eq. (2.12), with $p_n \equiv \varrho_{NPT}(\Gamma_n; V_n)$ given by Eq. (2.16). Trial translational and rotational moves are performed so that the volume remains constant; therefore, the acceptance probability of such moves is simply the same as that considered in the canonical ensemble [cf. Eq. (2.13)]. The volume can be sampled in different ways, each giving rise to slightly different expressions for the acceptance probabilities. Throughout this work, we consider three different sampling algorithms:

(a) LVOL1 SCHEME, in which the volume is sampled isotropically. This will be used in this work when performing NPT simulations of phases with no translational order, namely, the isotropic and nematic phases. The box-side ratios, defined as $\xi_y = L_y/L$ and $\xi_z = L_z/L$, with $L \equiv L_x$, do not change along the simulation. It follows that $L_y = \xi_y L$, $L_z = \xi_z L$, $V = \xi_y \xi_z L^3$, and $dV = 3\xi_y \xi_z L^2 dL$. In terms of L, the configurational integral is written as

$$Z_{NPT} \propto \int dL\, L^{3N+2} \exp(-\beta PV) \int d\mathbf{s}^N d\Omega^N \exp(-\beta \mathcal{U}) \,,$$

from which we infer that the appropriate Boltzmann weight is

$$\begin{aligned} \varrho_{NPT}(\Gamma; L) &\propto L^{3N+2} \exp\{-\beta[PV + \mathcal{U}(\Gamma)]\} \\ &= \exp\{-\beta[PV + \mathcal{U}(\Gamma) - (3N+2) k_{\mathrm{B}} T \ln L]\} \,. \end{aligned}$$

The volume is then sampled by performing trial moves involving a random change in L. According to the Metropolis prescription, the

transition from configuration m to configuration n is accepted with probability given by Eq. (2.12); this is explicitly written as

$$\mathcal{P}_{m\to n} = \min\left(1, \exp\{-\beta[P\Delta V + \Delta\mathcal{U} - (3N+2)k_{\rm B}T\ln(L_n/L_m)]\}\right) , \tag{2.17}$$

where L_n (L_m) is the value of L in the new (old) configuration, $\Delta V = V_n - V_m$, and $\Delta\mathcal{U} = \mathcal{U}_n - \mathcal{U}_m$.

(b) LVOL2 SCHEME, appropriate for phases that exhibit translational order along one direction (say, the z direction), but no translational order in any transverse direction; this algorithm is typically used for the simulation of the smectic phase. Here, two decoupled trial volume changes are defined: one, in which the volume is sampled through changes in L_z at constant cross section, L_xL_y; and a second one, in which the cross section is changed isotropically at constant L_z. For the first case, it follows that $V = L_xL_yL_z$ with $dV = L_xL_ydL_z$; it can be easily shown that each configuration should appear with a Boltzmann weight given by

$$\varrho_{NPT}(\Gamma; L_z) \propto L_z^N \exp\{-\beta[PV + \mathcal{U}(\Gamma)]\} , \tag{2.18}$$

and the probability of accepting a move in which L_z changes is given, within the Metropolis scheme, by

$$\mathcal{P}_{m\to n} = \min\left(1, \exp\{-\beta[P\Delta V + \Delta\mathcal{U} - Nk_{\rm B}T\ln(V_n/V_m)]\}\right) . \tag{2.19}$$

For the second case, we change L (with $L_x = L$, and $L_y = \xi_y L$), at constant $\xi_y \equiv L_y/L_x$ and L_z. Now, $V = \xi_y L_z L^2$, with $dV = 2\xi_y L_z L dL$. It can be shown that each configuration should appear in the chain of configurations with a Boltzmann weight given by

$$\varrho_{NPT}(\Gamma; L) \propto L^{2N+1} \exp\{-\beta[PV + \mathcal{U}(\Gamma)]\} ,$$

and the probability of accepting a trial move in which L changes is given, within the Metropolis scheme, by

$$\mathcal{P}_{m\to n} = \min\left(1, \exp\{-\beta[P\Delta V + \Delta\mathcal{U} - (2N+1)k_{\rm B}T\ln(L_n/L_m)]\}\right) .$$

(c) LVOL3 SCHEME, in which the volume is sampled by performing independent trial changes of the box sides. This scheme is typically used for simulation of the solid phase in the NPT ensemble. Each time the volume is attempted to be changed, our algorithm considers a trial change in one of the box sides while keeping the other two constant. This is

performed three times, each time trying to vary (sequentally) L_x, L_y, or L_z. The corresponding Boltzmann weight of the configurations and acceptance probability of the trial move are the same as those given in Eq. (2.18) and (2.19), respectively.

In all cases, we set the maximum size of the sampling variable so that 20–25% of the attempted moves are accepted.

2.2.4 Estimation of statistical errors

As in a real experiment, the estimates of ensemble averages obtained in a simulation are subject to statistical uncertainties.[3] A quantification of these errors is of fundamental importance for obvious reasons. When dealing with the estimation of statistical errors in the computed averages in a simulation, one can find similarities, but also differences, with the procedure used for this purpose in real experiments.

Some comments regarding the notation will be useful for the present discussion. We organize our simulations in cycles (or sweeps), where one cycle consists on N trial molecular displacements, N trial molecular reorientations, and some trial volume changes (one when using the LVOL1 algorithm, two when using LVOL2, and three for the case of the LVOL3 algorithm). We recall that N is the number of molecules of the system. For comparison, one MC cycle corresponds approximately to one time step in molecular dynamics. After equilibration, the simulation is extendend over a total of $N_{\rm run}$ cycles. We recall that, when using a Metropolis-based algorithm, an estimate of the ensemble average of property $\mathcal{A}$ is given by the run average $\langle \mathcal{A} \rangle_{\rm run}$, defined as

$$\langle \mathcal{A} \rangle_{\rm run} = \frac{1}{N_{\rm run}} \sum_{i=1}^{N_{\rm run}} \mathcal{A}_i \,. \tag{2.20}$$

This is the value that we associate with the "measurement" of property $\mathcal{A}$; note that the experiment involves a simulation over a fixed number of cycles, $N_{\rm run}$, which can be chosen arbitrarily large. One should expect that the above value will be a closer realization of the (true) ensemble average if $N_{\rm run} \to \infty$. However, one is constraint to perform simulation experiments of finite length. In a real experiment, the error $\varepsilon(\mathcal{A})$ associated with the measurement of $\mathcal{A}$ is usually assessed by repeating the experiment M times. One then computes

[3] We are not dealing here with possible systematic errors, such as those due to system-size effects, periodic boundary conditions, etc.

the corresponding variance

$$\mathrm{var}(\mathcal{A}) \equiv \sigma^2(\mathcal{A}) = \frac{1}{M}\sum_{k=1}^{M}(\mathcal{A}_k - \langle\mathcal{A}\rangle)^2\,, \tag{2.21}$$

where $\mathcal{A}_k$ is the result after the k-th measurement, and $\langle\mathcal{A}\rangle$ is the mean value over the set of measurements. The error $\varepsilon(\mathcal{A})$ is usually reported as the standard deviation, $\sigma(\mathcal{A})$ (defined as the square root of the variance), with the usual meaning that there is a chance of 67% that a single measurement yields a value between $\langle\mathcal{A}\rangle$ and $\langle\mathcal{A}\rangle \pm \varepsilon(\mathcal{A})$, provided the individual measurements are independent and Gaussian distributed. This chance goes up to 97% when the error is reported as twice the standard deviation.

An straight application of this scheme to the estimation of errors in simulation is unpractical, as it would involve repeating the "experiment" (simulating the system over N_{run} cycles) M times. One should try instead to give an estimate of the error from the implementation of a *single* simulation experiment. A possible way to proceed is as follows. The full simulation is divided into n_b blocks, each comprising a total of $N_b = N_{\mathrm{run}}/n_b$ cycles. In the course of the simulation, the block (or coarse-grained) averages $\bar{\mathcal{A}}_n$ ($n = 1, \ldots, n_b$), as well as the variance of the block averages, are computed. The latter is given by

$$\sigma^2_{\mathrm{block}} = \frac{1}{n_b}\sum_{n=1}^{n_b}(\bar{\mathcal{A}}_n - \bar{\mathcal{A}})^2\,, \tag{2.22}$$

where $\bar{\mathcal{A}}$ is the mean value of the block averages

$$\bar{\mathcal{A}} = \frac{1}{n_b}\sum_{n=1}^{n_b}\bar{\mathcal{A}}_n\,. \tag{2.23}$$

$\bar{\mathcal{A}}$ does not depend on n_b [obviously, $\bar{\mathcal{A}}$ is exactly the same as $\langle\mathcal{A}\rangle_{\mathrm{run}}$ as given in Eq. (2.20)], but σ_{block} depends on the number of blocks n_b in which the simulation has been partitioned. It turns out that a good estimator of the variance in the run average can be computed from

$$\sigma^2(\bar{\mathcal{A}}) \approx \frac{1}{n_b - 1}\sigma^2_{\mathrm{block}}\,, \tag{2.24}$$

provided the block averages are uncorrelated (i.e., statistically independent). One should anticipate that this condition will hold if N_b (number of cycles per block) is chosen sufficiently large.

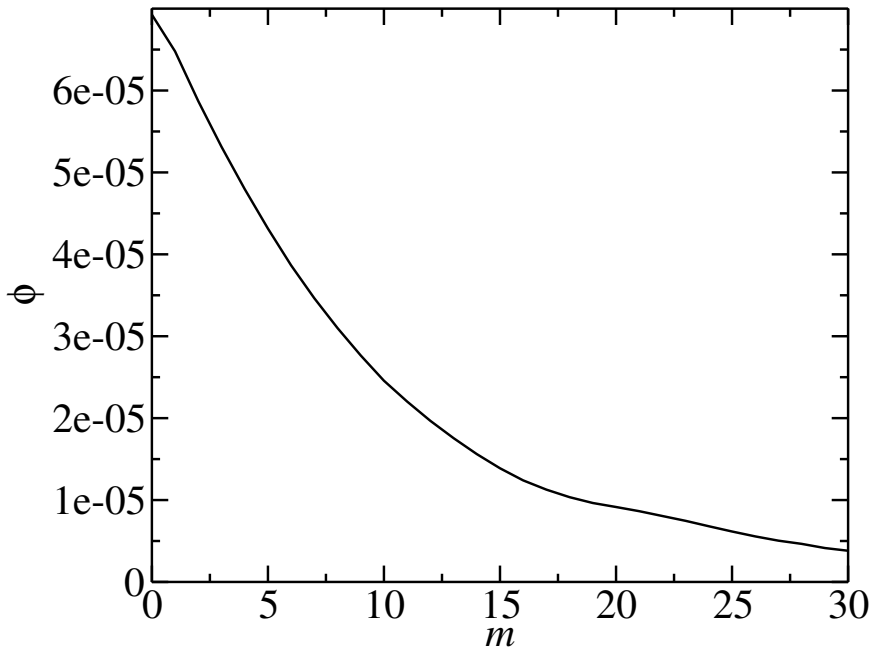

Figure 2.1: Density autocorrelation function as a function of the distance m between consecutive blocks (100 MC cycles per block) as obtained from a constant-pressure MC simulation of a system of 500 hard spheres at a reduced pressure of $\beta P D^3 = 1$. Details on the simulation are given in the main text.

One possible way to check whether the block averages are uncorrelated (or whether the choice of N_b is good enough) is through the computation of the autocorrelation function $\phi(m)$ of the block averages of property $\mathcal{A}$. This is defined as [18, 20, 21]

$$\phi(m) = \langle (\bar{\mathcal{A}}_k - \bar{\mathcal{A}})(\bar{\mathcal{A}}_{k+m} - \bar{\mathcal{A}}) \rangle_k = \frac{1}{n_b - m} \sum_{k=1}^{n_b - m} (\bar{\mathcal{A}}_k - \bar{\mathcal{A}})(\bar{\mathcal{A}}_{k+m} - \bar{\mathcal{A}}) \,. \quad (2.25)$$

$\phi(m)$ gives an indication of the correlation between block averages computed m blocks appart. Note that for $m = 0$, $\phi(0)$ is just the variance of the block averages defined in Eq. (2.22). As m increases, $\phi(m)$ will decrease, indicating that block averages become increasingly uncorrelated. This function is expected to have an exponential decay at short times[4], i.e.,

$$\phi(m) = \phi(0) \exp(-m/\tau) \,, \quad (2.26)$$

where τ is a characteristic decay time. The correlation time τ_c is defined as $\tau_c = 2\tau$. We use the value of τ_c as a measure of the number of blocks

[4]We are using here the word time in a Monte Carlo sense, with m labelling the time, and with N_b being the unit of time.

beyond which the block averages become uncorrelated. It then follows that $\tau_c N_b$ is the minimum number of cycles that a block should have in order to ensure that succesive block averages become statistically independent. The total number of uncorrelated blocks in the run (of length $N_{\rm run}$) is then $N_{\rm run}/(\tau_c N_b)$. Plugging this number for n_b in the right-hand side of Eq. (2.24), will give us a fair estimate of the variance in the run average.

A practical example will help to clarify the above discussion. We consider the estimate of the error associated with the average number density $\rho = N/V$ obtained from a constant-pressure MC simulation of a system of $N = 500$ hard spheres of diameter D.[5] We set the input pressure to $\beta P D^3 = 1$. Under this pressure, the system is fluid-like. After the equilibration stage, the system is run for a total of $N_{\rm run} = 4 \times 10^5$ cycles. Block averages are calculated over blocks of relatively small size ($N_b = 100$ cycles per block). The simulation comprises a total of $n_b = N_{\rm run}/N_b = 4 \times 10^3$ blocks. We find a value of $\bar{\rho} \equiv \langle \rho \rangle_{\rm run} = 0.39856$ for the run average of the number density, and a value of $\sigma_{\rm block} = 0.00832$ for the standard deviation of the block averages calculated according to Eq. (2.22). We plot in Fig. 2.1 the autocorrelation function of the block averages of the density, $\phi_\rho(m)$. From the short-time (exponential) behaviour of $\phi_\rho(m)$, we find $\tau \approx 10$ and, therefore, a correlation time $\tau_c = 2\tau = 20$. From this, we estimate that blocks should contain a minimum of $\tau_c N_b = 2000$ cycles. The data from the run can be blocked so as to obtain a total of $N_{\rm run}/(\tau_c N_b) = 200$ independent block averages. Inserting this value in Eq. (2.24) yields $\sigma = 0.0006$. The simulation result should then be reported as $\bar{\rho} = 0.3986(6)$ (error $\varepsilon = \sigma$). In most instances, the errors in this work will be reported as $\varepsilon = 2\sigma$, i.e., $\bar{\rho} = 0.3986(12)$ for the present example.

We show in Fig. 2.2 $\sigma(\bar{\mathcal{A}})$ [cf. Eq. (2.24)] for different choices of the block size for the run considered here. According to the plot, the estimate of the error becomes insensitive to the choice of the block size provided the latter is chosen sufficiently large.

Estimates of the error according to the previous procedure should in principle be performed for each magnitude computed in a simulation (note that each property would have a different correlation time). This can be very tedious. A much practical approach would be to consider a value of the block size, N_b, sufficiently large and avoid having to perform the full autocorrelation analysis in every simulation. We normally use a value of $N_b = 5000$ cycles, which, according to our example, is safe enough.

[5] We use D to set the unit of length and define dimensionless reduced units in this section.

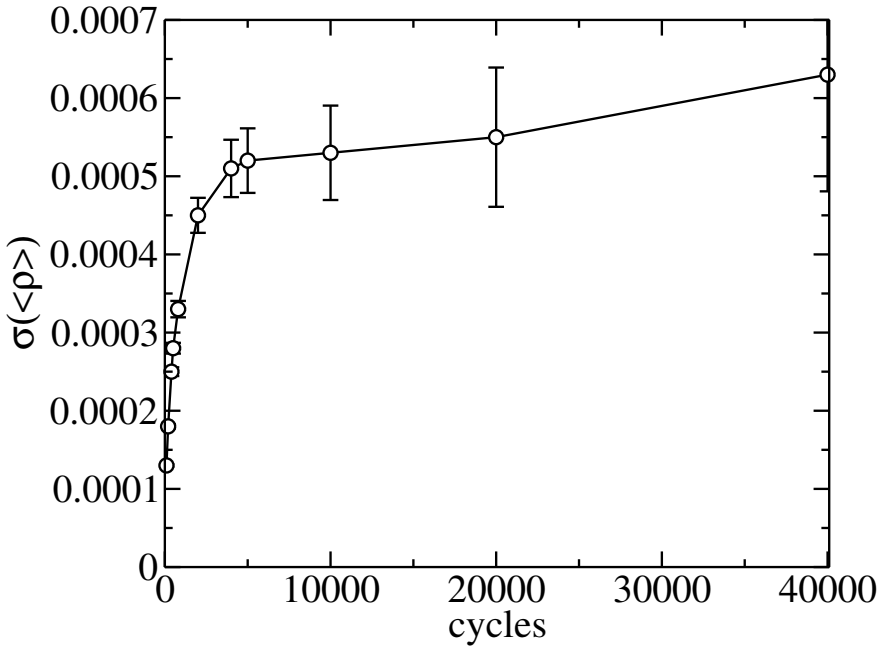

Figure 2.2: Standard deviation associated with the run average of the number density obtained in a constant-pressure simulation of a system of 500 hard spheres at a pressure of $\beta P D^3 = 1$ for different choices of the block size.

We end this section by recalling that the analysis described here is limited to the estimation of errors of properties that can be computed as run averages. Errors on other properties should be estimated in a different way. Of particular importance in this thesis is the free energy: this property cannot be computed as an ensemble average. The method that we consider for estimating the errors in free energies will be explained in subsequent chapters.

2.3 Free energy calculation: generalities

As already mentioned, the main goal of this work is to determine the phase diagram of different model potentials, and this requires the calculation of the free energy of all of the phases. However, this quantity can not be calculated directly in a computer simulation since it is not an average of functions of the phase space coordinates of the system. One has to use instead indirect methods [17]. This is as in experiments, where the free energy is not directly accesible. One should note that first-order derivatives of the free energy can be easily calculated in a computer experiment (the pressure being an example). We review in this section a number of methods for the indirect

calculation of the free energy from computer simulation.

One way to compute the free enery of a system is to connect the state under consideration with another state of known free energy through a reversible path. This involves a calculation of the change in free energy along the path by integration of appropiate thermodynamic functions (typically, first-order derivatives of the free energy) which we will describe in the next section. There are only few systems for which the free energy is known, as for example the ideal gas or the Einstein crystal. The relevant expression can be written as

$$F(Y_1) = F(Y_0) + \int_{Y_0}^{Y_1} dY \left(\frac{\partial F}{\partial Y}\right) ,$$

where Y is some thermodynamic property and $F(Y_0)$ is the free energy of the reference state.

There are other methods for the computation of the free energy difference between two states from simulation. One of these methods, the so-called simulation method in the expanded ensemble proposed by Lyuvartsev *et al.* [22], has been ocassionally used in this work, and will be discussed below. Though most of the methods for the calculation of the free energy actually compute free-energy differences, we should recall that there is a particular simulation method that provides the absolute free energy. This is the case of the particle-insertion method, due to Widom [23]. This method, as well as an extension used in the present work, is also discussed below.

2.3.1 Parametric integration

In this method the Hamiltonian $H = H(\lambda)$ of the system is considered as a function of a generic parameter λ which varies along the integration path [17]. In the following, we describe the parametric integration method in the NVT ensemble. The Helmholtz free energy $F(\lambda)$ in this ensemble is related to the canonical partition function through the relation

$$F(\lambda) = -k_{\mathrm{B}}T \ln Q(\lambda) , \tag{2.27}$$

where the partition function depends on the parameter λ and is given by

$$Q(\lambda) = \frac{1}{N!}\frac{1}{\Lambda_t^{3N}\Lambda_r^N}\int d\Gamma \exp\left[-\beta\mathcal{U}(\lambda)\right] . \tag{2.28}$$

Differentiating in both terms of Eq. (2.27) with respect to the parameter λ we obtain

$$\frac{\partial F(\lambda)}{\partial \lambda} = -k_{\mathrm{B}}T\frac{1}{Q(\lambda)}\frac{\partial Q(\lambda)}{\partial \lambda} = \frac{\int d\Gamma \left[\partial\mathcal{U}(\lambda)/\partial\lambda\right]\exp[-\beta\mathcal{U}\left(\lambda\right)]}{\int d\Gamma \exp[-\beta\mathcal{U}\left(\lambda\right)]} .$$

Recalling the definition of ensemble average in the canonical ensemble, one can recast the above expression as:

$$\frac{\partial F\left(\lambda\right)}{\partial \lambda} = \left\langle \frac{\partial \mathcal{U}(\lambda)}{\partial \lambda} \right\rangle_{\lambda} . \tag{2.29}$$

Upon integration of Eq. (2.29) between two states characterized by parameters λ_0 and λ_1, one obtains

$$F(\lambda_1) - F(\lambda_0) = \int_{\lambda_0}^{\lambda_1} d\lambda \left\langle \frac{\partial \mathcal{U}(\lambda)}{\partial \lambda} \right\rangle_{\lambda} . \tag{2.30}$$

If the free energy of the initial state is known, we can obtain the free energy of the final state by numerical quadrature. In practice, the integral is numerically calculated using Gaussian quadrature [24]. This requires performing a number of NVT simulations at intermediate values of λ between λ_0 and λ_1.

A similar relation follows in the NPT ensemble,

$$G(\lambda_1) - G(\lambda_0) = \int_{\lambda_0}^{\lambda_1} d\lambda \left\langle \frac{\partial \mathcal{U}(\lambda)}{\partial \lambda} \right\rangle_{\lambda} ,$$

where G is the Gibbs free energy. In common with other methods, one must ensure that the system does not cross a first-order phase transition along the integration path.

2.3.2 Thermodynamic integration

The thermodynamic integration technique is used in this work to calculate the free energy of different phases, such as isotropic, nematic, and solid. This method requires that the free energy of a reference state and the equation of state of the system under study be known. In order to derive the working expression of the method, we start from the thermodynamic relation

$$\left(\frac{\partial F}{\partial V}\right)_{NVT} = -P\,, \tag{2.31}$$

that links the pressure with the Helmholtz free energy. For convenience, we express the above derivative in terms of the number density $\rho = N/V$,

$$\left(\frac{\partial F}{\partial \rho}\right)_{NVT} = \frac{N}{\rho^2}\,P\,.$$

Integrating the above equation along an isotherm, we obtain the key expression of the thermodynamic integration method,

$$f(\rho) = f_{\rm ref} + \int_{\rho_{\rm ref}}^{\rho} Z(\rho') \frac{d\rho'}{\rho'} , \tag{2.32}$$

where $f(\rho)$ is the free energy at an arbitrary density, $f_{\rm ref} = f(\rho_{\rm ref})$ is the free energy at the reference density $\rho_{\rm ref}$, and $Z = P/(\rho k_{\rm B} T)$ is the compressibility factor. In the above equation, we have defined $f = F/(N k_{\rm B} T)$. According to Eq. (2.32), the calculation of the free energy at a density ρ requires the equation of state along an isotherm to be known.

If the pressure is chosen as the integration variable along the isotherm, one arrives at a similar expression,

$$g(P) = g_{\rm ref} + \int_{P_{\rm ref}}^{P} Z(P') \frac{dP'}{P'} , \tag{2.33}$$

but now involving the difference in Gibbs free energy. In the above equation, we have defined $g = G/(N k_{\rm B} T)$.

2.3.3 The expanded ensemble

As mentioned above, the free energy can not be directly measured from a simulation since it can not be expressed as an average over phase space; one therefore has to make use of indirect methods to compute free energy differences. One of these methods is the expanded ensemble proposed by Lyuvartsev *et al.* [22].

The general idea of the method is as follows.[6] One samples the configuration space of a set of M subensembles, each of them representative of a system characterized by an interaction energy $\mathcal{U}_m = \mathcal{U}(\Gamma_m; \epsilon_m)$ with $m = 1, \ldots, M$, and ϵ_m being an arbitrary set of parameters. We can write the corresponding configurational integral for each subensemble as

$$Z_m = \int d\Gamma_m \exp\left(-\beta \mathcal{U}_m\right) .$$

For each subensemble m we define the configuration space Γ_m so that

$$\Gamma = \Gamma_0 \cup \Gamma_1 \cup \ldots \Gamma_M .$$

[6] The method is presented here in the canonical ensemble; it is straightforward to generalize the method to any other ensemble.

A global configurational integral for the expanded ensemble is defined as

$$Z = \sum_{m=0}^{M} Z_m \exp\left(\beta W_m\right) ,$$

where W_m is a weight factor for the potential $\mathcal{U}_m$. The probability of finding the system in a configuration of the subensemble Γ_m when sampling the whole configuration space Γ can be written as

$$p_m = \frac{Z_m \exp \beta W_m}{Z} \propto \exp\left[-\beta\left(\mathcal{U}_m - W_m\right)\right] . \tag{2.34}$$

According to Eq. (2.34) it follows that

$$\ln\left(\frac{p_n}{p_m}\right) = \ln\left(\frac{Z_n}{Z_m}\right) + \beta\left(W_n - W_m\right) . \tag{2.35}$$

From the relation between the free energy and the partition function one can write

$$\ln\left(\frac{Z_n}{Z_m}\right) = -\beta(F_n - F_m) .$$

After substitution into Eq. (2.35), one gets

$$\beta(F_n - F_m) = -\ln\left(\frac{p_n}{p_m}\right) + \beta\left(W_n - W_m\right) , \tag{2.36}$$

which can be rewritten as

$$f_n - f_m = -\frac{1}{N}\ln\left(\frac{p_n}{p_m}\right) + \left(w_n - w_m\right) , \tag{2.37}$$

where $w = \beta W/N$ and $f = F/(N\mathrm{k_B}T)$. Eq. (2.37) is the key relation of the expanded-ensemble method.

One can devise a Metropolis algorithm to sample the expanded ensemble. In addition to the standard (translational and rotational) MC moves, one performs trial moves to drive the system from one subensemble to another. The acceptance probability of such a move in the canonical ensemble is given by

$$\mathcal{P}_{m\to n} = \min\left\{1, \exp\left[\beta\left(\Delta W_{mn} - \Delta\mathcal{U}_{mn}\right)\right]\right\} , \tag{2.38}$$

where $\Delta W_{mn} = W_n - W_m$ and $\Delta\mathcal{U}_{mn} = \mathcal{U}_n - \mathcal{U}_m$. The probabilities appearing in Eq. (2.37) are determined from the frecuency of visits to each subensemble in the course of the simulation. In general, consecutive subensembles in the Markov chain will be separated by a large free energy barrier, which may

give rise to a poor sampling of subsystems with high free energy. As a result, the corresponding probabilities may differ in several orders of magnitude and the scheme turns inefficient. This can be alleviated by a suitable choice of weighting coefficients. Though the difference in free energy $\Delta F_{mn} = F_n - F_m$ should not depend on ΔW_{mn}, the probability ratio p_n/p_m is strongly dependent on the weight factors, as can be seen after manipulating Eq. (2.36)

$$\frac{p_n}{p_m} = \exp[\beta(\Delta W_{mn} - \Delta F_{mn})] \,.$$

According to this expression, the choice $\Delta W_{mn} \approx \Delta F_{mn}$ will ensure a nearly uniform sampling with $p_n \approx p_m$. This choice, however, would require prior knowledge of the quantities we want to compute. It is straightforward to devise a simple scheme that systematically corrects the set of weight functions [25, 26]: starting from a suitable initial guess, and making use of expression (2.36), the weight factors are succesively refined according to

$$\beta(\Delta W_{mn})_{\text{new}} = \beta(\Delta W_{mn})_{\text{old}} - \ln \frac{p_n}{p_m} \,, \tag{2.39}$$

during the course of a preliminary run.

The expanded ensemble simulation technique has proved quite efficient in a variety of problems involving the computation of free energy differences; examples include the calculation of the free energy [22, 27] or the chemical potential [28] of dense model fluids [29–31] and crystalline solids [25, 26]; the free energies of solute molecules into different solvents [32]; or the surface tension of the vapour-liquid interface [33]. In the present work, this technique has been used to compute the free energy of hard sphere solids, and the difference in free energy between an interacting and non-interacting Einstein crystal.

2.3.4 Test-particle insertion method

The test-particle insertion technique (usually referred to as the Widom method) allows one to compute the chemical potential in a system characterized by an arbitrary interaction potential $\mathcal{U}$. Though originally devised for simulations in the NVT ensemble [23], the method can be easily extended to the computation of the chemical potential in any ensemble. The working expression in the NPT ensemble reads as follows (see, for example Frenkel and Smit [17])

$$g(P) = g_{\text{id}}(P) + g_{\text{ex}}(P) = \ln(\beta P D^3) - \ln \left\langle \frac{\beta P V}{(N+1)} \exp(-\beta \Delta \mathcal{U}) \right\rangle \,, \tag{2.40}$$

where $\Delta\mathcal{U}$ is the interaction potential of a ghost particle with the rest of particles of the system. The angular brackets denote an average over the appropriate ensemble characterized by constant number of particles N, pressure P, and temperature T. In expresion (2.40), we have chosen the de Broglie wave length equal to D, where D is some arbitrary length scale in the interaction model.

Before going any further, some comments are in order:

- g in Eq. (2.40) represents the chemical potential in units of $k_{\mathrm{B}}T$. We use this notation, rather than the more standard notation $\beta\mu$, in order to be consistent with our choice of f and g to denote the Helmholtz and Gibbs free energy per particle, respectively, in units of $k_{\mathrm{B}}T$. For one-component systems, it follows that $g = \beta\mu$.

- Expression (2.40) defines the chemical potential up to an (arbitrary) additive constant. When locating phase transitions, this constant will cancel out when equating the chemical potentials of the coexisting phases *provided the same choice of constants is made in both phases*.

- The ideal-gas contribution *does* depend on the choice of length unit. Different choices will yield different values of the chemical potential of the ideal gas: they will simply differ by an additive constant (see our previous comment). The excess contribution, however, *does not* depend on the particular choice of length unit.

- As most of the simulations performed in this work are carried out in the NPT ensemble, we have defined the ideal-gas contribution in terms of the pressure and not in terms of the number density, as is usually done when working in the canonical ensemble.

For the particular case of systems characterized by hard interactions, g_{ex} is related to the probability that no overlaps take place in the system when a trial particle insertion is attempted. This restricts the applicability of the above (unweighted) scheme to situations where the density is not too high. A number of alternative strategies have been devised in order to push the applicability of this method to relatively dense systems (see Ref. [17]). The practical implementation of the method for molecular systems involves the following steps:

1. Generate a trial position for the centre of mass of the ghost particle within the limits of the simulation box.

2. Generate a random orientation for the ghost particle.

3. Loop over the N particles of the system and calculate the energy $\Delta\mathcal{U}$ appearing in Eq. (2.40). For hard-particle systems, the corresponding Boltzmann factor will be either zero or one, depending on whether or not overlaps between the ghost particle and the particles of the system are found.

The standard implementation of the above scheme considers an unweighted sampling of the trial positions and orientations from a uniform distribution (i.e., all posible positions and orientations of the ghost particle are generated with the same likehood). We have considered a variant of the method which is expected to be appropriate for the computation of the chemical potential of fluid systems with orientational order. This (weighted) scheme is described next.

Let us consider an orientationally ordered (nematic) fluid consisting of N axially symmetric particles. The long axis of the molecules define an average (macroscopic) direction of alignment (the so-called *director* of the phase). The degree of orientational order can be characterized by the orientational distribution function, $h(\Omega)$, defined as the probability of finding a particle with orientations within the solid angle Ω. This distribution is normalized to one, so that for the isotropic phase, $h = 1/(4\pi)$. Uniaxial nematic phases exhibit cylindrical symmetry around the director, and $h(\Omega)$ just depends on a single angle, θ, where θ is the angle between the main molecular axis and the director. In this case, it turns out more convenient to choose the normalization of $h(\cos\theta)$ as 4π. With this choice, it follows that

$$\int_0^1 dx\, h(x) = 1 \tag{2.41}$$

where $x = \cos\theta$. According to this choice, the isotropic phase will be characterized by $h = 1$, and the nematic phase by a function $h(x)$ peaked around the value $x = 1$.

The weighted implementation of the Widom method involves the following steps. The polar angle ϕ that defines the molecular axial vector is randomly (and uniformly) generated in the range $[0, 2\pi]$. The azimuthal angle $x = \cos\theta$, however, is generated from a suitable non-uniform distribution function. The best choice would correspond to the expected orientational distribution function $h(x)$ of the nematic phase. This is unkown beforehand, but a simple alternative is to make use of the Onsager distribution, which

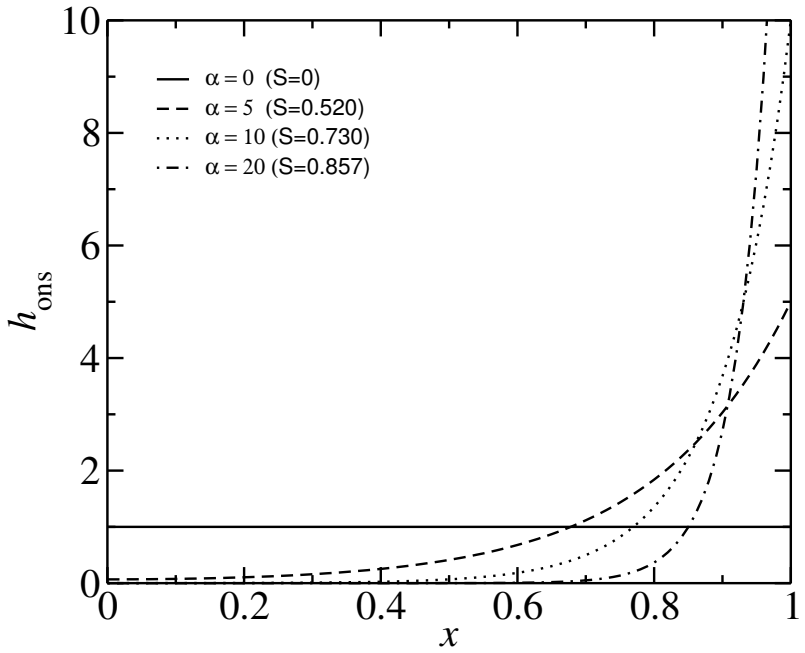

Figure 2.3: Onsager distribution function $h_{\rm ons}$ Eq. (2.42) in terms of $x = \cos\theta$ for different values of the parameter α shown in the plot. The accompanying values of S are the corresponding values of the orientational order parameter $S_{\rm ons}$.

has the following form

$$h_{\rm ons}(x) = \frac{\alpha \cosh(\alpha x)}{\sinh \alpha}\,, \tag{2.42}$$

where α is a (positive) parameter. Orientational disorder (isotropic phase) is characterized by $\alpha = 0$, while orientational order (nematic phase) is characterized by $\alpha > 0$: the larger the parameter α is, the stronger the degree of orientational order will be. Fig. 2.3 depicts the Onsager distribution function for different choices of the parameter α. The orientational order parameter $S_{\rm ons}$ resulting from the Onsager distribution depends on α, where $S_{\rm ons}$ is defined as

$$S_{\rm ons} = \int_0^1 dx\, \frac{(3x^2-1)}{2}\, h_{\rm ons}(x)\,. \tag{2.43}$$

Here, we use a rejection algorithm due to von Neumann (see appendix G.6 in Allen and Tildesley [4]) to generate the random variable x distributed according to the Onsager distribution for a given value of α. The method runs as follows. Let x be a random variable distributed according to an arbitrary distribution $f(x)$. Assume that $f(x)$ is bounded and of finite range,

$x_1 \leq x \leq x_2$. Define $g(x) = f(x)/A$, where $A \geq 1$ is an arbitrary constant defined so as to insure $0 \leq g(x) \leq 1$ in the range $x_1 \leq x \leq x_2$. According to von Neumann's algorithm, one has to proceed as follows to generate x randomly on the distribution of interest:

(a) Generate two random variables ξ_1, ξ_2 uniformly distributed in [0,1].

(b) Generate x randomly in the range $[x_1, x_2]$ as $x = x_1 + (x_2 - x_1)\xi_2$, and evaluate $g(x)$.

(c) If $\xi_1 \leq g(x)$, then x is a random number distributed according to $f(x)$; otherwise, go to (a).

In practice, our implementation of von Neumann's algorithm involves the following steps:

1. The distribution $f(x)$ is taken to be the Onsager distribution defined in Eq. (2.42), $f(x) = h_{\rm ons}(x)$. The value of α is chosen so that $S_{\rm ons}$ as given from Eq. (2.43) approximately matches the expected value of the order parameter of the nematic phase under investigation. Typical values of α are taken in the range $5 < \alpha < 20$ (see Fig. 2.3).

2. Choose $A = \alpha$. With this choice, $g(x) = \cosh(\alpha x)/\sinh(\alpha)$, and therefore, $g(x) \leq 1$ as required in von Neumann's algorithm.

3. Follow steps (a) through (c) in von Neumann's scheme, considering $x_1 = 0$, and $x_2 = 1$. The generated value, x, will obey the Onsager distribution.

Finally, a value ϕ for the polar angle of the ghost particle is uniformly generated in the range $[0, 2\pi]$. Recall that x is the angle with respect to the director; therefore, x and ϕ define the orientation of the axial vector of the ghost particle in the director frame, $\hat{\mathbf{u}}_{\rm dir}$.[7] Before calculating the interaction between the ghost particle and the rest of particles of the system, one has to express the components of the axial vector of the ghost particle in the simulation-box frame, $\hat{\mathbf{u}}_{\rm box}$, using

$$\hat{\mathbf{u}}_{\rm box} = \mathbf{R}\ \hat{\mathbf{u}}_{\rm dir}\ ,$$

where $\mathbf{R}$ is the corresponding rotation matrix. The columns of the rotation matrix are simply the components of the eigenvectors of the orientational matrix $\mathbf{Q}$.

[7] The unit vectors of this frame, defined as the eigenvectors of the orientational matrix $\mathbf{Q}$, defined later in Eq. (4.4), are routinely calculated in our codes.

The chemical potential within the weigthed scheme reads

$$g(P) = \ln(\beta P D^3) - \ln \left\langle \frac{\beta P V}{h_{\rm ons}(x)(N+1)} \exp(-\beta \Delta \mathcal{U}) \right\rangle . \tag{2.44}$$

2.4 Free energy calculation of fluid phases

2.4.1 The isotropic phase

We consider the ideal gas as the reference state for the calculation of the free energy of the isotropic phase. Applying Eq. (2.32) to the ideal gas (id) and to the isotropic (I) phase at a density ρ, we obtain

$$f^{\rm id}(\rho) = f^{\rm id}(\rho_0) + \int_{\rho_0}^{\rho} Z^{\rm id}(\rho') \frac{d\rho'}{\rho'} , \tag{2.45}$$

$$f(\rho) = f(\rho_0) + \int_{\rho_0}^{\rho} Z(\rho') \frac{d\rho'}{\rho'} , \tag{2.46}$$

where ρ_0 is some arbitrary density. Substracting Eq. (2.45) from Eq. (2.46), and taking the limit $\rho_0 \to 0$ (which leads to $f(0) = f^{\rm id}(0)$) yields the relation which allows us to calculate the free energy of the isotropic fluid phase once the equation of state along an isotherm is known,

$$f(\rho) = f^{\rm id}(\rho) + \int_0^{\rho} [Z(\rho') - 1] \frac{d\rho'}{\rho'} . \tag{2.47}$$

The integration in the above equation is performed by fitting the simulation data for the compressibility factor. In principle, one is free to choose the functional form of the fit, and a polynomial function will be always used throughout this work. In particular, the simulation results will be fitted to an expression of the form

$$Z(\rho) = \sum_{i=1}^{m} a_i \, \rho^{i-1} , \tag{2.48}$$

where a_i are the fitting coefficients. The first coefficient is fixed to $a_1 = 1$ in order to reproduce the low-density limit of Z, while the rest of the coefficients are fitted using a linear least-square method [24]. Finally, inserting the expression of the compressibility factor in Eq. (2.47) one obtains the free energy at any density along the isotropic branch

$$f(\rho) = f^{\rm id}(\rho) + \sum_{i=2}^{m} \frac{a_i}{i-1} \rho^{i-1} ,$$

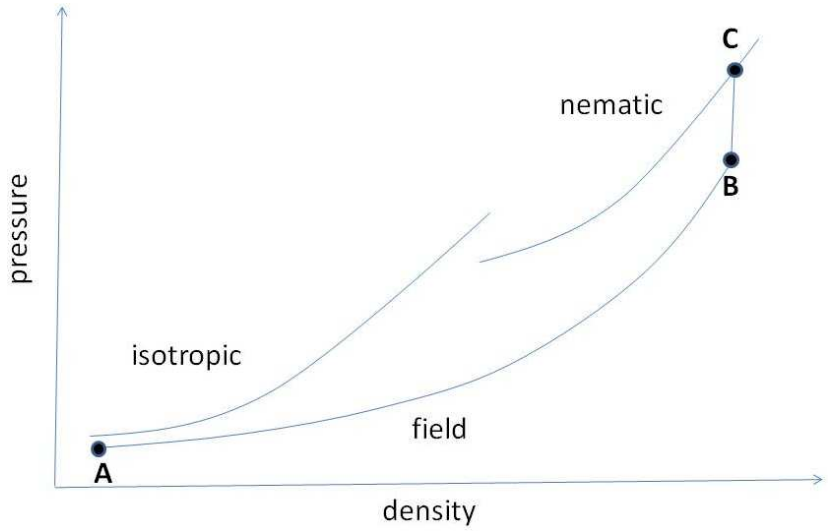

Figure 2.4: Schematic representation of the thermodynamic path used to compute the free energy of a reference nematic state.

where $f^{\mathrm{id}}(\rho) = \ln(\Lambda_t^3 \Lambda_r \rho) - 1$. The Gibbs free energy at density ρ follows from the thermodynamic relation $G = F + PV$, which can be written as

$$g(\rho) = f(\rho) + Z(\rho)\,. \tag{2.49}$$

Alternatively, one can compute the Gibbs free energy at any pressure by fitting Z to a polynomial in P of the form

$$Z(P) = \sum_{i=1}^{m} c_i P^{i-1}\,.$$

In this case, it is straightforward to show that

$$g(P) = g^{\mathrm{id}}(P) + \sum_{i=2}^{m} \frac{c_i}{i-1} P^{i-1}\,. \tag{2.50}$$

Here, $g^{\mathrm{id}}(P) = \ln(\beta P \Lambda_t^3 \Lambda_r)$ is the Gibbs free energy of the ideal gas at pressure P.

2.4.2 The nematic phase

According to the key expression of thermodynamic integration along an isotherm [c.f. Eq. (2.32)], the free energy of the nematic fluid at density ρ is given by

$$f(\rho) = f_{\mathrm{ref}} + \int_{\rho_{\mathrm{ref}}}^{\rho} Z(\rho') \frac{d\rho'}{\rho'}\,, \tag{2.51}$$

where $Z(\rho)$ is the compressibility factor of the nematic phase. At variance with the isotropic phase, the ideal gas can not be used as the reference state. As the nematic liquid is expanded to the low-density region, the system crosses a first-order (order-disorder) transition. A reversible path can, however, be devised if the order-disorder transition is artificially supressed. This idea is behind the method proposed by Frenkel and Mulder [11]: an external field, H_{ext}, is applied to the system so that the orientational order persists even at low densities. This Hamiltonian reads

$$H_{\text{ext}} = \lambda \sum_{i=1}^{N} \sin^2 \theta_i \,, \tag{2.52}$$

where θ_i is the angle between the long axes of molecule i and the direction of the external field, and λ is the strength of the external field. The value of λ is chosen such that the isotropic-nematic transition is suppressed.

A reversible path is now devised from the nematic reference state (defined by a density ρ_{ref}) to a low-density ideal-gas state. A schematic representation of this path is shown in Fig. 2.4. The ideal gas plus external field (point A in Fig. 2.4) is compressed at constant temperature up to ρ_{ref} (point B). The external field is then switched off at constant density ρ_{ref}. The free energy of the nematic reference state (point C) is thus given by

$$f_{\text{ref}} \equiv f_{\text{C}} = f_{\text{A}} + \Delta f_{\text{AB}} + \Delta f_{\text{BC}} \,. \tag{2.53}$$

f_{A} represents the free energy of the ideal gas at density ρ_{ref} in the presence of the external field, which can be written as

$$f_{\text{A}} = \ln(\Lambda_t^3 \Lambda_r \rho_{\text{ref}}) - 1 + f_\lambda \,,$$

where f_λ stands for the contribution of the external field, which is given by

$$f_\lambda = -\ln q_\lambda \,, \tag{2.54}$$

with

$$q_\lambda = \int_0^1 dx \exp\left[-\beta\lambda\left(1 - x^2\right)\right] \,. \tag{2.55}$$

The integration is performed by expanding the integrand, which gives

$$q_\lambda = \exp(-\beta\lambda) \sum_{n=0}^{\infty} \frac{1}{2n+1} \frac{(\beta\lambda)^n}{n!} \,. \tag{2.56}$$

The computation of Δf_{AB} in Eq. (2.53) is analogous to that of the isotropic phase. According to Eq. (2.47), one now has

$$\Delta f_{\mathrm{AB}} = \int_0^{\rho_{\mathrm{ref}}} [Z_\lambda(\rho) - 1] \frac{d\rho}{\rho} ,$$

where Z_λ is the compressibility factor of the system in the presence of the external field.

Finally, parametric integration is used to compute the free energy change of the process of switching off the external field. According to Eq. (2.30)

$$\Delta f_{\mathrm{BC}} = -\frac{1}{N k_{\mathrm{B}} T} \int_0^\lambda d\lambda \left\langle \sum_{i=1}^{N} \sin^2 \theta_i \right\rangle_\lambda .$$

A 10-point Gaussian quadrature is used to calculate the above integral.

Once the free energy of the reference nematic state f_{ref} has been computed, the free energy of a nematic state at any density ρ follows from Eq. (2.51). As we did for the isotropic phase, the equation of state obtained from simulation is fitted to a polynomial in ρ of the form

$$Z(\rho) = \sum_{i=1}^{m} b_i \, \rho^{i-1} .$$

The explicit expression of the free energy at a nematic density ρ is thus given by

$$f(\rho) = f_{\mathrm{ref}} + b_1 \ln\left(\frac{\rho}{\rho_{\mathrm{ref}}}\right) + \sum_{i=2}^{m} \frac{b_i}{i-1} (\rho^{i-1} - \rho_{\mathrm{ref}}^{i-1}) .$$

Variations of this method have also been employed in this work. They will be explained when appropriate.

2.5 Free energy of solids. Einstein crystal method

2.5.1 Simple crystals

There exists no natural reversible path from the solid phase to the isotropic phase, so this path must be constructed artificially. One possibility was proposed by Hoover and Ree [34] who introduced the single-occupancy cell method in which each particle is assigned to one lattice point and can only move around this lattice point. At high density, the properties of the cell

system resembles those of a perfect solid. The cell system can be reversibly expanded to low density without melting. Hoover and co-workers [35, 36] proposed in 1970 an alternative to the single-occupancy cell method: the solid is cooled to a temperature sufficiently low such that the system behaves as an harmonic crystal, the free energy of which can be calculated analytically. It was concluded that actually both methods suffer from some limitations.

In 1984, Frenkel and Ladd [37] proposed another method to calculate the free energy of the solid phase using parametric integration. The basic idea is to reversibly transform the solid under study into an ideal Einstein crystal (EC)[8] connecting the atoms to their lattice sites. Some years later, the method was revised by Polson *et al.* [38]. The EC method was extended to molecular solids by Frenkel and Mulder [11]. More recently, Vega and Noya [39] have proposed a slightly different version of the Frenkel-Ladd method named the Einstein molecule method in which, instead of fixing the center of mass of the system, one fixes the position of a reference molecule. An extension of the EC method has recently been proposed by Almarza [40] and applied to the computation of the free energy in systems of hard spheres. Wilding and co-workers [41,42] have proposed the phase switch Monte Carlo method, which has been applied to study the free energy difference between the fcc and hcp crystalline solids, and to obtain the fluid-solid transition of hard spheres for different system sizes.

In the present work, we apply the EC method for the calculation of the free energy of crystalline structures of atomic systems consisting of hard spheres, and of molecular systems of molecules interacting with the hard Gaussian overlap model, with and without attractive interactions. In the following, we describe this method in some length. We restrict ourselves to atomic systems with hard-core interactions.

Let us consider a system of atoms that interact with an intermolecular potential $\mathcal{U}_0(\mathbf{r}^N)$. The thermodynamic path that links the system with an ideal EC is defined by the following family of interactions

$$\mathcal{U}(\mathbf{r}^N;\chi,\lambda_t) = \chi\,\mathcal{U}_0(\mathbf{r}^N) + \lambda_t \sum_{i=1}^{N} (\mathbf{r}_i - \mathbf{r}_i^0)^2/D^2\,, \tag{2.57}$$

where D is some arbitrary length scale in the interaction model, $\mathbf{r}_i$ is the position of particle i, and $\mathbf{r}_i^0$ corresponds to the lattice positions of the EC. This lattice must have the same crystalline structure as the solid under

[8]The term ideal EC is used in this context to refer to a solid with harmonic interactions but without intermolecular interactions. This will also be referred to as a non-interacting EC.

study. Also, the number density must remain constant along the thermodynamic path. λ_t in Eq. (2.57) is the strength of the harmonic springs, and χ is a dimensionless parameter that tunes the hard-core interactions from a non-interacting ($\chi = 0$) to an interacting ($\chi = 1$) system. For numerical reasons [37, 38], it is usual practice to consider the non-interacting EC with fixed center of mass as reference state and compute the change in free energy under the constraint of fixing the center of mass. The reduced Helmholtz free energy of the solid phase can then be expressed as

$$f = f_{\rm EC}^{\rm CM} + \Delta f_{\chi}^{\rm CM} + \Delta f_{\lambda_t}^{\rm CM} + \Delta f^{\rm CM} \,. \tag{2.58}$$

$f_{\rm EC}^{\rm CM}$ represents the free energy of the ideal EC with fixed center of mass and strength of the harmonic springs λ_t. As shown in Appendix A, this is given by

$$f_{\rm EC}^{\rm CM} = -\frac{3}{2}\ln\left(\frac{\pi}{\beta\lambda_t}\right) - \frac{3}{2N}\ln\left(\frac{\beta\lambda_t}{\pi}\right) . \tag{2.59}$$

$\Delta f_{\chi}^{\rm CM}$ is the difference in free energy between the interacting ($\chi = 1$) and non-interacting ($\chi = 0$) EC for a fixed value of the coupling parameter λ_t. In principle, one can compute this contribution from

$$\Delta f_{\chi}^{\rm CM} = -\frac{1}{N}\ln\langle \exp(-\beta \mathcal{U}_0)\rangle_{\rm EC} \,,$$

where the average of the Boltzmann factor is obtained by sampling the configuration space of the non-interacting EC. However, the computation of this contribution using the expanded ensemble technique turns out to yield more accurate values.

$\Delta f_{\lambda_t}^{\rm CM}$ is the difference in free energy when the harmonic interactions are switched off with the constraint on the center of mass. In most instances, this contribution is computed from parametric integration [cf. Eq. (2.30)], using the strength of the harmonic springs as the integration parameter. The explicit expression is

$$\Delta f_{\lambda_t}^{\rm CM} = -\frac{1}{N{\rm k_B}T}\int_0^{\lambda_t} d\lambda \left\langle \sum_{i=1}^{N} (\mathbf{r}_i - \mathbf{r}_i^0)^2/D^2 \right\rangle_{\lambda} . \tag{2.60}$$

$\Delta f^{\rm CM}$ is the contribution due to the constraint on the center of mass. This is given by [38]

$$\Delta f^{\rm CM} = \frac{1}{N}\ln(\rho D^3) - \frac{3}{2N}\ln N \,. \tag{2.61}$$

2.5.2 Molecular crystals

The molecular models considered in this project are appropriate for uniaxial molecules. The extension of the EC method to molecular crystals was proposed by Frenkel and Mulder [11], and first implemented for systems of hard ellipsoids of revolution. The method is described here for systems of uniaxial hard particles of arbitrary shape. The thermodynamic path that links the target molecular solid with the ideal EC is defined as

$$\mathcal{U}(\mathbf{r}^N, \mathbf{\Omega}^N; \chi, \lambda_t, \lambda_r) = \chi\, \mathcal{U}_0(\mathbf{r}^N, \mathbf{\Omega}^N) + \lambda_t \sum_{i=1}^{N} (\mathbf{r}_i - \mathbf{r}_i^0)^2/D^2 + \lambda_r \sum_{i=1}^{N} \sin^2\theta_i \,. \tag{2.62}$$

This familiy of interactions is similar to the one used for the EC method as applied to atomic systems [cf. Eq. (2.57)], but now including an extra term that represents an orienting field. λ_r is the strength of the field, and θ_i is the angle between the main axis of molecule i with the direction of the field. The latter should be consistent with the symmetry of the solid phase. For all of the cases considered here, the main molecular axes are parallel to each other, so that the orienting field is applied along this direction.

The Helmholtz free energy of the molecular solid is given by an expression similar to Eq. (2.58). The explicit expression is

$$f = f_{\rm EC}^{\rm CM} + \Delta f_{\chi}^{\rm CM} + \Delta f_{\lambda_t,\lambda_r}^{\rm CM} + \Delta f^{\rm CM} \,, \tag{2.63}$$

where $f_{\rm EC}^{\rm CM}$ is the free energy of a molecular EC with fixed center of mass. At variance with the atomic EC, molecules are now perfectly oriented. The corresponding expression for the free energy reads

$$f_{\rm EC}^{\rm CM} = -\frac{3}{2}\ln\left(\frac{\pi}{\beta\lambda_t}\right) - \frac{3}{2N}\ln\left(\frac{\beta\lambda_t}{\pi}\right) - \ln q_{\lambda_r} \,, \tag{2.64}$$

where the last term accounts for the contribution arising from the orienting field, with q_{λ_r} given by Eq. (2.55)

$$q_{\lambda_r} = \int_0^1 dx\ \exp\left[-\beta\lambda_r\left(1-x^2\right)\right] \,. \tag{2.65}$$

The contribution $\Delta f_{\lambda_t,\lambda_r}^{\rm CM}$ in Eq. (2.63) represents the reversible work associated with disconnecting the translational and rotational fields. Both are

disconnected simultaneously at constant density. For convenience, the integration path is defined in terms of a single parameter ξ. The translational and rotational couplings are written as $\lambda_t = \xi$ and $\lambda_r = C\xi$, where C is a constant. Using parametric integration [cf. Eq. (2.30)] with ξ as the integration parameter, one arrives to

$$\Delta f_{\xi}^{\mathrm{CM}} \equiv \Delta f_{\lambda_t,\lambda_r}^{\mathrm{CM}} = -\int_0^{\xi} d\xi' \left[\left(\frac{\partial f}{\partial \lambda_t} \right) + C \left(\frac{\partial f}{\partial \lambda_r} \right) \right] . \tag{2.66}$$

Using Eq. (2.30) with $\mathcal{U}$ given by Eq. (2.62), one finds

$$\Delta f_{\xi}^{\mathrm{CM}} = -\frac{1}{N k_{\mathrm{B}} T} \int_0^{\xi} d\xi' \left\langle \sum_{i=1}^{N} (\mathbf{r}_i - \mathbf{r}_i^0)^2 / D^2 + C \sum_{i=1}^{N} \sin^2 \theta_i \right\rangle_{\xi'} . \tag{2.67}$$

2.6 Gibbs-Duhem integration

So far, we have described methods for the computation of the free energy of fluid and solid phases. The free energies enable one to determine the coexistence properties of first-order phase transitions by imposing the conditions of phase equilibria. In principle, this process could be repeated for different values of the molecular parameters. However, this is very time consuming; as an alternative we use the Gibbs-Duhem integration method to trace the phase boundaries between phases separated by first-order transitions. The method was originally proposed by Kofke [43, 44] and is based on a numerical integration of a generalized Clausius-Clapeyron equation. The basic idea of the method consists on performing simultaneous simulations of the two phases along the coexistence line starting from coexistence at a given point. In each of these simulations, the pressure of the system is adjusted so that the coexistence condition involving the equality of chemical potential is satisfied.

Since its introduction, the Gibbs-Duhem integration method has been applied to determine the vapour-liquid, vapour-solid, and liquid-solid coexistence lines in simple [45–48] and complex models [16, 49–56]. In his original work, Kofke applied the Gibbs-Duhem integration method to determine the vapour-liquid coexistence in the Lennard-Jones model. Lisal *et al.* [46] has determined the vapour-liquid equilibria of dipolar two-centre Lennard-Jones fluids. Camp *et al.* [49] applied the method to trace out the isotropic-nematic coexistence line in systems of uniaxial hard ellipsoids. They later determined the isotropic-nematic and isotropic-discotic coexistence lines in systems of biaxial hard ellipsoids [50]. Polson and Frenkel [52] calculated the full solid-fluid coexistence line for systems of chain molecules, investigating the effect

of chain stiffness on the transition. Galindo et *al.* [55] determined the solid-fluid coexistence properties of linear rigid Lennard-Jones chain molecules; they compare the results with those obtained for flexible models. de Miguel and del Río [16] have investigated the isotropic-nematic transition for the hard Gaussian overlap model for a range of molecular elongations using this technique. The phase behaviour of the square-well model has been studied by Liu *et al.* [48] for different values of the attractive range. The vapour-liquid and liquid-solid coexistence lines in binary Lennard-Jones mixtures have been determined from the Gibbs-Duhem method by Lamm and Hall [54]. Other examples include the study of the phase diagram of binary metallic alloys [51]. A comprehensive review of the method and its applications can be found in Ref. [57].

2.6.1 Temperature Gibbs-Duhem integration

We consider a system that exhibits a first-order transition between two phases 1, 2. An infinitesimal change of the Gibbs free energy can be expressed as

$$d\mu = \left(\frac{\partial \mu}{\partial T}\right)_P dT + \left(\frac{\partial \mu}{\partial P}\right)_T dP = -sdT + vdP\,, \tag{2.68}$$

where μ is the chemical potential, s is the entropy per particle, and v is the volume per particle. According to the coexistence conditions Eq. (2.1), the condition $\Delta\mu = \mu_1 - \mu_2 = 0$ must be satisfied along the coexistence line.

The Gibbs-Duhem integration method is based on the numerical integration of the Clapeyron equation. This equation follows from equating Eq. (2.68) for the two coexisting phases

$$\left(\frac{dP}{dT}\right)_{\text{coex}} = \frac{\Delta h}{T\Delta v} = \Phi(P,T)\,, \tag{2.69}$$

where $\Delta h = h_1 - h_2$ and $\Delta v = v_1 - v_2$ represent the difference in enthalpy and volume per particle between the two coexisting phases, respectively. The first-order derivative appearing in Eq. (2.69) is taken along the coexistence line.

The numerical solution of the Clapeyron equation can be accomplished by using different methods. Having calculated the coexistence pressure P_{o} at a given temperature T_{o}, one wants to determine the coexistence pressure P_{n} at a new temperature T_{n}. This first-order differential equation is solved here by using a fourth-order Runge-Kutta algorithm. The practical implementation of this algoritm involves the following steps:

1. Simultaneous NPT simulations are performed for the two coexisting phases at $P_{\rm o}$ and $T_{\rm o}$. Averages of the enthalpy and volume for each phase are calculated at these conditions and used to evaluate $\Phi_1 = \Phi(P_{\rm o}, T_{\rm o})$ defined in Eq. (2.69).

2. A predicted value of the coexistence pressure at temperature $T_{\rm h} = T_{\rm o} + \Delta T/2$ is obtained from

$$P_{\rm h}^{\rm p} = P_{\rm o} + \frac{\Delta T}{2}\Phi_1 \,,$$

   where ΔT is the integration step. An NPT simulation is then carried out at $P_{\rm h}^{\rm p}$ and $T_{\rm h}$ in order to compute $\Phi_2 = \Phi(P_{\rm h}^{\rm p}, T_{\rm h})$.

3. A corrected value of the coexistence pressure at $T_{\rm h}$, given by

$$P_{\rm h}^{\rm c} = P_{\rm o} + \frac{\Delta T}{2}\Phi_2 \,,$$

   is used as the input pressure in an NPT simulation. A new value $\Phi_3 = \Phi(P_{\rm h}^{\rm c}, T_{\rm h})$ is then computed.

4. A new value of the pressure is predicted at temperature $T_{\rm n}$

$$P_{\rm n}^{\rm p} = P_{\rm o} + \Delta T \Phi_3 \,,$$

   $\Phi_4 = \Phi(P_{\rm n}^{\rm p}, T_{\rm n})$ is determined in an NPT simulation at input conditions $P_{\rm n}^{\rm p}$ and $T_{\rm n}$.

The coexistence pressure at temperature $T_{\rm n}$ follows from [24]:

$$P_{\rm n} = P_{\rm o} + \frac{\Delta T}{6}(\Phi_1 + 2\Phi_2 + 2\Phi_3 + \Phi_4) \,. \tag{2.70}$$

2.6.2 Parametric Gibbs-Duhem integration

We describe here a variant of the Gibbs-Duhem method which will be used to determine the phase diagram of the hard Gaussian overlap model. We will restrict ourselves to hard-core systems, where the temperature plays no thermodynamic role. We consider a system that exhibits a first-order transition between phases 1 and 2. An infinitesimal change in the chemical potential can be written as

$$d\mu = \left(\frac{\partial \mu}{\partial P}\right)_x dP + \left(\frac{\partial \mu}{\partial x}\right)_P dx = v dP + \Omega dx \,, \tag{2.71}$$

where x is an arbitrary parameter that enters into the intermolecular interactions. Using that $\Delta\mu = 0$ at coexistence, it follows that

$$\Delta v dP + \Delta\Omega dx = 0\,,$$

where $\Delta v = v_1 - v_2$ and $\Delta\Omega = \Omega_1 - \Omega_2$. It follows that

$$\left(\frac{dP}{dx}\right)_{\rm coex} = -\frac{\Delta\Omega}{\Delta v} = \Phi(x,P)\,. \tag{2.72}$$

This is a Clausius-Clapeyron type equation. In general, Ω can not be related to a trivial thermodynamic property. A general procedure for its computation involves the following perturbation-based approach. According to its definition, Ω is given by

$$\Omega = \left(\frac{\partial\mu}{\partial x}\right)_P = \frac{1}{N}\left(\frac{\partial G}{\partial x}\right)_P\,, \tag{2.73}$$

where G is the Gibbs free energy, which is related to the isobaric partition function $Q \equiv Q(x)$ by

$$G = -k_{\rm B}T\ln Q\,. \tag{2.74}$$

The partition function in the NPT ensemble can be written as

$$Q(x) = \frac{1}{N!}\frac{1}{\Lambda_t^{3N}\Lambda_r^N}\int dV\exp\left(-\beta PV\right)\int d\Gamma\exp\left[-\beta\mathcal{U}(\Gamma;x)\right]\,. \tag{2.75}$$

Differentiating Eq. (2.74) with respect to x at constant P yields[9]

$$\left(\frac{\partial G}{\partial x}\right)_P = -k_{\rm B}T\frac{\partial\ln Q(x)}{\partial x} = -k_{\rm B}T\lim_{\delta x\to 0}\left[\frac{\ln Q(x+\delta x)-\ln Q(x)}{\delta x}\right]\,.$$

Inserting (2.75) in the above equation, we obtain

$$\left(\frac{\partial G}{\partial x}\right)_P = -k_{\rm B}T\lim_{\delta x\to 0}\left\{\frac{1}{\delta x}\ln\left[\frac{\int dV\exp(-\beta PV)\int d\Gamma\exp(-\beta\Delta\mathcal{U})\exp(-\beta\mathcal{U})}{\int dV\exp(-\beta PV)\int d\Gamma\exp(-\beta\mathcal{U})}\right]\right\}\,,$$

where $\Delta\mathcal{U} = \mathcal{U}(\Gamma;x+\delta x) - \mathcal{U}(\Gamma;x)$ represents the energy associated with a small perturbation in which x is changed to $x+\delta x$ at constant pressure. The above expression can be rewritten as an ensemble average. It follows that

$$\left(\frac{\partial G}{\partial x}\right)_P = -k_{\rm B}T\lim_{\delta x\to 0}\left\{\frac{1}{\delta x}\ln\left\langle\exp(-\beta\Delta\mathcal{U})\right\rangle\right\}\,. \tag{2.76}$$

According to its definition (2.73), Ω can be finally computed from

$$\Omega = -\frac{k_{\rm B}T}{N}\lim_{\delta x\to 0}\left\{\frac{1}{\delta x}\ln\left\langle\exp(-\beta\Delta\mathcal{U})\right\rangle\right\}\,. \tag{2.77}$$

[9]We are implicitly assuming here that the ideal contribution does not depend on the parameter x. A particular application where this is not the case will appear later.

Chapter 3

Free energy of the hard-sphere solid

We investigate in this chapter the system-size dependence of the free energy of crystalline solids as obtained from simulation experiments [26]. We consider a path at constant density which connects the solid under study with the reference state (a non-interacting Einstein crystal with fixed center of mass position). The free energy along this path is computed from simulations in the expanded ensemble [22] and our results are compared with those obtained by typical integration of the derivative of the free energy using Gaussian quadrature [38]. It is found that the free energy exhibits a strong dependence with system size. We study the face-centered cubic (fcc) and hexagonal close-packed phases of the hard-sphere (HS) system at a density close to the melting transition. A possible dependence of the free energy of the solid phase with the shape of the simulation box is analyzed. We also investigate the effect on the free energy of the orientation of the close-packed crystal layers with respect to the simulation cell. The fcc phase is found to be the stable one close to melting. The value of the free energy in the thermodynamic limit is in agreement with existing data.

3.1 Introduction

Since the first simulations of the fluid-solid transition of a system of hard spheres [3, 58], considerable work has been done on this system. Direct coexistence methods [59, 60] and methods based on free energy calculations [17] have been used to determine the fluid-solid transition properties.

When direct coexistence methods are used, the fluid-solid coexistence properties are estimated from a simulation of the two phases under co-

existence conditions. This approach was first used by Ladd and Woodcock [61, 62].

The most commonly used approach to the calculation of the free energy of a solid is based on the Einstein crystal (EC) method presented in the preceding chapter. In this method, one considers a reversible path connecting the solid under consideration with a reference state (a non-interacting or ideal EC), the free energy of which can be computed analytically. The accuracy of the calculated free energies relies to a large extent on the efficient computation of the change in free energy when the coupling parameter for the strength of the harmonic interactions is switched off. In most applications, the computation of the free energy involves performing a number of independent simulations along the chosen path. The free energy difference is then obtained from numerical integration of the derivative of the free energy using an appropriate quadrature scheme. Chang and Sandler [63] have recently suggested an alternative approach based on the expanded ensemble technique [22] that avoids the numerical integration: the free energy difference along the thermodynamic path follows from a direct determination of the difference between the free energies of adjacent states defined along the path. This approach has been subsequently applied to the calculation of the free energy in different problems involving crystalline phases [25, 64, 65]. Other certainly appealing techniques have been proposed to date [41, 66, 67].

In their original work, Chang and Sandler [63] consider the application of the method to the calculation of the free energy of a defect-free face-centered cubic (fcc) phase of a HS solid at a fixed number density close to the melting transition for different sizes of the (cubic) simulation cell. According to their results, the excess free energy appears to exhibit a weak dependence with system size, which is at variance with the much stronger dependence previously reported by Polson *et al.* [38]. Chang and Sandler claim that this large difference might be due to the use of boxes of different (cubic vs non-cubic) shapes in the simulations[1]. This effect appears to be quite significant for small system sizes; on the other hand, both sets of data yield a fully consistent estimate of the limiting value of the excess free energy in the thermodynamic limit. Incidentally, we note that Frenkel and Ladd [37] had suggested the existence of a dependence of the free energy with box shape based on the different values of the free energy obtained for systems of $N = 108$ hard spheres from simulations in cubic and non-cubic boxes. However, the difference is small and cannot be reconciled with the data reported by Chang and Sandler.

[1]The simulation boxes used by Polson *et al.* [38] are most likely non-cubic and not cubic as the authors claim.

3.2 Simulation methodology

The so-called EC method [37] has become a standard simulation technique to compute the Helmholtz free energy of solids. The method is based upon transforming the solid under consideration into a non-interacting EC crystal with the same structure (reference state), the free energy of which is known exactly. In the previous chapter we gave a full description of the EC method for the computation of the free energy of a reference solid state. Here, we will just write down the general expressions and apply the EC method to a system of hard spheres. For a system of N hard spheres, the path linking the solid and the reference state can be appropriately defined through the following biparametric potential [63]

$$\mathcal{U}(\mathbf{r}^N;\chi,\lambda) = \chi\mathcal{U}(\mathbf{r}^N) + \lambda\sum_{i=1}^{N}(\mathbf{r}_i - \mathbf{r}_i^0)^2/D^2\,, \tag{3.1}$$

where D is the diameter of the hard spheres, and $\mathbf{r}_i$ is the position of particle i, with $i = 1,\ldots,N$. χ and λ in Eq. (3.1) are coupling parameters that define the path connecting the solid under consideration ($\chi = 1$, $\lambda = 0$) with the non-interacting EC ($\chi = 0$, $\lambda \neq 0$), where λ sets the strength of the harmonic interactions. $\mathbf{r}_i^0$ ($i = 1,\ldots,N$) in Eq. (3.1) correspond to the lattice positions of the EC with the same structure as the equilibrium structure of the solid. As argued in the previous chapter, it is usual practice for numerical reasons [37, 38] to consider the non-interacting EC with fixed center of mass as reference state and compute the change in free energy under the constraint of fixing the center of mass. The Helmholtz free energy of the solid phase can then be expressed as

$$f = f_{\rm EC}^{\rm CM} + \Delta f_{\chi}^{\rm CM} + \Delta f_{\lambda}^{\rm CM} + \Delta f^{\rm CM}\,, \tag{3.2}$$

where f stands for $f \equiv F/(Nk_BT)$. Here, $f_{\rm EC}^{\rm CM}$ represents the free energy of the EC with fixed center of mass, which is explicitly given by [38] (see also Appendix A)

$$f_{\rm EC}^{\rm CM} = -\frac{3}{2}\ln\left(\frac{\pi}{\beta\lambda}\right) - \frac{3}{2N}\ln\left(\frac{\beta\lambda}{\pi}\right)\,. \tag{3.3}$$

The last term on the right-hand side of Eq. (3.3) corresponds to the decrease in free energy due to the constraint of fixing the center of mass [38]. $\Delta f_{\chi}^{\rm CM} \equiv f^{\rm CM}(\chi = 1,\lambda) - f^{\rm CM}(\chi = 0,\lambda)$ in Eq. (3.2) represents the free energy difference between the EC with HS interactions ($\chi = 1$) and the non-interacting ($\chi = 0$) crystal for a fixed value of the coupling parameter λ and with fixed center of mass. This contribution is expected to be small for sufficently

strong harmonic couplings. $\Delta f_\lambda^{\rm CM} \equiv f^{\rm CM}(\chi=1,\lambda) - f^{\rm CM}(\chi=1,\lambda=0)$ in Eq. (3.2) represents the change in free energy associated with switching off the harmonic interactions. One should note that $f^{\rm CM}(\chi=1,\lambda=0)$ corresponds to the free energy of the solid with fixed center of mass. The free energy of the solid is finally obtained after adding the contribution due to the constraint on the center of mass. According to Polson *et al.* [38] this contribution, denoted by $\Delta f^{\rm CM}$ in Eq. (3.2), is given by

$$\Delta f^{\rm CM} \equiv f(\chi=1,\lambda=0) - f^{\rm CM}(\chi=1,\lambda=0) = \frac{1}{N}\ln(\rho D^3) - \frac{3}{2N}\ln N\,, \tag{3.4}$$

where $\rho = N/V$ is the number density, with V being the volume of the system. The free energy difference between the system with coupling parameter λ and the HS crystal is typically computed from integration of the derivative of the free energy along the thermodynamic path. This can be expressed as

$$\begin{aligned}\Delta f_\lambda^{\rm CM} &= -\frac{1}{Nk_BT}\int_0^\lambda d\lambda' \left\langle \frac{\partial \mathcal{U}^{\rm CM}(\mathbf{r}^N;\lambda',\chi)}{\partial\lambda'}\right\rangle_{\lambda'} \\ &= -\frac{1}{Nk_BT}\int_0^\lambda d\lambda' \left\langle \sum_{i=1}^N (\mathbf{r}_i - \mathbf{r}_i^0)^2/D^2 \right\rangle_{\lambda'}\,,\end{aligned} \tag{3.5}$$

where $\mathcal{U}^{\rm CM}(\mathbf{r}^N;\chi,\lambda)$ stands for the potential defined by Eq. (3.1) with the additional constraint of fixed center of mass. In practice, the integration in Eq. (3.5) involves a computation of the average value of the derivative of the free energy (here, the mean square displacement of the particles from their lattice positions) in a series of constant-volume simulations for varying values of the coupling parameter λ. Typically, a 10-point Gaussian quadrature is used to perform this numerical integration. Instead, we follow the approach of Chang and Sandler [63] and make use of the expanded ensemble technique. This involves a sampling of the configuration space of a set of M subsensembles each representative of a system characterized by an interaction energy $\mathcal{U}_m \equiv \mathcal{U}(\mathbf{r}^N;\xi_m)$, with $m = 1,\ldots,M$, where ξ_m is an arbitrary set of parameters (here taken as the strength of the harmonic interactions). As shown in §2.3.3, the key expression of the expanded simulation technique [see Eq. (2.37)],

$$f_n - f_m = -\frac{1}{N}\ln\frac{p_n}{p_m} + (\omega_n - \omega_m)\,, \tag{3.6}$$

allows for the computation of the difference in free energy between two arbitrary subsystems. We recall that $w_k = \beta W_k/N$, where W_k is a weight factor for the potential $\mathcal{U}_k$, and p_k is the probability of finding the system in the subensemble k. In addition to the usual MC moves, one also considers trial

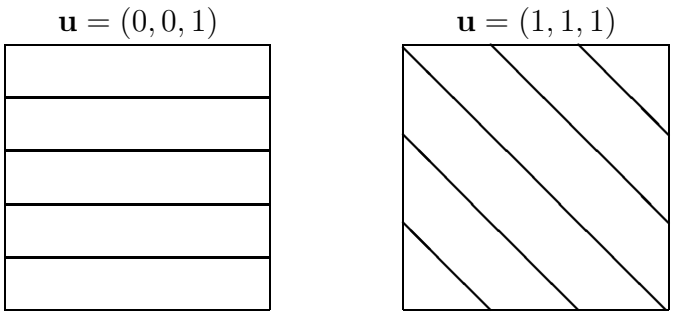

Figure 3.1: Schematic representation of the different orientations of the closed-packed layers used for the simulation of the HS solid. $\mathbf{u}$ is a vector that defines the normal to the closed-packed layers. The components of $\mathbf{u}$ are defined with respect to the simulation box.

moves that attempt to switch the system from one subensemble to another at constant volume, temperature, and number of particles. The probability of acceptance of such a transition is given by Eq. (2.38). The weight factors are refined during the equilibration stage of the simulation. We use for this purpose the iterative scheme embodied by Eq. (2.39). We observe that a few iterations are sufficient to obtain a corrected value of Δw_{mn} that ensures $p_m \approx p_n$. This procedure is repeated for the next pair of subsystems in the sequence. Following previous recommendations [63], the whole set of weight factors are simultaneously refined in a single simulation covering the full range of subsystems.

3.3 Results and discussion

We consider here the calculation of the Helmholtz free energy of the fcc and hcp phases of a HS solid for different box shapes and number of particles at a number density $\rho D^3 = 1.04086$. This value is close to the density of the solid phase at melting and is chosen so as to be able to compare with results reported by other authors.

Different setups are considered for generating the initial equilibrium solid structure. They are schematically depicted in Fig. 3.1. A first series of simulations is performed for the fcc phase with closed-packed planes oriented perpendicular to the direction defined by the (normal) vector $\mathbf{u} = (1, 1, 1)$, where the components are referred to a orthonormal basis defined along the

x, y, and z axis of the simulation box. The total number of particles is given by $N = 4n_x n_y n_z$, where n_x, n_y and n_z are the number of unit cells along each direction of the simulation box. The simulation cell is cubic if $n_x = n_y = n_z$, and non-cubic otherwise. This geometry will be referred hereafter as cubic (or non-cubic) fcc (1,1,1), where (1,1,1) denotes the components of vector $\mathbf{u}$. A second series of simulations is performed by setting the fcc phase with closed-packed planes perpendicular to the direction $\mathbf{u} = (0, 0, 1)$ (i.e., these planes are parallel to the x-y plane of the simulation box). The total number of particles is given by $N = n_x n_y n_z$, where $n_x \times n_y$ is the number of particles in each closed-packed layer, and n_z is the number of such layers; to fulfill the requirements imposed by the periodic boundary conditions, n_z is always chosen to be a multiple of three so as to reproduce the ABC stacking of the compact layers. In this case, the simulation box has always a non-cubic shape. This geometry will be referred hereafter as non-cubic fcc (0,0,1). The main difference between these two setups is therefore the relative orientation of the closed-packed layers with respect to the simulation box and, possibly, the shape of the box. Finally, we also consider a set of simulations with non-cubic hcp (0,0,1) structures, for which the only difference with the non-cubic fcc (0,0,1) structures is to be found in the ABAB arrangement of the compact layers perpendicular to the z axis of the simulation box. In this case, the number of closed-packed layers n_z has to be a multiple of two.

In principle, the free energy difference between the interacting and non-interacting EC with fixed center of mass ($\Delta f_\chi^{\mathrm{CM}}$ in Eq. (3.3)) could be calculated from

$$\Delta f_\chi^{\mathrm{CM}} = -\frac{1}{N} \ln \left\langle \exp\left(-\beta \Delta \mathcal{U}^{\mathrm{CM}}\right) \right\rangle_{\chi=0} , \tag{3.7}$$

with $\Delta \mathcal{U}^{\mathrm{CM}} = \mathcal{U}^{\mathrm{CM}}(\chi = 1; \lambda) - \mathcal{U}^{\mathrm{CM}}(\chi = 0; \lambda)$, where the average of the exponential is obtained by sampling the configuration space of the non-interacting ($\chi = 0$) EC. Though this (perturbation-based) expression is expected to be reliable (provided λ is large enough), we find that the computation of $\Delta f_\chi^{\mathrm{CM}}$ from a simulation in the expanded ensemble is generally more accurate. Its calculation for each of the cases considered here is accomplished in a single constant-volume simulation in the expanded ensemble with transitions between states characterized by $\chi = 0$ and $\chi = 1$ with the harmonic coupling set equal to $\lambda = 1000\, k_B T$. For all the lattice structures and for all the system sizes considered here, we find (on average) a value of 0.00178(2), which is essentially equal to the value of 0.0018 reported by Chang and Sandler [63] for Δf_χ without the constraint on the center of mass of the EC.

For the calculation of the free energy difference between the interacting EC with $\lambda = 1000\, k_B T$ and the HS solid with $\lambda = 0$ [$\Delta f_\lambda^{\mathrm{CM}}$ in Eq. (3.3)] we

follow a scheme similar to the one employed by Chang and Sandler [63]. The full range of values of λ is divided into a total of M windows (here, we consider $M = 9$), each containing either five or six values of λ. For each consecutive pair of values of λ within a window, we start from an educated guess for the difference of weight factors. This guess is corrected in the course of a preliminary short simulation as explained earlier [see Eq. (2.39)]. This stage typically involves 10^4 MC cycles, where one cycle consists of N attempts to translate the particles and one attempt to drive the system into an adjacent subensemble. A single simulation involving the full range of potentials within each window is then performed and the corresponding weight factors are refined over 10^5 MC cycles following the same prescription as before. This full scheme is just carried out for a single value of N (for each structure): for subsequent values of N, the set of weight factors appropriate for each window is directly refined over 10^5 MC cycles. Once the weight factors have been corrected, the probabilities of visiting each subensemble within a window are obtained in a single simulation involving 5×10^5 MC cycles. The change in free energy along each window follows from Eq. (3.6). The simulation run is divided into 20 blocks and an estimate of the uncertainty is obtained from the variance of the block averages. Our choice for the size of the windows is such that the change in free energy per particle is always smaller than 0.65 $k_{\mathrm{B}}T$ along the window. With the adopted windowing of the thermodynamic path and sampling length, we find that the free energy difference per particle in a window can be obtained, on average, within an uncertainty of about $(4.5 \times 10^{-4})k_{\mathrm{B}}T$ for the smallest system sizes and to within $(2.5 \times 10^{-4})k_{\mathrm{B}}T$ for the largest systems considered here. The free energy difference $\Delta f_\lambda^{\mathrm{CM}}$ is finally obtained by adding the corresponding results from the full set of $M = 9$ window simulations. In Fig. 3.2 we show the change in free energy, $\Delta f_\lambda^{\mathrm{CM}}$, when disconnecting the harmonic coupling as obtained from expanded ensemble simulations for a fcc (non-cubic) crystal HS for two system sizes; the orientation of the closed-packed layers is (0,0,1).

The different contributions to the absolute Helmholtz free energy of HS crystals have been gathered in Table 3.1. The last column in the table includes the values of the excess free energy, $f_{\mathrm{ex}} = f - f_{\mathrm{id}}$, where f_{id} is the free energy of the ideal gas at the same density. Within the Stirling approximation, it follows that

$$f_{\mathrm{id}} = \ln(\rho D^3) - 1 + \frac{1}{2N} \ln(2\pi N) \,. \tag{3.8}$$

For comparison, we have also computed $\Delta f_\lambda^{\mathrm{CM}}$ from a standard 10-point Gaussian quadrature for some of the systems considered here. As an example, a value of $\Delta f_\lambda^{\mathrm{CM}} = -3.6490(13)$ is found for the fcc cubic phase

Table 3.1: Relevant contributions to the free energy of a solid of HSs at a density of $\rho D^3 = 1.04086$, for different structures (fcc and hcp), shapes of the simulation box (cubic and non-cubic), and orientations of the closed-packed planes with respect to the simulation box [(1,1,1) and (0,0,1)]. N is the total number of particles. For (1,1,1) orientations, n_x, n_y and n_z are the number of units cells along each direction of the simulation box ($N = 4n_xn_yn_z$); for (0,0,1) orientations, $n_x \times n_y$ is the number of particles in the closed-packed planes, and n_z is the number of such layers along the z direction ($N = n_xn_yn_z$). $\Delta f_\chi^{\rm CM}$ is the free energy difference between the interacting and non-interacting EC with fixed center of mass and harmonic coupling $\lambda = 1000\,k_{\rm B}T$ as obtained in a single expanded-ensemble simulation; $\Delta f_\lambda^{\rm CM}$ is the free energy difference between the HS solid and an interacting EC with $\lambda = 1000\,k_{\rm B}T$ at the same density as obtained in a series of nine expanded ensemble simulations. The last two columns are the absolute (f) and excess ($f_{\rm ex}$) reduced free energy of the unconstrained solid.

N	$n_x \times n_y \times n_z$	$\Delta f_\chi^{\rm CM}$	$\Delta f_\lambda^{\rm CM}$	f	$f_{\rm ex}$
fcc cubic (1,1,1)					
256	$4 \times 4 \times 4$	0.00180(5)	−3.6500(13)	4.9302(13)	5.8757(13)
500	$5 \times 5 \times 5$	0.00177(3)	−3.6667(10)	4.9438(10)	5.8957(10)
864	$6 \times 6 \times 6$	0.00177(2)	−3.6749(9)	4.9497(9)	5.9046(9)
1372	$7 \times 7 \times 7$	0.00177(2)	−3.6794(7)	4.9527(7)	5.9094(7)
2048	$8 \times 8 \times 8$	0.00177(3)	−3.6820(7)	4.9545(7)	5.9121(7)
fcc non-cubic (1,1,1)					
216	$3 \times 3 \times 6$	0.00178(3)	−3.6443(13)	4.9248(13)	5.8681(13)
448	$4 \times 4 \times 7$	0.00179(3)	−3.6652(10)	4.9415(10)	5.8926(10)
700	$5 \times 5 \times 7$	0.00178(3)	−3.6729(8)	4.9471(8)	5.9010(8)
fcc non-cubic (0,0,1)					
216	$6 \times 6 \times 6$	0.00175(3)	−3.6463(15)	4.9228(15)	5.8660(15)
432	$6 \times 6 \times 12$	0.00178(2)	−3.6661(11)	4.9392(11)	5.8900(11)
576	$6 \times 8 \times 12$	0.00176(2)	−3.6708(10)	4.9440(10)	5.8969(10)
768	$8 \times 8 \times 12$	0.00176(2)	−3.6748(9)	4.9473(9)	5.9017(9)
1152	$8 \times 12 \times 12$	0.00177(2)	−3.6788(8)	4.9508(8)	5.9069(8)
2520	$12 \times 14 \times 15$	0.00178(4)	−3.6831(7)	4.9551(7)	5.9132(7)
hcp non-cubic (0,0,1)					
216	$6 \times 6 \times 6$	0.00179(4)	−3.6460(15)	4.9232(15)	5.8664(15)
432	$6 \times 6 \times 12$	0.00177(2)	−3.6653(11)	4.9402(11)	5.8908(12)
576	$6 \times 8 \times 12$	0.00177(2)	−3.6706(10)	4.9442(10)	5.8971(10)
768	$8 \times 8 \times 12$	0.00178(3)	−3.6734(9)	4.9487(9)	5.9032(9)
1152	$8 \times 12 \times 12$	0.00178(2)	−3.6777(8)	4.9520(8)	5.9081(8)
2352	$12 \times 14 \times 14$	0.00174(2)	−3.6821(7)	4.9556(7)	5.9135(7)

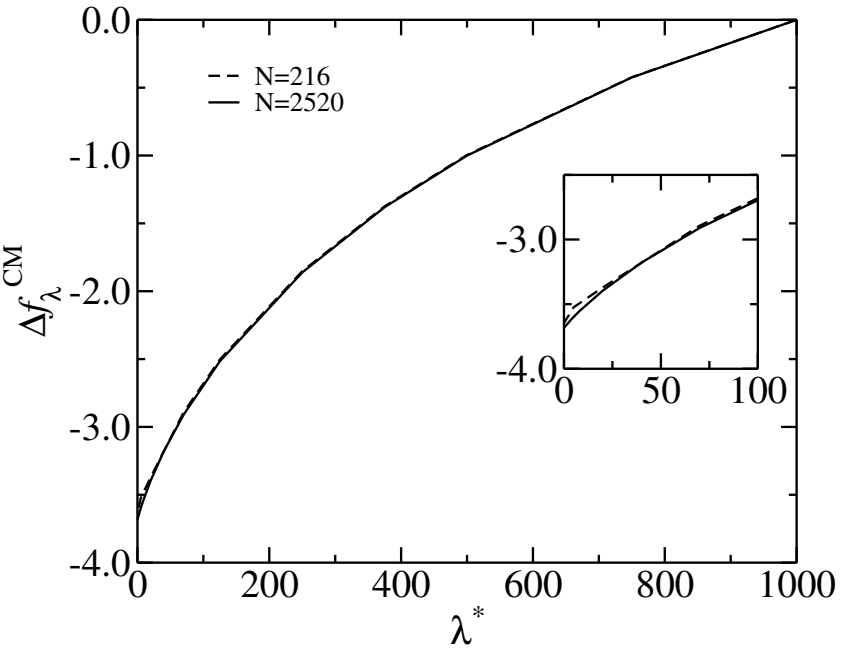

Figure 3.2: Change in free energy $\Delta f_\lambda^{\mathrm{CM}}$ when disconnecting the harmonic coupling $\lambda^* = \lambda / k_{\mathrm{B}}T$ for two different system sizes.

with $N = 256$. This value should be compared with the value $-3.6500(13)$ obtained from simulations in the expanded ensemble.

The excess free energy of the fcc phase for cubic simulation boxes (cubic fcc (1,1,1) geometry) is shown in Fig. 3.3 as a function of the inverse number of particles (N = 256, 500, 864, 1372, and 2048). We note that the values obtained here from expanded ensemble simulations exhibit the same behaviour with system size that was found by Polson *et al.* [38] using non-cubic boxes and a different scheme, in which the key contribution $\Delta f_\lambda^{\mathrm{CM}}$ is computed from numerical integration of the derivative of the free energy using a 10-point Gaussian quadrature (cf. Eq. (3.5)). Our results, however, are seen to be slightly higher for the smaller system sizes; the origin of this small difference will become clear later. As shown in Fig. 3.3, our data are at variance with those reported by Chang and Sandler [63], particularly for the smaller system sizes. In order to understand the nature of this discrepancy, one should note that Chang and Sandler consider a slightly different approach. In particular, they consider the unconstrained EC as the reference state and calculate the (absolute) free energy of the solid from expanded ensemble simulations along a path in which the harmonic coupling is varied without the constraint on the center of mass. This constraint is, however,

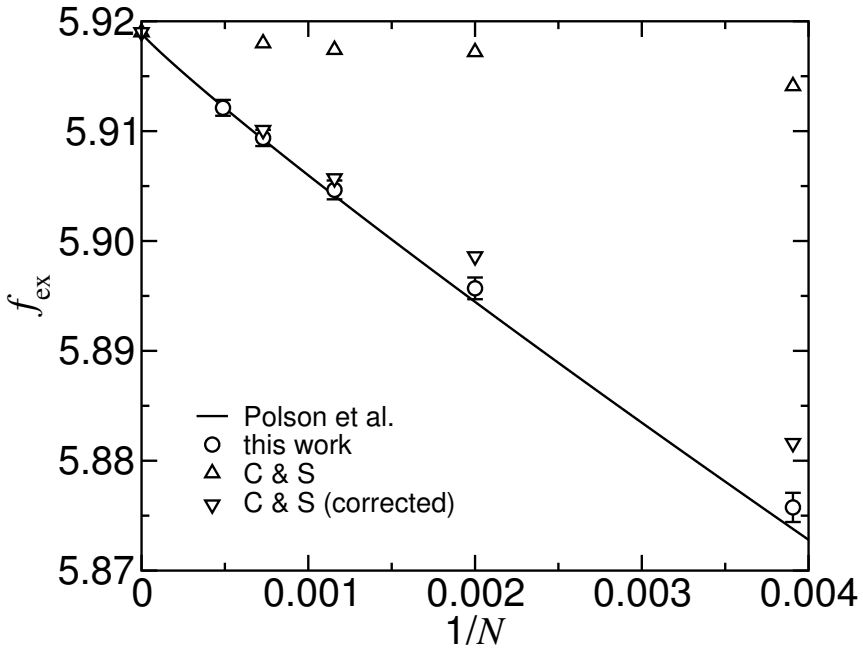

Figure 3.3: Excess free energy vs $1/N$ for the fcc HS crystal at a number density $\rho D^3 = 1.04086$ as obtained from simulations of cubic boxes with (1,1,1) orientation of the closed-packed layers (symbols). Circles are for the results obtained from expanded ensemble simulations (this work); triangles are for the results by Chang and Sandler [25] (C & S) as given in that reference (up triangles) and after correction for the (missing) $-3/(2N)\ln N$ term (down triangles). The solid line is a linear fit to the results of Polson *et al.* [38] obtained from simulations of non-cubic boxes with (0,0,1) geometry.

explicitly considered for transitions involving the state $\lambda = 0$ to avoid the drift of the center of mass when the particles of the crystal are no longer bounded harmonically to the sites of the underlying Einstein lattice. Using our notation, this procedure involves the following steps to compute the free energy of the solid phase

$$f = f_{\rm EC} + \Delta f_\chi + \Delta f(\lambda \to \lambda_0) + \Delta f(\lambda_0 \to 0) + \Delta f^{\rm CM}\,, \qquad (3.9)$$

where $f_{\rm EC}$ is the free energy of the unconstrained EC; Δf_χ has the same meaning as in Eq. (3.2), but without the constraint on the center of mass; $\Delta f(\lambda \to \lambda_0) = f(\lambda_0) - f(\lambda)$ is the change in free energy when the harmonic coupling is varied from λ to λ_0, with λ_0 being a value close to $\lambda = 0$; and $\Delta f(\lambda_0 \to 0) = f^{\rm CM}(\lambda = 0) - f(\lambda_0)$. The term $\Delta f^{\rm CM}$ in Eq. (3.9) is the correction due to the constraint on the center mass. This correction should be given by Eq. (3.4), but the last term in the right-hand side of that equation

(kinetic contribution) seems to be missing in Ref. [63]. This term vanishes in the limit $N \to \infty$, but turns out to be quantitatively important for small system sizes. When this (missing) term is explicitly added to the free energy data reported by Chang and Sandler, their results are seen to come to a closer agreement with those reported here (see Fig. 3.3). An inspection of Fig. 3.3, however, shows a persistent difference between the (corrected) data from Chang and Sandler and our results. At this stage, we are not able to give a fully convincing explanation for this difference, though it could be associated with the computation of $\Delta f(\lambda_0 \to 0)$ in Eq. (3.9) from expanded ensemble simulation[2]. We then conclude that the different system-size behaviour of the free energy found by Chang and Sandler and by Polson *et al.* is seemingly due to a missing N-dependent term in Ref. [63] and not to using different box shapes and number of particles, as the authors claim.

In spite of the above conclusion, one still may wonder the extent to which the free energy of the solid phase depends on the shape of the (finite sized) simulation box. This was already suggested by Frenkel and Ladd [37], who report a value of $f_{\rm ex} = 5.825(3)$ for a system of $N = 108$ hard spheres (fcc phase) in a cubic box, and a value of $f_{\rm ex} = 5.7932(8)$ for the same number of particles in a fcc (0,0,1) geometry with $n_x = n_y = 3$, $n_z = 12$ (these values of the free energy have been corrected for the extra term of the form $-2/N \ln N$ that was missing in Ref. [37]). This issue was not further investigated there and no definite conclusions on the (possible) dependence of the free energy on the box shape emerged from that work. We decided to investigate this point more systematically, computing the free energy of the fcc phase of the HS solid for different geometries of the simulation box. We start by considering systems with fcc (0,0,1) geometry containing $N = 216, 432, 576, 768, 1152,$ and 2520 particles (further details are included in Table 3.1). As explained earlier, all these cases correspond to non-cubic box shapes. The number density is set equal to $\rho D^3 = 1.04086$, as before. The free energy is calculated using essentially the same method as the one used for cubic box shapes; in particular, expanded ensemble simulations are performed to compute the free energy difference between the solid structure and the EC along a path in which the center of mass of the system is kept fixed. The key contributions to the free energy are collected in Table 3.1.

We show in Fig. 3.4 the variation of $f_{\rm ex} + \ln N/N$ with $1/N$ for systems with non-cubic fcc (0,0,1) geometry, along with the corresponding results for systems with cubic fcc (1,1,1) geometry. This way of presenting the data

[2]We find a bit tricky (and non-trivial) the implementation of the expanded ensemble technique when transitions from a state with fixed center of mass to a state without that constraint (or viceversa) are involved.

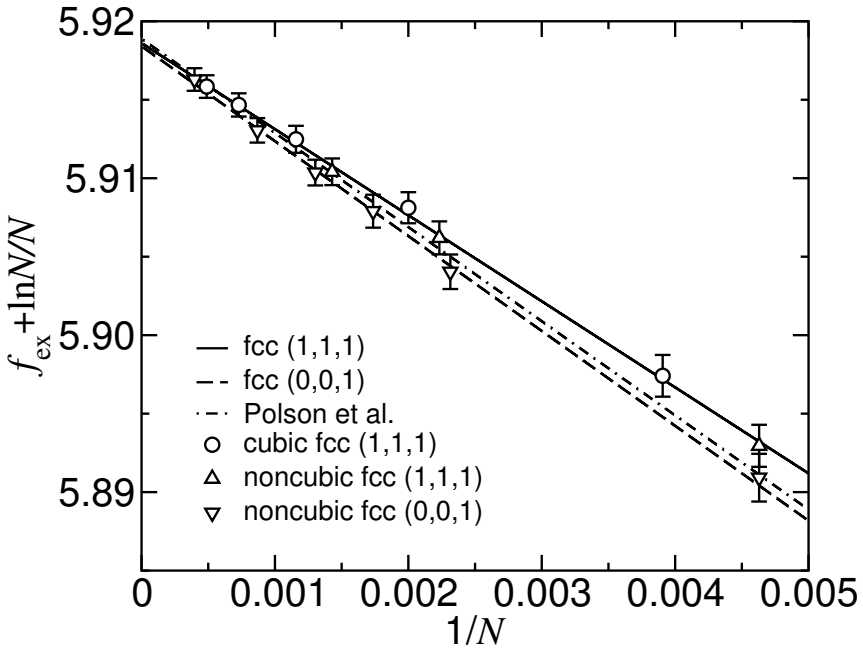

Figure 3.4: System-size dependence of the free energy of the fcc phase of a HS solid ($\rho D^3 = 1.04086$) for different orientations of the closed-packed layers with respect to the simulation box. The notation (1,1,1) and (0,0,1) denotes the components of the normal vector of these layers with respect to the axes of the simulation box. The lines are linear fits to the simulation data obtained with (1,1,1) orientations (solid line) and (0,0,1) orientations (long-dashed line). The dotted-dashed line corresponds to the fit of the data reported by Polson *et al.* [38] using different box shapes and number of particles.

follows from the fact that the leading finite-size correction term to the free energy per particle of the harmonic crystal is expected to be of the form $\ln N/N$ (in units of $k_{\rm B}T$), and the next higher-order term of the order of $1/N$ [34, 38]. In Fig. 3.4, we also include the free energy associated with non-cubic fcc (1,1,1) structures, in which $L_x = L_y$, but L_z is larger than the transverse dimension of the simulation box (see Table 3.1). The data included in Fig. 3.4 appear to corroborate the expected functional form of the finite-size corrections to the free energy (that is, linear behaviour of $f_{\rm ex} + \ln N/N$ with $1/N$) when the free energy data are analyzed in terms of the orientation of the closed-packed planes relative to the simulation box *irrespective of whether the box is cubic or non-cubic.*

The dependence of the excess free energy with the shape of the simulation box becomes apparent in Fig. 3.5, where $f_{\rm ex} + \ln N/N$ is shown for systems with cubic and non-cubic geometry and the same orientations of the closed

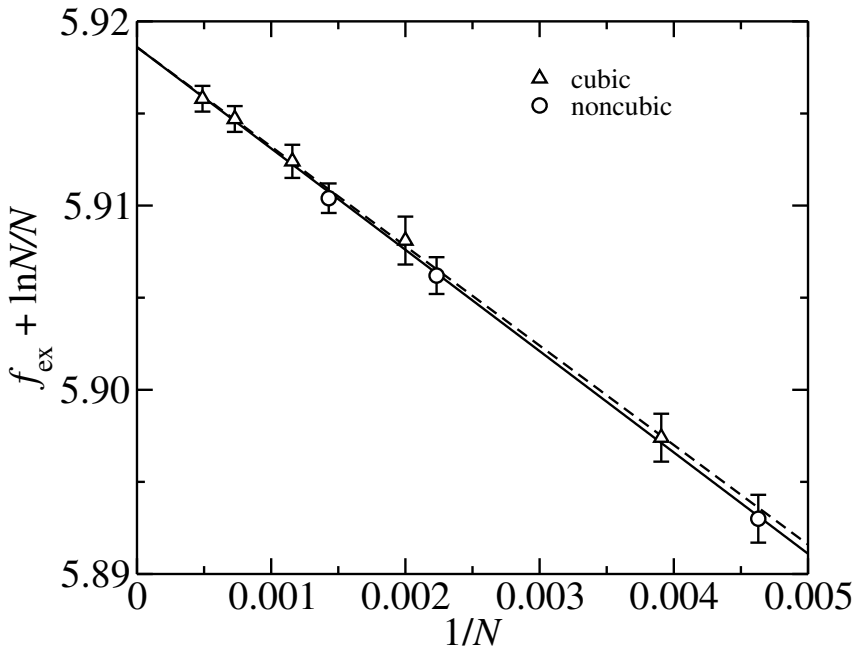

Figure 3.5: System-size dependence of the free energy of the fcc phase of a HS solid ($\rho D^3 = 1.04086$) for different shapes of the simulation box (cubic vs non-cubic) with the same orientation of the closed-packed layers (1,1,1). The triangles are data for the cubic shape and circles are data for the non-cubic shape. The lines are fits to the simulation data.

packed layers (1,1,1). The difference in free energy is small and becomes negligible in the thermodynamic limit. Referring to Fig. 3.4, we then conclude that solid phases with tilted closed-packed layers are characterized by values of the free energy higher than those found for non-tilted structures. This difference could be due to the fact that the system has to accomodate an ordered crystalline structure into a box of fixed shape and be compatible with periodic boundary conditions, this resulting in unbalanced strain on the system when the closed-packed planes are tilted. This effect is more noticeable for small systems and is expected to be negligible in the limit $N \to \infty$. Though the particular shape of the simulation box may still contribute to the free energy of a crystalline phase of finite size, our results depicted in Fig. 3.5 seem to indicate that this contribution is small in comparison to the contribution arising from the orientation of the compact crystal layers with respect to the simulation box.

Incidentally, we note that the (small) differences between our results and those of Polson *et al.* in Fig. 3.3 are simply due to the fact that we were comparing in that figure free energies of solids with different orientations:

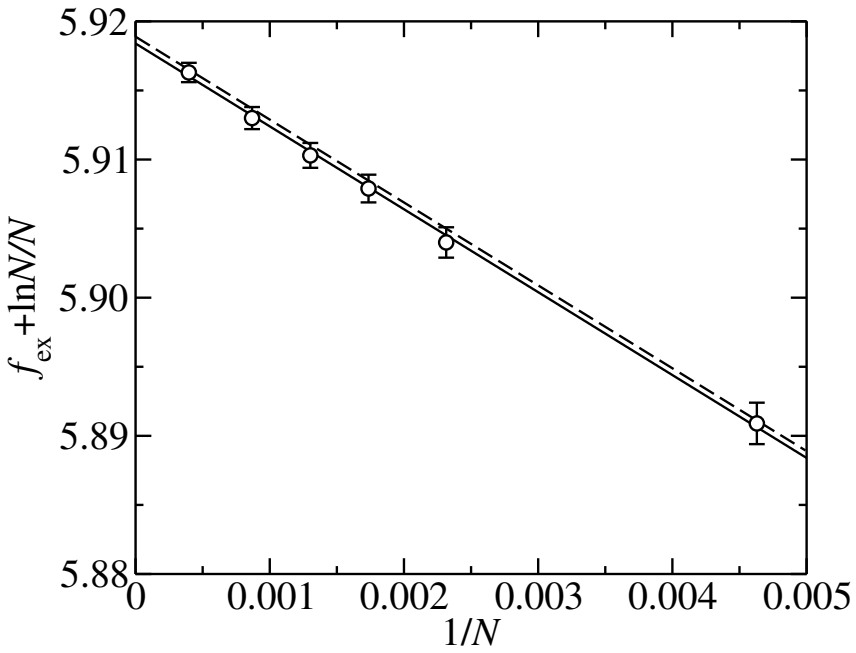

Figure 3.6: System-size dependence of the free energy of the fcc HS solid ($\rho D^3 = 1.04086$) for non-cubic fcc geometry with (0,0,1) orientation of the closed-packed layers with respect to the simulation box. Circles are data obtained in this work. The solid line is a linear fit to our results, and the dashed line is a fit of the simulation results of Polson *et al.* [38].

our results depicted in Fig. 3.3 correspond to systems with tilted compact layers, whereas those of Polson *et al.* are for systems with non-tilted compact layers. We note that under the same conditions, i.e. non-cubic fcc (0,0,1) geometry, our results obtained from expanded ensemble simulations are in agreement with those reported by Polson *et al.* from standard numerical integration (see Fig. 3.6).

We have also computed the free energy of the hcp phase of HS solids at the same density $\rho D^3 = 1.04086$ for different system sizes. In all cases, the simulation box is non-cubic; the set of closed-packed are placed parallel to the x-y plane of the simulation box and stacked following an ABAB pattern. Details on the number of molecules per layer and number of layers for each of the solid structures considered here are given in Table 3.1. Once again, we carry out expanded ensemble simulations to compute the free energy difference between the hcp phase and the EC (with the same structure) along a path in which the center of mass of the system is kept fixed. The resulting values of the free energy are collected in Table 3.1 and shown in Fig. 3.7, along with the corresponding values obtained for the fcc phase with ABC

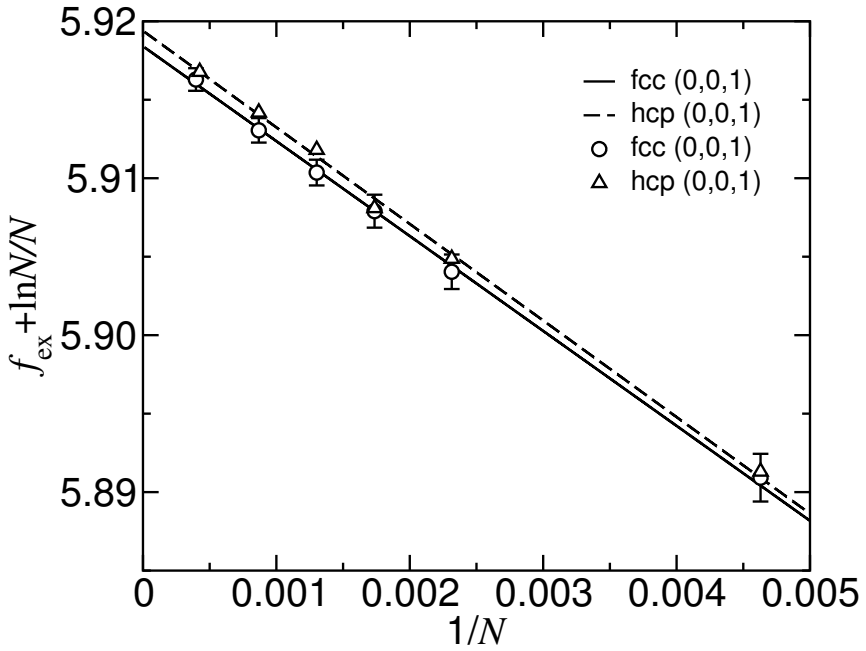

Figure 3.7: System-size dependence of the free energy of the fcc and hcp phases of a HS solid ($\rho D^3 = 1.04086$) with compact layers perpendicular to the direction (0,0,1). The lines are linear fits to the data points. The fcc is more stable than the hcp phase in the limit $N \to \infty$, the difference in free energy being $f_{\rm ex}^{\infty}(\text{hcp}) - f_{\rm ex}^{\infty}(\text{fcc}) = 0.0010(7)$.

stacking. For all system sizes, the fcc phase turns out to be more stable than its hcp counterpart, provided the orientation of the closed-packed planes with respect to the simulation box is the same in both phases.

In order to obtain the values of the free energy of the different structures in the limit $N \to \infty$, we regress our simulation data to a straight-line model $y(x) = a + bx$, with $x = 1/N$ and $y = f_{\rm ex} + \ln N/N$. The fitting coefficients a and b are obtained by minimizing the chi-square merit function of the model [24]

$$\chi^2(a,b) = \sum_{i=1}^{n} \left(\frac{y_i - a - bx_i}{\sigma_i} \right)^2 , \tag{3.10}$$

where n is the number of data points, and σ_i the uncertainty associated with each value of y_i. The resulting values of the fitting coefficients are included in Table 3.2.

Within the accuracy of the results, the value of the excess free energy of the fcc phase in the limit $N \to \infty$ is seen to be independent of the orientation

Table 3.2: Estimates of the excess free energy per particle (in units of k_BT) of the HS solid in the limit $N \to \infty$ as obtained from the linear fit $f_{\rm ex} + \ln N/N = a + b(1/N)$; a and b are (dimensionless) fitting coefficients, and r is the regression coefficient of the fit.

system	$a \equiv f_{\rm ex}^{\infty}$	b	r
fcc (1,1,1)	5.9186(5)	−5.5(3)	−0.99939
fcc (0,0,1)	5.9184(6)	−6.0(4)	−0.99948
hcp (0,0,1)	5.9194(6)	−6.1(4)	−0.99907

of the closed-packed layers. Our value of $f_{\rm ex}^{\infty} = 5.9184(6)$ obtained for the fcc (0,0,1) configuration is consistent with the value of $f_{\rm ex}^{\infty} = 5.91889(4)$ reported by Polson *et al.* for the same geometry. Also, the value of $f_{\rm ex}^{\infty} = 5.9186(5)$ found here for the fcc (1,1,1) crystal compares favorably with the value $f_{\rm ex}^{\infty} = 5.9190(5)$ reported by Chang and Sandler for the same geometry. The estimated value of the free energy in the thermodynamic limit is in agreement with data of Polson *et al.* [38], Chang and Sandler [63], Almarza [40], and Vega *et al.* [69].

When our data for the free energies of the fcc and hcp phases with the same (0,0,1) geometry are compared in the limit $N \to \infty$, we find that the fcc turns out to be more stable than the hcp phase, as has been reported elsewhere [37, 41, 66–68, 71]. The corresponding difference in free energy in the thermodynamic limit is found to be $f_{\rm ex}^{\infty}({\rm hcp}) - f_{\rm ex}^{\infty}({\rm fcc}) = 0.0010(7)$. This is consistent with the value of 0.0009(2) reported by Bolhuis *et al.* [68] at the same density but is not with the value of 0.0050(10) reported by Woodcock [72].

3.4 Conclusions

A quantitative study of the system-size dependence of the Helmholtz free energy of crystalline solids has been considered in this chapter. Our results are consistent with a linear dependence of $f_{\rm ex} + \ln N/N$ with the inverse number of particles, as first suggested by Hoover [34] and later corroborated by Polson *et al.* [38]. The key contributions to the free energy have been calculated from simulations in the expanded ensemble along a path that connects the solid with the EC. The N-dependence found in this investigation for the free energy of HS solids is strong and in full agreement with the

dependence that emerges from the simulation results obtained from numerical integration of the derivative of the free energy along the path reported by Polson *el al.* [38]. As might have been anticipated, different techniques yield consistent answers. On the other hand, our results are at variance with those reported by Chang and Sandler [63], who find a rather weak (linear) dependence of f_{ex} with $1/N$; the origin of this discrepancy is seemingly due to a missing term in their expressions of the free energy and not to an effect of the shape of the simulation box, as they originally claim.

A systematic study of the effect of the box shape on the free energy of the solid phase has also been considered in this chapter. Our results point to the conclusion that the free energy does not appear to be very sensitive to the precise shape of the simulation box; previous studies had suggested otherwise [37]. More importantly, we have found a systematic dependence of the computed values of the free energy with the arrangement of the closed-packed layers of the solid phase with respect to the simulation box. As far as we know, this effect has passed inadverted in previous calculations of the free energy of crystalline solids. A careful comparison of the free energies for structures with tilted and non-tilted closed-packed layers shows that the former are characterized by larger values of the free energy. This is probably due to the additional stress generated on a system that has to accomodate a crystalline structure into a box of fixed shape so as to be compatible with the restrictions imposed by the periodic boundary conditions. This stress is expected to be larger for tilted structures and more significant for small systems. We indeed find that the difference between the free energy of tilted and non-tilted structures gets smaller with increasing system size and vanishes, within statistical uncertainties, in the thermodynamic limit.

Chapter 4

HGO model: small molecular anisotropies

A computer simulation study of the phase diagram of non-spherical hard Gaussian overlap (HGO) molecules is presented in this chapter. We focus here on the phase behaviour for low values of κ, where κ represents the molecular anisotropy. It is shown that for small values of κ, systems of HGO molecules may exhibit isotropic (I), plastic solid (PS), and solid (S) phases depending on the value of κ. Though the fluid phase of the HGO model has been extensively studied [14–16, 73], no investigation has so far been reported for the crystalline phases. In addition to the fluid phase, we include here a study of the plastic solid and solid phases using different simulation techniques, such as thermodynamic integration, parametric integration, expanded ensemble, and Gibbs-Duhem integration.

From the equation of state at selected values of κ, the different phase transitions are determined from free energy calculations. For the computation of the free energy of the fluid phase we use either the ideal gas as the reference state or parametric integration, with κ being the integration parameter. In the latter case, a hard-sphere (HS) fluid at the same pressure is chosen as the reference state. The free energy of the plastic solid phase is computed from parametric integration choosing a HS crystal at the same pressure as the reference state. For the calculation of the free energy of the solid phase we use a non-interacting Einstein crystal (EC) with fixed center of mass as the reference state.

Knowing the transition properties at chosen values of κ, the transition lines in the P–κ plane are determined from integration of the Clausius-Clapeyron equation. We give an estimation of the location of the isotropic-plastic-solid triple point. Our results are compared with the phase behaviour

of similar hard-core models, namely, systems of hard ellipsoids, hard dumbbells, and hard spherocylinders.

4.1 Introduction

The HS model has proved to be useful to understand the physical behaviour of many simple systems [74]. However, other factors, such as molecular shape or size, must be taken into consideration to account for the formation of more complex phases. As for simple fluids, the structural behaviour of complex fluids is expected to be largely dominated by short-range repulsive interactions. This expectation motivates the attention paid to hard-core models, where the attractive interactions are neglected. Molecular models such as hard-dumbbells (HD) [75–77], hard spherocylinders (HSC) [12, 70, 78–80] or hard ellipsoids (HE) [1, 11, 81–83] have been widely used. In spite of the simple (geometric) way in which the repulsive interactions are incoroprated in these models, the corresponding mathematical form of the interactions is far from simple. This generally makes difficult their theoretical treatment. It is for this reason that Berne and Pechukas [84] introduced the Gaussian overlap model in 1972 as a simple model potential to represent the repulsive part of the intermolecular interactions. A hard version, known as the hard Gaussian overlap (HGO) model, was later introduced by Bhethanabotla and Steele [85]. For moderately non-spherical molecules, the viral coefficients B_2 to B_5 of the HGO and HE models have been reported to be very similar. As a consequence, one might expect that both models exhibit similar phase behaviour. This is interesting if one considers that the HGO model is computationally much simpler than its HE counterpart. Nevertheless, the differences between both models are expected to become noticeable for larger molecular elongations.

The isotropic fluid phase of the HGO model for different molecular elongations has been studied quite extensively. Rigby [15] has performed a study of the fluid phase for a range of molecular elongations $0.10 < \kappa < 10$ based on the calculation of the virial coefficients B_2 to B_5. The resulting viral equations of state compare satisfactorily with theoretical predictions of the equations of state of Boublik, Naumann-Chen-Leland and Wojcik-Gubbins [15]. In addition, the isotropic fluid phase of HGO systems with $0.5 \leq \kappa \leq 2$ has been studied from MC simulation. Maeso and Solana [14] has proposed an equation of state of the HGO isotropic fluid based on a generalization of the Carnahan-Starling equation of state. The results for different values of κ are in good agreement with simulation data of Rigby.

In the range of molecular elongations considered here, we observe the presence of three phases: isotropic fluid, plastic solid, and solid phases. The same sequence of phases has been reported in related hard-core models. According to the simulation study of Frenkel *et al.* [11, 81] for the HE model, the PS phase is stable for molecular elongations $\kappa \leq 1.25$. This is in quantitative agreement with theoretical predictions from Singh and Singh [87, 88]. Also, the PS–S transition is reported to be continuous as no discontinuity of the orientational order parameter appears to accompany the transition. As for the HSC model, Bolhuis and Frenkel [70] have carried out a thorough study of the phase behaviour from computer simulation. They find that the isotropic fluid freezes into the PS phase for molecular elongations $\kappa \leq 1.35$. Vega *et al.* [75, 76], and Singer and Mumaugh [77] have studied the stability of the PS phase in the HD model. They conclude that the PS phase lies in the range $1 \leq \kappa \leq 1.4$.

We determine the phase diagram of the HGO model by computing the I–PS, PS–S, and I–S coexistence lines by Gibbs-Duhem integration in the range $1 \leq \kappa \leq 2$. The melting point of the HS system is taken as the starting point for the integration along the I–PS coexistence line. The I–S transition point for $\kappa = 2$, and the PS–S transition point for $\kappa = 1.25$ have been taken as starting points for the determination of the I–S and PS–S coexistence lines, respectively. We give an estimation of the location of the I–PS–S triple point.

4.2 Model potential

The HGO model is intimately related with the so-called Gaussian overlap model proposed by Berne and Pechukas [84] in 1972. The Gaussian overlap model aims to provide a realistic description of the anisotropic repulsive part of the interactions between elongated molecules. Each molecule is considered to have a quasi ellipsoidal shape, with an associated three-dimensional Gaussian given by

$$G(\mathbf{r}) = \exp(-\mathbf{r}^t \mathbf{S}^{-1} \mathbf{r}) \,, \tag{4.1}$$

where

$$\mathbf{S} = (L^2 - D^2)\hat{\mathbf{u}}\hat{\mathbf{u}}^t + D^2\mathbf{I} \,, \tag{4.2}$$

is the range matrix, $\mathbf{r}$ is the center of mass of the molecule, $\hat{\mathbf{u}}$ is the axial unit vector, L and D are a measure of the dispersion of the Gaussian distribution in the direction parallel and perpendicular to the symmetry axis, respectively, and $\mathbf{I}$ is the unit matrix. G can be viewed as a representation of the molecular distribution of matter. Berne and Pechukas assume that

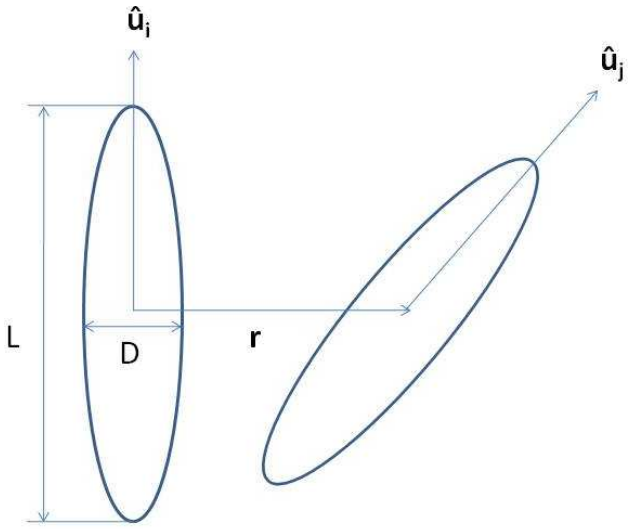

Figure 4.1: Schematic representation of the HGO model.

the repulsive interaction between a pair of such molecules is proportional to the overlap of their Gaussians. Under this assumption, they show that the repulsive interactions decay exponentially with distance, the characteristic decay length being explicitly given by

$$\sigma(\hat{\mathbf{r}}, \hat{\mathbf{u}}_i, \hat{\mathbf{u}}_j) = D \left\{ 1 - \frac{\chi}{2} \left[\frac{(\hat{\mathbf{r}} \cdot \hat{\mathbf{u}}_i + \hat{\mathbf{r}} \cdot \hat{\mathbf{u}}_j)^2}{1 + \chi(\hat{\mathbf{u}}_i \cdot \hat{\mathbf{u}}_j)} + \frac{(\hat{\mathbf{r}} \cdot \hat{\mathbf{u}}_i - \hat{\mathbf{r}} \cdot \hat{\mathbf{u}}_j)^2}{1 - \chi(\hat{\mathbf{u}}_i \cdot \hat{\mathbf{u}}_j)} \right] \right\}^{-1/2} , \quad (4.3)$$

where the parameter χ is defined as $\chi = (\kappa^2 - 1) / (\kappa^2 + 1)$, with $\kappa = L/D$ being a measure of the anisotropy of the Gaussian distribution. For spherical molecules, characterized by a spherically symmetric distribution of matter, $\kappa = 1$ and $\chi = 0$. On the other hand, infinitely anisotropic molecules will be characterized by $\chi = 1$.

In an attempt to consider a realistic expression for the anisotropic repulsive and attractive interactions between non-spherical molecules, Berne and Pechukas considered a Lennard-Jones functional form for the distance dependence of the interactions, with σ (a constant for spherically symmetric molecules) given by Eq. (4.3). This is what nowdays is known as the Gaussian overlap model. It soon became clear that this model contains a number of unrealistic features, the most troublesome being that it grossly overestimates the strength of the anisotropic attractive interactions at long distances. A succesful attempt to alleviate these inconsistencies was made by Gay and Berne [86], who proposed what nowdays is probably the most sucessful single-atom potential for non-spherical molecules.

At a later stage, Bhethanabotla and Steele [85] considered a hard version of the Gaussian overlap model. They simply ignore the attractive interactions and consider σ as defined in Eq. (4.3) as the distance of closest approach between a pair of non-spherical molecules. The model so defined is known as the hard Gaussian overlap (HGO) model. The interaction between a pair of molecules is explicitly defined as

$$u(\mathbf{r}, \hat{\mathbf{u}}_i, \hat{\mathbf{u}}_j) = \begin{cases} \infty & \text{if } r \leq \sigma(\hat{\mathbf{r}}, \hat{\mathbf{u}}_i, \hat{\mathbf{u}}_j)\,, \\ 0 & \text{if } r > \sigma(\hat{\mathbf{r}}, \hat{\mathbf{u}}_i, \hat{\mathbf{u}}_j)\,. \end{cases}$$

A schematic representation of the HGO model is shown in Fig 4.1. It is important to note that this model does not have a proper geometric representation: molecules interacting through HGO interactions cannot be represented by a solid body. Rather, it is a (simple) mathematical representation of the short-range repulsive interactions. Though the model does not make any assumption about the molecular geometry, the HGO molecules are usually said to have a quasi-ellipsoidal shape. This is justified by the fact that for parallel HGO molecules, σ is *exactly* the contact distance between a pair of (parallel) ellipsoids of elongation $\kappa = L/D$. For non-parallel HGO molecules, σ does not represent the distance of closest approach between ellipsoidal molecules and, therefore, a single HGO molecule should not be viewed as an ellipsoid. Incidentally, one should note that if $\kappa = 1$ the HGO model represents the interactions between hard spheres of diameter D.

As already mentioned, the HGO and HE models share similarities but are not equivalent. The main differences are believed to be due to the larger value of the excluded volume between a pair of HGO molecules in comparison with that of HE molecules [16]. While the geometry of the HE model is well defined, it is not straightforward to define the volume of a single HGO molecule. We use the idea of Rigby [15] and associate a volume to the HGO molecule equal to the volume of a HE molecule with the same anisotropy

$$v_0 = \frac{\pi}{6}\kappa D^3\,,$$

This is justified by the fact that the distance of closest approach between an HGO molecule of elongation κ and a spherical molecule describes an ellipsoidal surface, enclosing a volume v_0 as given above, when the diameter of the sphere is made infinitely small [15].

4.3 Simulation details

4.3.1 Generalities

Our goal in this chapter is to trace the phase boundaries of the HGO model in the low-κ region ($1 \leq \kappa \leq 2$). As it will be shown in the following, the phase diagram in this range of molecular elongations consists on regions of stability of isotropic fluid, plastic solid, and solid phases. The corresponding coexistence lines are determined by Gibbs-Duhem integration using as starting points the corresponding coexistence values at suitable values of κ. For this end, we have performed a full analysis of the equations of state of HGO models with molecular elongations $\kappa = 1$ (hard spheres), 1.25, and 2. We will show that the HGO model with $\kappa = 1.25$ exhibits a S phase in addition to the I and PS phases, and the PS phase is absent for $\kappa = 2$.

The equations of state are determined from NPT computer simulation series. A first series involves compressing a low-density fluid configuration to obtain the fluid branch. $N = 500$ molecules in the fluid phase are considered. A second series is started at high density from a crystalline solid structure consisting on a set of layers parallel to the xy plane with in-layer hexagonal arrangement of the centers of mass of the molecules. The layers are stacked along the z direction according to an ABC pattern. We have considered 6 layers each one consisting on 10×10 molecules, which yields a total of $N = 600$ molecules.

The simulations are divided in cycles, each cycle consisting on N trial translational and rotational molecular displacements and one atempt to change the volume. Volume fluctuations are performed using different schemes depending on each phase. For translationally disordered phases (I), we use the LVOL1 scheme while for phases characterized by three-dimensional positional order (PS or S) we use the LVOL3 scheme (see chapter 2). We adjust the maximum translational/rotational displacements and box-length fluctuation so as to obtain an average acceptance of about $30 - 35\%$ and 25% of the attempted moves, respectively. Averages of properties of interest such as the number density, and order parameters are taken over blocks of 5000 cycles.

All quantities are reported in reduced (dimensionless) units, using D as the unit of length, and $k_{\mathrm{B}}T$ as the energy scale. Explicitly, we define the reduced pressure $P^* = \beta P D^3$, where $\beta = (k_{\mathrm{B}}T)^{-1}$, and the reduced number density $\rho^* = \rho D^3$. The reduced Helmholtz free energy is defined as $f = F/(Nk_{\mathrm{B}}T)$, and the Gibbs free energy as $g = G/(Nk_{\mathrm{B}}T)$.

4.3.2 Order parameters

To distinguish between different phases we calculate the orientational, and bond-orientational order parameters during the simulations. The orientational order parameter S is defined as the average value of the largest eigenvalue of the ordering tensor $Q_{\alpha\beta}$ [89] defined as

$$Q_{\alpha\beta} = \frac{1}{N}\sum_{i=1}^{N}\frac{1}{2}\left(3u_{i\alpha}u_{i\beta} - \delta_{\alpha\beta}\right) , \tag{4.4}$$

where $u_{i\alpha}$ is the α-component ($\alpha = x, y, z$) of the axial vector $\hat{\mathbf{u}}_i$. The order parameter S measures the degree of orientational order. It can take values between 0 (in an orientationally disordered phase) and 1 (in a perfectly orientationally ordered phase).

The local bond orientational order [90] describes the translational in-plane order and is defined as:

$$\Psi_6(\mathbf{r}_i) = \frac{\sum_j w(R_{ij})\exp(i6\theta_{ij})}{\sum_j w(R_{ij})} ,$$

where j is the number of nearest neighbours of molecule i and θ_{ij} is the angle between the projection (R_{ij}) of the intermolecular vector $\mathbf{r}_{ij}$ onto the layer plane and a fixed axis. $w(R_{ij})$ is a weight function that provides a criterium to choose the nearest neighbours of each molecule. Following Bates and Luckhurst [91] we choose this function as 1 for $R_{ij} < 1.4D$, 0 for $R_{ij} > 1.8D$, and in between is defined as a linear interpolation. According to its definition, $\Psi_6(\mathbf{r}_i)$ is a complex quantity. For practical purposes, we determine the bond orientational order in each layer as

$$\Psi_6^l = \mathrm{Re}\left\{\frac{1}{N_l}\sum_i \Psi_6(\mathbf{r}_i)\right\} , \tag{4.5}$$

where the sum is restricted to those molecules that belong to layer l, and N_l is the number of molecules in layer l. A bulk bond orientational order parameter Ψ_6 is also computed by averaging $\Psi_6(\mathbf{r}_i)$ over the whole system

$$\Psi_6 = \mathrm{Re}\left\{\frac{1}{N}\sum_i \Psi_6(\mathbf{r}_i)\right\} . \tag{4.6}$$

The bond orientational order measures the extent to which molecules in the system keep a local hexagonal arrangement. Both Ψ_6^l and Ψ_6 can vary between 0 (no hexagonal order) and 1 (perfect hexagonal order). They are therefore expected to be close to 1 for the S and PS phases, and close to 0 for the I phase.

4.3.3 Simulation averages and error estimation

Properties such as the density, order parameters, or the enthalpy, can be directly calculated during the simulations. It was shown in §2.2.4 how to proceed to the calculation of the ensemble averages of such properties. We recall here that the uncertainty ε associated with these properties is estimated from $\varepsilon = 2\sigma_{\rm run}$, where $\sigma_{\rm run}$ is the standard deviation of the run averages computed from $\sigma_{\rm run} = \sigma_{\rm b}/(N_{\rm b}-1)^{1/2}$, with $\sigma_{\rm b}$ being the standard deviation of the block averages, and $N_{\rm b}$ the number of blocks.

One of the goals of this work is to determine the phase diagram of molecular models, which typically requires a computation of free energies. This is not a property that can be directly calculated in a simulation. The most commonly used method for the calculation of the free energy is thermodynamic integration, which requires a knowledge of the free energy of a reference state point and fitting of the simulation data for the compressibility factor to a chosen functional form

$$g(P) = g_{\rm ref} + \int_{P_{\rm ref}}^{P} Z(P')\frac{dP'}{P'}\,. \tag{4.7}$$

According to this equation, there are two error sources that will contribute to the statistical uncertainty ε_g in the free energy (at any given pressure): the computation of $g_{\rm ref}$ and the numerical integration along the equation of state, with associated errors $\varepsilon_{\rm ref}$ and $\varepsilon_{\rm int}$, respectively. The uncertainty associated with the free energy is then estimated as $\varepsilon_g = (\varepsilon_{\rm ref}^2 + \varepsilon_{\rm int}^2)^{1/2}$. The computation of $g_{\rm ref}$ is either analytical, in which case $\varepsilon_{\rm ref} = 0$ and the only contribution to ε_g is $\varepsilon_{\rm int}$, or is calculated from a numerical quadrature along a path that connects the reference state with a state of known free energy

$$g_{\rm ref} = g_0 + \int_{\xi_0}^{\xi_1} d\xi\, \frac{\partial g(\xi)}{\partial \xi}\,,$$

where $g_0 \equiv g(\xi_0)$ and $g_{\rm ref} \equiv g(\xi_1)$. The above integration is performed after a computation of the integrand in a simulation series for values of ξ in the domain $\xi_0 \leq \xi \leq \xi_1$. $\varepsilon_{\rm ref}$ follows in this case from propagation of errors associated with the values of the integrand.

Though an estimate of $\varepsilon_{\rm ref}$ is straightforward, obtaining an estimate of $\varepsilon_{\rm int}$ is not simple. Recently, de Miguel [33] has proposed a procedure to estimate the statistical uncertainties associated with free energies obtained from thermodynamic integration when using fitted data. The method is based on a synthetic analysis of the simulation data and will be illustrated here for estimating the uncertainty associated with the Gibbs free energy at an arbitrary

pressure P. Let us consider that a sequence of n simulations are performed at input pressures P_i $(i = 1, \ldots, n)$. We denote by $Z_i^{(0)}$ the corresponding output values of the compressibility factor, and by ε_i their associated statistical errors. In practice, the set $Z_i^{(0)}$ is fitted to a polynomial of order M in P. The fitting coefficients are denoted as $\{a_m^{(0)}\}$ $(m = 0, 1, \ldots, M)$. The free energy at pressure P will parametrically depend on this set, $g^{(0)}(P) \equiv g(a_m^{(0)}; P)$. One next assumes that the possible outcomes of Z from a simulation at P_i obey a Gaussian distribution with mean value $Z_i^{(0)}$ and standard deviation ε_i. The synthetic algorithm involves the following steps:

1. Generate synthetic sets of n data points, $Z_i^{(k)} = Z_i^{(0)} + \xi_i$, where ξ_i is a random number drawn from a Gaussian distribution with zero mean value and standard deviation σ_i, with $\varepsilon_i = 2\sigma_i$. Each set is considered as a potential replica of the actual simulation data set.

2. Find the fitting coefficients $a_m^{(k)}$ and the free energy $g^{(k)}(P) \equiv g(\{a_m^{(k)}\}; P)$ corresponding to each synthetic data set. The set of free energies $g \equiv g^{(k)}(P)$ is expected to be Gaussian distributed about the mean value $g^{(0)}$,

$$\mathcal{P}(\delta g) = \frac{1}{\sigma\sqrt{2\pi}} \exp\left(-\frac{\delta g^2}{2\sigma^2}\right),$$

   where we have used the notation $\delta g = g - g^{(0)}$.

3. Determine the standard deviation σ of this Gaussian distribution, and relate σ with ε_{int}. In practice, we consider $\varepsilon_{\text{int}} = 2\sigma$.

The synthetic analysis will prove useful for estimating the statistical uncertainty of the Gibbs free energy at a first-order transition. As it will be shown later, this is required in order to assess the statistical uncertainty of the corresponding transition pressure.

4.4 HGO model $\kappa = 1$ (hard spheres)

We present in Fig. 4.2 the equation of state of a system of hard spheres showing the isotropic fluid (I) and solid (S) phases. The location of the I–S transition is also indicated in the plot. An initial isotropic configuration is equilibrated at low pressure for 4×10^5 cycles and averages are taken over 4×10^5 additional cycles. The fluid branch is run from low pressure $P^* = 0.2$ up to high pressure $P^* = 15$. Constant pressure simulations are carried out

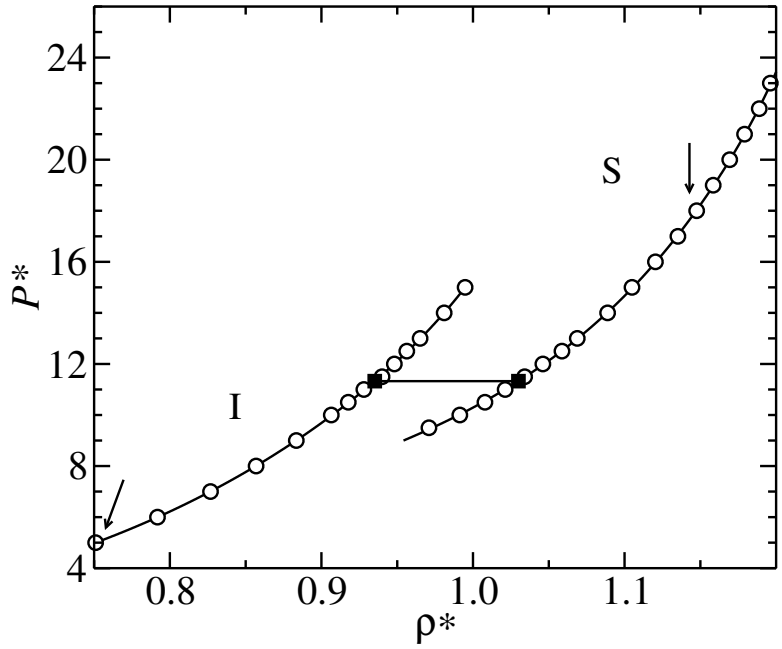

Figure 4.2: Pressure P^* vs density ρ^* for a HS system in the isotropic fluid (I) and solid (S) regions. Continuous lines are fits to the simulation data. Filled squares indicate the I–S transition. Arrows indicate the reference states considered for the calculation of the free energy of each phase. Pressure is expressed in units of $P^* = \beta P D^3$ and the density $\rho^* = \rho D^3$, where D is the diameter of the spheres. Error bars in the density are smaller than the size of the symbols.

for a total of 25 state points. No crystallization of the fluid phase in this simulation series is observed. The simulations in the solid phase are started from a lattice configuration and a total of 19 constant-pressure simulations are run in the range $9.5 \leq P^* \leq 24$. Below $P^* = 9.5$, the crystal melts into a fluid phase.

During the simulation runs, we follow the behaviour of the bond orientational order parameter. The isotropic phase is characterized by the lack of positional order ($\Psi_6 \approx 0$), while the solid phase is characterized by a high degree of order. Ψ_6 is seen to slowly decrease as the solid is expanded and to exhibit a discontinuous jump to zero at the melting transition.

4.4.1 Free energy calculations

The determination of the fluid-solid transition involves a computation of the free energy (or chemical potential) of each phase; as argued earlier in chapter 2, the most commonly used method is thermodynamic integration. For the

Table 4.1: Thermodynamic properties of a HS system at $\rho^* = 0.925$ (close to the freezing transition) obtained from fitting $Z(\rho^*)$ to a polynomial of order $M-1$ in ρ^*. We also include the values of χ^2 from the fit. P^* represents the pressure, g and f are the Gibbs and Helmholtz free energy, respectively. The last row includes the values obtained from the Carnahan-Starling (CS) equation of state.

M	χ^2	P^*	g	f
5	31998.8	10.9122	15.3213	3.5243
6	423.4	10.8669	15.3362	3.5882
7	151.7	10.8359	15.2836	3.5691
8	132.8	10.8268	15.2785	3.5738
9	120.9	10.8213	15.2704	3.5716
CS		10.8287	15.2678	3.5611

fluid phase of hard spheres we make use of Eq. (2.32)

$$f(\rho^*) = \ln \rho^* - 1 + \int_0^{\rho^*} [Z(\rho^{*\prime}) - 1] \frac{d\rho^{*\prime}}{\rho^{*\prime}} \,. \tag{4.8}$$

The integration in the above equation is performed by fitting the simulation data for the compressibility factor to a polynomial in the density of the form

$$Z(\rho^*) = \sum_{n=1}^{M} a_n (\rho^*)^{n-1} \,,$$

where the coefficients $a_1 = 1$, $a_2 \equiv B_2 = 2\pi/3$, and $a_3 \equiv B_3 = 5\pi^2/8$ are fixed. B_2 and B_3 are the second and third-order virial coefficients for the HS fluid [74]. The values of the free energy are expected to depend on the degree of the fitting polynomial. This is illustrated in Table 4.1, where we include the values of the free energy at $\rho^* = 0.925$ when $M = 6, 7, 8$ and 9 coefficients are considered in the calculations. From this table we infer a relatively strong dependence of the free energy with M. In addition, it seems that M needs to be fairly large. As a consequence, we wonder whether a different type of fitting would be more efficient. We have tried a polynomial fitting of the compressibility factor of the form

$$Z(P^*) = \sum_{n=1}^{M} a_n (P^*)^{n-1} \,. \tag{4.9}$$

Table 4.2: Thermodynamic properties of a HS system at the fluid pressure $P^* = 11.25$ (close to the freezing transition) obtained from fitting $Z(P^*)$ in the range $P^* \geq 5$. We also include the values of χ^2 from the fit. g and f represent the Gibbs and Helmholtz free energy, respectively.

M	χ^2	ρ^*	g	f
3	9.32	0.93295	15.7271	3.6685
4	3.79	0.93365	15.7321	3.6826
5	3.77	0.93363	15.7321	3.6824
6	3.71	0.93370	15.7320	3.6831

According to Eq. (2.33), the Gibbs free energy at an arbitrary pressure P^* follows from

$$g(P^*) = g_{\rm ref} + \int_{P^*_{\rm ref}}^{P^*} Z(P^{*\prime}) \frac{dP^{*\prime}}{P^{*\prime}} \,. \tag{4.10}$$

In this case, the integration is not carried out from low pressure, but from a reference pressure. We consider here $P^*_{\rm ref} = 5$. The free energy at this reference pressure is calculated using the particle-insertion (Widom) method at constant pressure [17]. Four independent constant-presure runs at $P^*_{\rm ref} = 5$ are carried out, each consisting on 10×10^6 cycles with 2500 trial insertions per cycle. After averaging, we obtain $\rho^*_{\rm ref} = 0.7503(2)$ and $g_{\rm ref} = 8.390(7)$. This value is fully consistent with the value of $g = 8.384$ obtained from the Carnahan-Starling (CS) semi-empirical equation of state,

$$Z_{\rm CS} = \frac{1 + \eta + \eta^2 - \eta^3}{(1-\eta)^3} \,, \qquad f_{\rm CS} = \ln \rho^* - 1 + \frac{\eta(4-3\eta)}{(1-\eta^2)} \,,$$

where $\eta = \pi\rho^*/6$ is the packing fraction.

We include in Table 4.2 a number of thermodynamic properties of the HS system close to the freezing transition. A comparison of the data in Tables 4.1 and 4.2 shows that the systematic errors due to the particular form of the fitting model are substantially smaller when the fit is performed over a narrower range of data. This conclusion follows from the fact that the χ^2 values of the fit are significantly smaller in Table 4.2 than those in Table 4.1. Also, less coefficients are required to represent the simulation data.

The values of the fitting coefficients for the fluid and solid phase of the HS system are given in Table 4.3. The Gibbs free energy of the solid phase is computed from standard thermodynamic integration along the solid equation

Table 4.3: Fitting coefficients for the fluid and solid phases for a system of hard spheres. A polynomial fit of the form given in Eq. (4.9) is considered. Also included are the χ^2 values resulting from the fits.

a_m	fluid	solid
a_1	1.55570	5.02840
a_2	1.12246	0.23340
a_3	−0.02326	0.04031
a_4	0.00057	−0.00151
a_5		0.00002
χ^2	3.79	6.30

of state [cf. Eq. (4.10)]. We use the EC method to calculate the Helmholtz free energy $f_{\rm ref}$ of a reference solid state. For this purpose we first determine the equilibrium lattice parameters of the solid in a constant-pressure simulation at $P^*_{\rm ref} = 18$. The average density of the solid structure is found to be $\rho^*_{\rm ref} = 1.1476(38)$. A path at constant density that connects the solid under study with a non-interacting EC with fixed center of mass is considered. The Helmholtz free energy of the solid reference state is then calculated as (see chapter 2)

$$f_{\rm ref} = f^{\rm CM}_{\rm EC} + \Delta f^{\rm CM}_{\chi} + \Delta f^{\rm CM}_{\lambda_t} + \Delta f^{\rm CM}\,.$$

The meaning of each term was explained in chapter 2. We recall that in the above expression $f^{\rm CM}_{\rm EC}$, and $\Delta f^{\rm CM}$ are analitical. $\Delta f^{\rm CM}_{\lambda_t}$ is calculated from

$$\Delta f^{\rm CM}_{\lambda_t} = -\frac{1}{N{\rm k_B}T}\int_0^{\lambda_t}\left\langle \sum_{i=1}^{N}(\mathbf{r}_i - \mathbf{r}_i^0)^2/D^2 \right\rangle_{\chi=1} d\lambda_t'\,. \tag{4.11}$$

λ_t is the harmonic coupling for which the solid under study approach the EC. The integrand in the above expression must be a slowly varying function of λ_t'; however, one might expect a rapid grow of the mean-square displacement as $\lambda_t' \to 0$. To avoid this divergence, it is usual to consider a change of variables of the type

$$u = \ln(\lambda_t^* + c)\,, \tag{4.12}$$

where $\lambda_t^* = \beta\lambda_t'$ and c is a constant. With this change, Eq. (4.11) can be expressed as

$$\Delta f^{\rm CM}_{\lambda_t} = -\frac{1}{N}\int_{u_{\rm min}}^{u_{\rm max}} du\,(\lambda_t^* + c)\left\langle \sum_{i=1}^{N}(\mathbf{r}_i - \mathbf{r}_i^0)^2/D^2 \right\rangle_{\chi=1}\,, \tag{4.13}$$

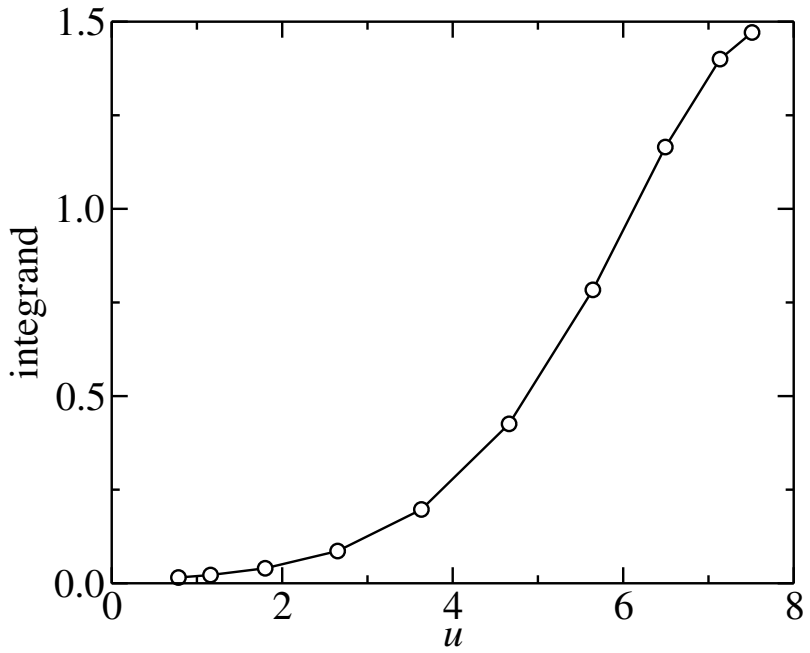

Figure 4.3: Variation of the integrand in Eq. (4.13). The line is a guide to the eye. The error bars are smaller than the size of the symbols.

where $u_{\min} = \ln c$, and $u_{\max} = \ln(\beta\lambda_t + c)$. With an appropiate choice of the constant c, the integrand can be smoothed out. A value of $c = 2$ turns out to be a good choice for the present application. The integration is numerically calculated by a 10-point Gaussian quadrature. This involves performing NVT simulations at intermediate values of the coupling parameter to determine the average mean-square displacement. The variation of the integrand in the Eq. (4.13) is shown in Fig. 4.3.

The contribution $\Delta f_\chi^{\rm CM}$ is computed in a simulation in the expanded ensemble. In Table 4.4 we give the relevant contributions to the free energy of the crystalline solid phase. Once $f_{\rm ref}$ has been calculated, the Gibbs free energy at the reference pressure follows from

$$g_{\rm ref} = f_{\rm ref} + \frac{P^*_{\rm ref}}{\rho^*_{\rm ref}} \,. \tag{4.14}$$

The Gibbs free energy at any pressure in the solid phase is obtained from Eq. (4.10). The equation of state of the solid phase is fitted to a polynomial in P^*. We find that 5 terms are enough to reproduce the equation of state. The fitting coefficients are given in Table 4.3.

Table 4.4: Relevant contributions to the free energy of the fcc structure of a HS solid at a pressure of $P^*_{\rm ref} = 18$ (average density $\rho^*_{\rm ref} = 1.1476(38)$). $f^{\rm CM}_{\rm EC}$ is the free energy of the EC, $\Delta f^{\rm CM}_{\chi}$ is the free energy difference between the interacting and non-interacting EC with harmonic coupling $\lambda_t = 2000\, k_{\rm B}T$, and $\Delta f^{\rm CM}_{\lambda_t}$ is the free energy difference between the HS solid and the interacting EC. $\Delta f^{\rm CM}$ is the contribution due to the constraint on the center of mass. $f_{\rm ref}$ and $g_{\rm ref}$ are the absolute Helmholtz and Gibbs free energies of the reference solid state, respectively.

$f^{\rm CM}_{\rm EC}$	$\Delta f^{\rm CM}_{\chi}$	$\Delta f^{\rm CM}_{\lambda_t}$	$\Delta f^{\rm CM}$	$f_{\rm ref}$	$g_{\rm ref}$
9.66812	0.00346(4)	−3.4335(8)	−0.015763	6.2223(8)	21.9072(8)

Table 4.5: Coexistence properties of the I–S transition for a HS system as obtained from different simulation methods. NPT MC corresponds to results obtained in this work. EC (Einstein crystal) and EM (Einstein molecule) are results from Vega *et al.* [39]. SMC are data from Errington [92] using the switch Monte Carlo method.

method	$\rho^*_{\rm I}$	$\rho^*_{\rm S}$	P^*	g
NPT MC	0.935(3)	1.030(4)	11.33(14)	15.814(14)
EC			11.34	
EM			11.35(3)	
SMC	0.9347(4)	1.0326(6)	11.34(1)	

4.4.2 Location of the fluid-solid transition

In order to determine the location of the first-order transition between the fluid (I) and solid (S) phases, the coexistence condition $g_{\rm I}(P) = g_{\rm S}(P)$ is solved. In Table 4.5 we give the coexistence properties at the I–S transition. According to the data in Table 4.5, we find good agreement between our results and data from Vega and Noya [39], and from Errington [92] for a system of $N = 500$ hard spheres. Vega and Noya use the Einstein crystal method and the Einstein molecule method for the calculation of the free energy of the solid phase, while Errington makes use of the phase-switch Monte Carlo method.

Table 4.6: Fitting coefficients for the fluid, plastic solid, and solid phases for a system of HGO molecules with molecular elongation $\kappa = 1.25$. A polynomial fit for $Z(P^*)$ is used. Also included are the χ^2 values resulting from the fits.

a_m	fluid	plastic solid	solid
a_1	1.93729	2.77147	43.88456
a_2	1.26437	0.97884	−1.26358
a_3	−0.01866	−0.00105	0.04408
a_4	0.00048	5.19×10^{-6}	−0.00040
a_5	-4.56×10^{-6}	-9.17×10^{-9}	1.36×10^{-6}
χ^2	4.61	14.00	8.36

4.5 HGO model $\kappa = 1.25$

When the HGO molecules become non-spherical ($\kappa \neq 1$), one might expect the stabilization of an orientationally ordered solid phase at sufficiently high pressure, as is observed in a system of hard ellipsoids. This is illustrated in Fig. 4.4 where we present the equation of state of the HGO model with $\kappa = 1.25$ in the P^*–ρ^* plane showing isotropic fluid, plastic solid, and solid phases. The fluid branch is explored by compressing a low-pressure isotropic configuration. A total of 24 constant-pressure simulations are performed in the range $5 \leq P^* \leq 19$. Each state point is equilibrated over 5×10^5 cycles and averages are collected over 3×10^5 additional cycles. Constant-pressure simulations for a total of 32 state points are performed in the range $10 \leq P^* \leq 75$, starting from a lattice configuration with ABC structure. Averages are taken over a total of 4×10^5. The plastic solid phase is characterized by a high degree of translational order but a complete lack of orientational order. The solid phase is started from a lattice configuration with ABC stacking and a total of 14 state points are simulated along the solid branch expanding a high-pressure crystalline structure. Averages are computed over a total of 4×10^5 cycles.

4.5.1 Free energy calculations

The simulation data for the compressibility factor of all the phases are fitted to a polynomial function in P^*. The fitting coefficients corresponding to each phase are given in Table 4.6. From the analysis performed earlier for the HS system, we concluded that a fit of the form $Z(P^*)$ over a restricted range of pressures is numerically more stable. We use the same strategy for the isotropic phase of HGO systems. We consider $P^*_{\text{ref}} = 5$ as the reference

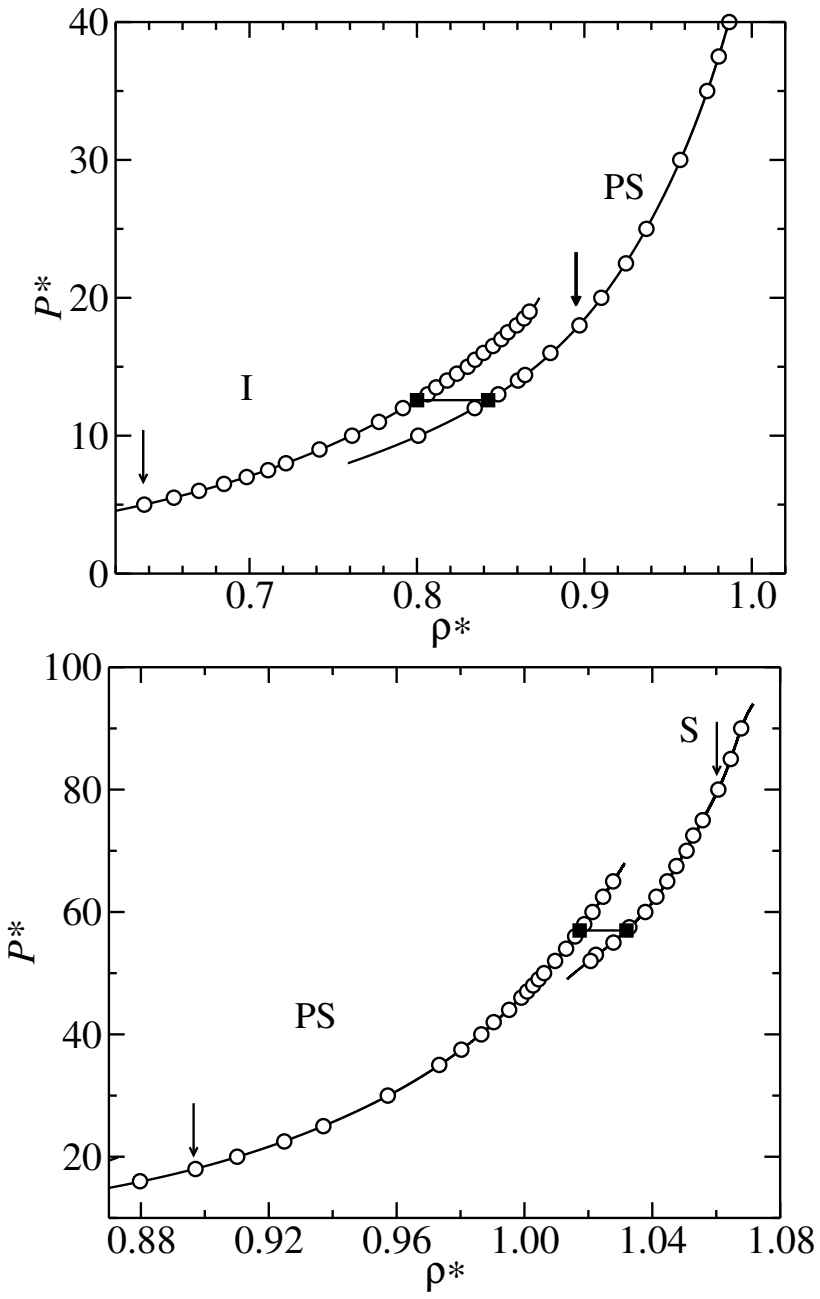

Figure 4.4: Pressure P^* vs density ρ^* for a system of HGO molecules with elongation $\kappa = 1.25$ in the isotropic (I), plastic solid (PS), and solid (S) regions. Continuous lines are fits to the NPT simulation data. Filled squares indicate the corresponding transitions. Arrows indicate the reference states considered for the calculation of the free energy of each phase. Pressure is expressed in units of $P^* = \beta P D^3$ and the density $\rho^* = \rho D^3$. Error bars are smaller that the size of the symbols.

pressure in the isotropic phase and calculate the free energy at this pressure by parametric integration. For an arbitrary parameter x, it follows that

$$g(x_1) = g(x_0) + \int_{x_0}^{x_1} dx \left(\frac{\partial g}{\partial x}\right) . \tag{4.15}$$

For this particular application, we consider $x = \ln\kappa$ and integrate from the HS fluid at the same pressure (the corresponding Gibbs free energy, $g_{\rm HS}(P^*_{\rm ref})$, was previously determined from the particle-insertion method). It then follows that

$$g(P^*_{\rm ref},\kappa) = g_{\rm HS}(P^*_{\rm ref}) + \int_1^{\kappa} \frac{d\kappa'}{\kappa'} \left(\frac{\partial g}{\partial \ln\kappa'}\right)_{P^*} . \tag{4.16}$$

As $\kappa = L/D$, the variation of the Gibbs free energy with molecular elongation can be calculated from changes in L (at constant D), from changes in D (at constant L), or from changes in both L and D. As $P^* = \beta P D^3$ is constant along the integration path, it seems natural to keep D constant. We therefore compute the first-order derivative in Eq. (4.16) from changes in L at constant D. The derivative of the Gibbs free energy can be separated into an ideal and excess contributions

$$\left(\frac{\partial g}{\partial \ln\kappa}\right)_{P^*} = \left(\frac{\partial g^{\rm id}}{\partial \ln\kappa}\right)_{P^*} + \left(\frac{\partial g^{\rm ex}}{\partial \ln\kappa}\right)_{P^*} .$$

As $g^{\rm id} = \ln P^*$, it follows that $\left(\partial g^{\rm id}/\partial\ln\kappa\right)_{P^*} = 0$. The variation of the excess part of the Gibbs free energy is defined as

$$\left(\frac{\partial g^{\rm ex}}{\partial \ln\kappa}\right)_{P^*} = \left(\frac{\partial g^{\rm ex}}{\partial \ln L}\right)_{P^*} = \Omega_L \,,$$

where Ω_L represents the change in (excess) Gibbs free energy when the molecular length L is changed at constant D, the process being performed at constant pressure P^*. As shown in chapter 2, Ω_L can be determinded using a perturbative approach [cf. Eq. (2.77)]. For the particular case of systems with hard interactions, the average of the Boltzmann factor of the perturbation is related with the probability $\mathcal{P}_L^{\rm acc}(\xi)$ of accepting a fictitious perturbation involving a change in the molecular size from $\ln L$ to $\ln L + \xi$ at constant D. Explicitly, one has

$$\Omega_L = -\lim_{\xi\to 0} \frac{1}{N\xi} \ln \mathcal{P}_L^{\rm acc}(\xi) \,. \tag{4.17}$$

$\mathcal{P}_L^{\rm acc}$ can be expressed in terms of the probability $\mathcal{P}_{ij}^{\rm ov}$ that a pair of molecules i and j overlap under the perturbation. Thus, the probability of accepting

the fictitious move can be written as

$$\mathcal{P}_L^{\rm acc} \approx 1 - \sum_{i>j} \mathcal{P}_{ij}^{\rm ov} \, . \tag{4.18}$$

$\mathcal{P}_{ij}^{\rm ov}$ can be expressed in terms of the ensemble average of the total number of overlaps $N_L^{\rm ov}$ due to the perturbation

$$\mathcal{P}_{ij}^{\rm ov} = \frac{\langle N_L^{\rm ov} \rangle}{\frac{1}{2}N(N-1)} \, .$$

Substitution into Eq. (4.18) yields

$$\mathcal{P}_L^{\rm acc} = 1 - \sum_{i>j} \frac{\langle N_L^{\rm ov} \rangle}{\frac{1}{2}N(N-1)} = 1 - \langle N_L^{\rm ov} \rangle \, . \tag{4.19}$$

Inserting the above expression into Eq. (4.17) and expanding the logarithm, one finally arrives to

$$\Omega_L = \lim_{\xi \to 0} \frac{\langle N_L^{\rm ov} \rangle}{N\xi} \, , \tag{4.20}$$

where second-order terms have been neglected.

In practice, the integration in Eq. (4.16) is performed using a 10-point Gaussian quadrature. For this purpose, NPT simulations are run for values of the molecular elongation in the range $1 \leq \kappa \leq 1.25$. A fictitious molecular scaling from $\ln L$ to $\ln L + \xi$ at constant D is performed every 5 cycles, and the number of overlaps $N_L^{\rm ov}$ counted. This value is accumulated during the production run and the average is used in Eq. (4.20). Five values of ξ are considered, and the final value of Ω_L is obtained from extrapolation to $\xi \to 0$. Each point is equilibrated for 4×10^6 cycles and averages are taken over 6×10^6 additional cycles. The variation of the integrand in Eq. (4.16) with the molecular elongation κ is shown in Fig 4.5. A value of 1.459(2) is found for the integral. Using in Eq. (4.16) the value of the Gibbs free energy $g_{\rm HS}$ of the HS fluid at $P_{\rm ref}^* = 5$, we obtain a value of $g_{\rm ref} = 9.849(7)$ for the Gibbs free energy of the reference isotropic state of the HGO model with $\kappa = 1.25$.

As a check of consistency, we have computed the Gibbs free energy of the HGO isotropic fluid with elongation $\kappa = 1.25$ at $P_{\rm ref}^* = 5$ from the particle-insertion method. A total of 10 independent runs of 10^6 cycles are carried out, with 2500 trial insertions per cycle (obtaining a probability of successful insertion of 3.3×10^{-5}). The resulting value, $g_{\rm ref} = 9.850(9)$, is fully consistent with the value previously obtained from parametric integration.

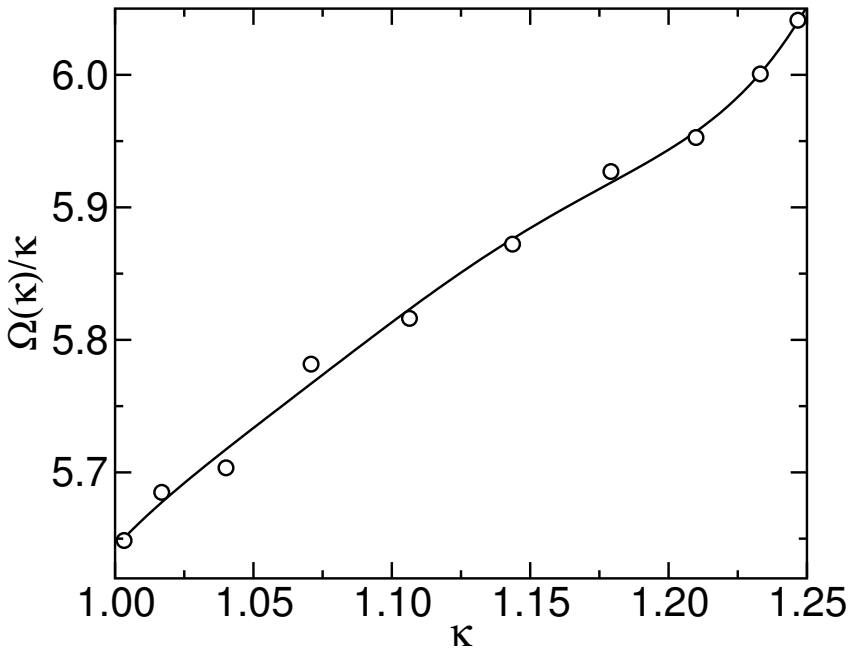

Figure 4.5: Behaviour of the integrand in Eq. (4.16) corresponding to the parametric integration performed in the isotropic fluid phase starting from the HS fluid at $P^*_{\rm ref} = 5$. The line is a guide to the eye. The error bars are smaller than the size of the symbols.

The computation of the Gibbs free energy of a reference state in the PS phase of the $\kappa = 1.25$ HGO model is also accomplished from parametric integration. We now consider $P^*_{\rm ref} = 18$ as the reference state and integrate from the HS solid at the same pressure. Both crystalline structures are assumed to have an ABC stacking (we recall that the free energy of the HS solid at this pressure was already computed in §4.4.1). The integration in Eq. (4.16) is calculated by using a 10-point Gaussian quadrature. The integrand is shown in Fig. 4.6. The resulting value of the integral is 4.5557(21). Using the value $g_{\rm HS}(P^*_{\rm ref}) = 21.9072(8)$ in Eq. (4.16) (see Table 4.4) we obtain a value of $g_{\rm ref} = 26.463(2)$ for the Gibbs free energy of the HGO plastic solid reference state.

The above calculation involves an integration along a path at constant P^*. As a check, the value of the Gibbs free energy has been independently assessed by considering a parametric integration but now along a path that links the HS crystal with the HGO plastic solid phase at constant $P^+ = 18$, where $P^+ = \beta P L D^2$. Rather than using D^3 as the unit of volume, the

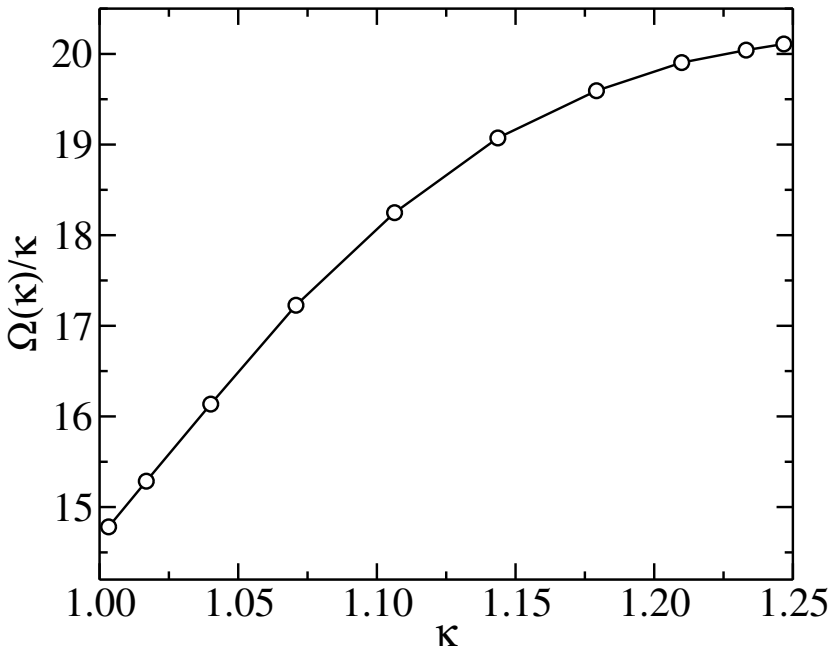

Figure 4.6: Behaviour of the integrand in Eq. (4.16) corresponding to the plastic solid phase starting from the HS solid at $P^* = 18$. The line is a guide to the eye. Error bars are smaller than the size of the symbols.

natural choice along this path is LD^2 (note that $P^+ = P^*\kappa$). In this case

$$g(P^+, \kappa) = g_{\rm HS}(P^+) + \int_1^\kappa \frac{d\kappa}{\kappa}\Omega^+ \,, \tag{4.21}$$

where we have defined

$$\Omega^+ = \left(\frac{\partial g}{\partial \ln k}\right)_{P^+} . \tag{4.22}$$

Note that Ω^+ corresponds to the change in free energy with respect to molecular elongation when κ is changed at constant pressure while keeping LD^2 constant. The ideal contribution is given by

$$\left(\frac{\partial g^{\rm id}}{\partial \ln \kappa}\right)_{P^+} = \left(\frac{\partial \ln P^*}{\partial \ln \kappa}\right)_{P^+} = \left(\frac{\partial \ln(P^+/\kappa)}{\partial \ln \kappa}\right)_{P^+} = -1 \,, \tag{4.23}$$

while the excess contribution is given by

$$\left(\frac{\partial g^{\rm ex}}{\partial \ln \kappa}\right)_{P^+} = \left(\frac{\partial g^{\rm ex}}{\partial \ln D}\right)_{P^+} \left(\frac{\partial \ln D}{\partial \ln \kappa}\right)_{P^+} + \left(\frac{\partial g^{\rm ex}}{\partial \ln L}\right)_{P^+} \left(\frac{\partial \ln L}{\partial \ln \kappa}\right)_{P^+} .$$

Defining

$$\Omega_L^+ = \left(\frac{\partial g^{\rm ex}}{\partial \ln L}\right)_{P^+} \qquad \Omega_D^+ = \left(\frac{\partial g^{\rm ex}}{\partial \ln D}\right)_{P^+} , \tag{4.24}$$

it follows that

$$\left(\frac{\partial g^{\rm ex}}{\partial \ln \kappa}\right)_{P^+} = -\frac{1}{3}\left(\Omega_D^+ - 2\Omega_L^+\right) . \tag{4.25}$$

From Eqs. (4.23) and (4.25) one finally arrives to

$$\Omega^+ = -1 - \frac{1}{3}\left(\Omega_D^+ - 2\Omega_L^+\right) . \tag{4.26}$$

After the integration in Eq. (4.21), we obtain

$$g(P^+ = 18, \kappa = 1.25) = 21.9072 + 0.4707 = 22.3779 .$$

In the usual reduced units, the pressure of this plastic solid state is $P^* = 14.4$ for $\kappa = 1.25$. The value of the Gibbs free energy at $P^*_{\rm ref} = 18$ follows from integration of the equation of state of the plastic phase in the appropriate range. Explicitly, one has

$$g_{\rm ref} \equiv g(P^*_{\rm ref} = 18) = g(P^* = 14.4) + \int_{14.4}^{18} Z(P^*)\frac{dP^*}{P^*} .$$

After the integration, we find $g_{\rm ref} = 26.461$, which is fully consistent with our previous calculation.

For the calculation of the free energy of a reference solid state we use the extension of the EC method to molecular crystals, proposed by Frenkel and Mulder [11]. As shown in §2.5.2, the free energy can be expressed as

$$f = f_{\rm EC}^{\rm CM} + \Delta f_\chi^{\rm CM} + \Delta f_\xi^{\rm CM} + \Delta f^{\rm CM} . \tag{4.27}$$

We choose a crystalline ABC structure at $P^*_{\rm ref} = 80$ as reference state. This structure is equilibrated in a constant-pressure simulation. We find an average density of $\rho^*_{\rm ref} = 1.06057$. Here, we consider an EC at the same density and structure, with $\xi \equiv \lambda_t = 2500\, k_{\rm B}T$ and $\lambda_r = 10\xi$. The difference in free energy between the interacting and non-interacting EC, $\Delta f_\chi^{\rm CM}$, is calculated in an expanded ensemble simulation. The contribution $\Delta f_\xi^{\rm CM}$ [see Eq. (2.67)] is numerically calculated from a 10-point Gaussian quadrature after considering a variable change of the same nature as the one considered previously for the HS solid. The variation of the integrand in $\Delta f_\xi^{\rm CM}$ with the integration variable is shown in Fig. 4.7. The different contributions to the free energy of the reference solid state are tabulated in Table 4.7. Finally, the Gibbs free energy of the reference solid state follows from Eq. (4.14).

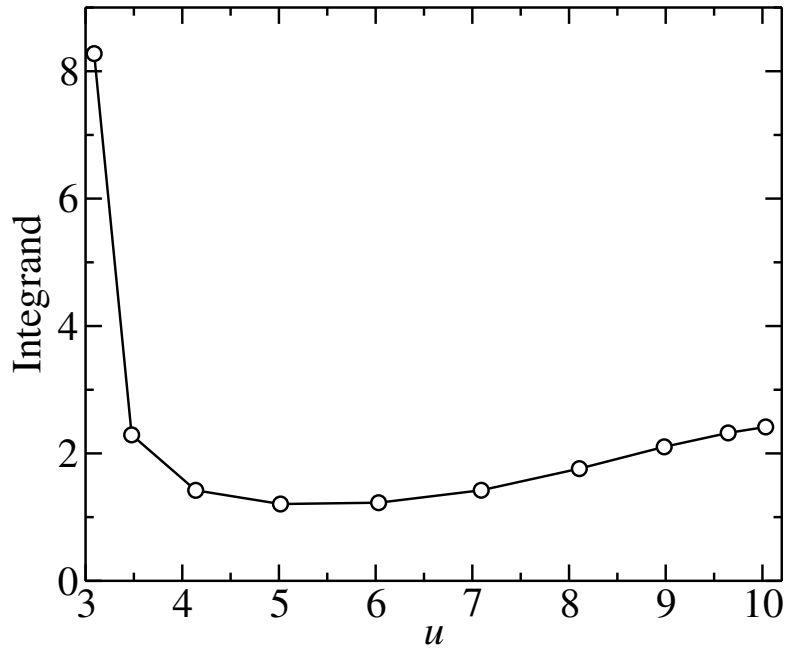

Figure 4.7: Variation of the integrand in the 10-point Gaussian quadrature for the computation of $\Delta f_{\xi}^{\mathrm{CM}}$ for the $\kappa = 1.25$ HGO solid at $P^* = 80$. $u = \ln c + \xi$ (with $c = 20$) is the integration variable. The line is a guide to the eye. The error bars are smaller than the size of the symbols.

Table 4.7: Relevant contributions to the free energy of the ABC crystalline phase of the $\kappa = 1.25$ HGO model at a pressure $P^*_{\mathrm{ref}} = 80$ ($\rho^*_{\mathrm{ref}} = 1.06057$). $f_{\mathrm{EC}}^{\mathrm{CM}}$ is the free energy of the Einstein crystal, $\Delta f_{\chi}^{\mathrm{CM}}$ is the free energy difference between the interacting and non-interacting Einstein crystal with harmonic coupling constants $\lambda_t = 2500 k_{\mathrm{B}}T$ and $\lambda_r = 25000 k_{\mathrm{B}}T$. $\Delta f_{\xi}^{\mathrm{CM}}$ is the free energy difference between the HGO solid and the interacting Einstein crystal. Δf^{CM} is the contribution due to the constraint on the center of mass. In the last two columns we give the Helmholtz and Gibbs free energy of the reference solid state, respectively.

$f_{\mathrm{EC}}^{\mathrm{CM}}$	$\Delta f_{\chi}^{\mathrm{CM}}$	$\Delta f_{\xi}^{\mathrm{CM}}$	Δf^{CM}	f_{ref}	g_{ref}
26.57276	0.0181(18)	-13.3952(79)	-0.015894	13.1797(79)	88.611

Table 4.8: Coexistence properties of the I–II transition, with I and II being either the isotropic (I), plastic solid (PS), or solid (S) phases, for the HGO model (this work) and HE (Frenkel and Mulder [11]) with molecular elongation $\kappa = 1.25$. The density and pressure are given in standard reduced units of $P^* = \beta P D^3$ and $\rho^* = \rho D^3$. The last column includes the values of the reduced Gibbs free energy at the transitions.

I–II	system	$\rho^*_{\rm I}$	$\rho^*_{\rm II}$	P^*	g
I–PS	HGO	0.800(3)	0.842(3)	12.57(23)	20.237(15)
	HE	0.786	0.831	11.47	18.44
PS–S	HGO	1.0241(13)	1.0405(15)	62.0(1.1)	71.486(17)

4.5.2 Location of phase transitions

In Table 4.8 we give the coexistence properties at the I–PS and PS–S transitions for the HGO model with molecular elongation $\kappa = 1.25$. For comparison, we include data of Frenkel and Mulder [11] for a system of HE molecules at the same elongation. The coexistence properties at the I–PS transition found for the HE model are lower than those corresponding to the HGO model. The PS–S transition in the HE model is reported to be continuous. According to our data, this transition is first order in the HGO model as shown in Fig. 4.4, with a relative density jump at the transition of $\Delta\rho^* = 2(\rho^*_{\rm PS} - \rho^*_{\rm S})/(\rho^*_{\rm PS} + \rho^*_{\rm S}) = 0.016$.

We have estimated the uncertainty in the transition pressures. As shown by de Miguel [33], the uncertainties in the pressure and Gibbs free energies at the transition between two phases I and II separated by a first-order transition are related by

$$\varepsilon_P = (\Delta v)^{-1} \varepsilon_g \,, \tag{4.28}$$

where $\epsilon_g = \varepsilon_{g\rm I} + \varepsilon_{g\rm II}$ with $\varepsilon_{g\rm I}$, $\varepsilon_{g\rm II}$ representing the uncertainties in the Gibbs free energy of phases I and II at the transition, respectively, and $\Delta v = v_{\rm I} - v_{\rm II}$ is the discontinuity of the volume per particle $v = V/N$ at the transition. According to Eq. (4.28), the uncertainty in the transition pressure will tend to be larger for weakly first-order transitions. The proof of the above equation is simple. Expanding the Gibbs free energy of phase I at the transition (P_t) in powers of P and keeping first-order terms, one finds

$$g_{\rm I}(P) = g_t + \left(\frac{\partial g_{\rm I}}{\partial P}\right)_t (P - P_t) = g_t + v_{\rm I}(P - P_t)$$

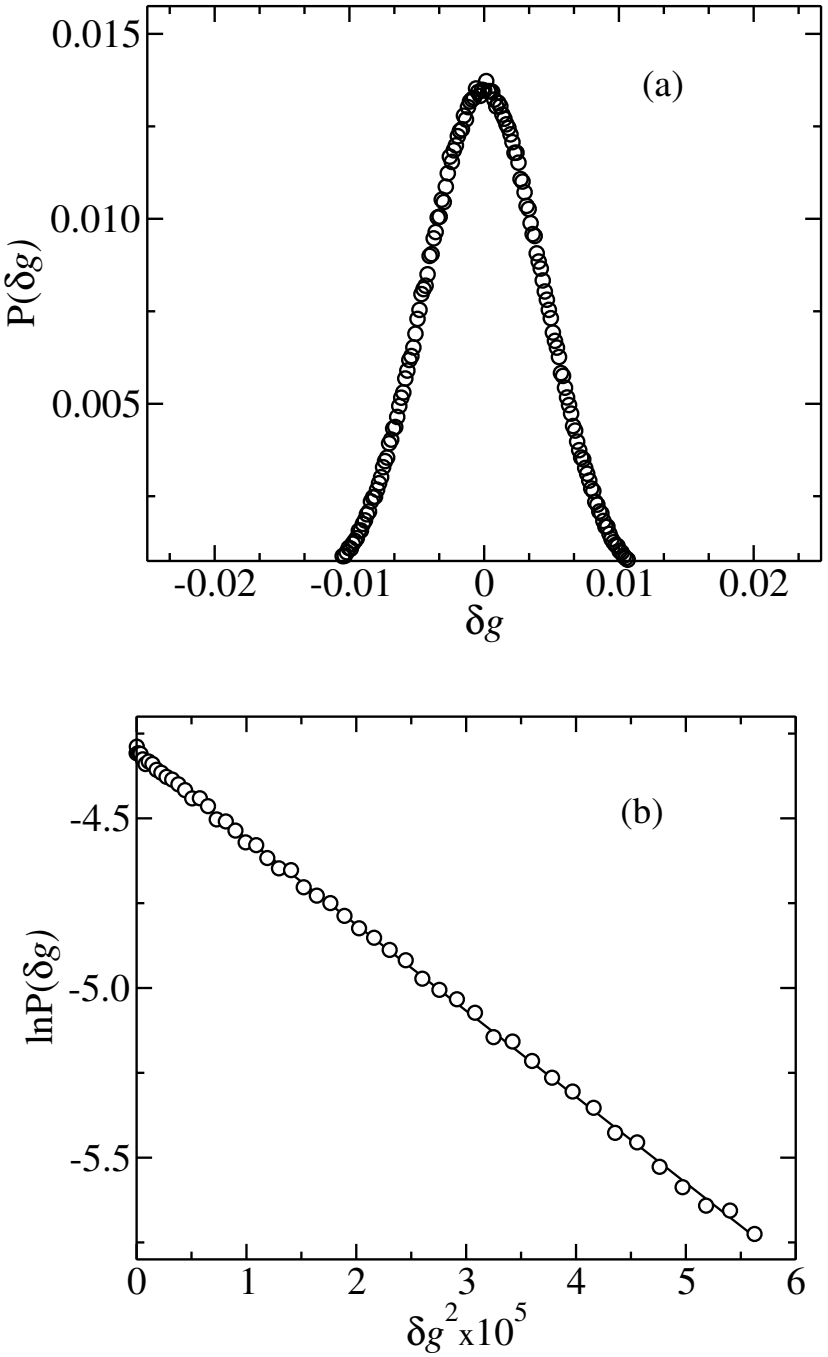

Figure 4.8: (a) Distribution of the reduced Gibbs free energy $\delta g = g - g_{\mathrm{I-PS}}$ resulting from a synthetic analysis at the isotropic (I)-to-plastic solid (PS) transition for HGO system with $\kappa = 1.25$. $g_{\mathrm{I-PS}}$ is the reduced Gibbs free energy at the transition. (b) Logarithmic representation of data represented in (a).

A similar relation holds for phase II

$$g_{\rm II}(P) = g_t + v_{\rm II}(P - P_t)$$

Considering now $g'_{\rm I} = g_{\rm I} - \varepsilon_{g_{\rm I}}$, $g'_{\rm II} = g_{\rm II} + \varepsilon_{g_{\rm II}}$ and solving the coexistence condition for the transition pressure P_t, $g'_{\rm I}(P'_t) = g'_{\rm II}(P'_t)$, we obtain $P'_t = P'_t + \varepsilon_P$ with ε_P given by Eq. (4.28). Similarly, if we consider $g'_{\rm I} = g_{\rm I} + \varepsilon_{g_{\rm I}}$ and $g'_{\rm II} = g_{\rm II} - \varepsilon_{g_{\rm II}}$, we find $P'_t = P'_t - \varepsilon_P$.

We illustrate the application of Eq. (4.28) for the estimation of the uncertainty in the I–PS transition pressure. The free energy of the isotropic fluid reference state was determined from the particle-insertion method. We reported a value $g^{\rm I}_{\rm ref} = 9.842$, with an associated error $\varepsilon_{\rm ref} = 0.007$. The statistical uncertainty associated with the thermodynamic integration of the equation of state is estimated from a synthetic analysis, as explained earlier in §4.3.3 (see Fig. 4.8). From this analysis, we find $\varepsilon_{\rm int} = 0.009$. It then follows that the uncertainty of the Gibbs free energy at the isotropic side of the transition is $\varepsilon_{g_{\rm I}} = (\varepsilon^2_{\rm ref} + \varepsilon^2_{\rm int})^{1/2} = 0.011$. For the plastic solid phase we find $\varepsilon_{\rm ref} = 0.002$, and $\varepsilon_{\rm int} = 0.003$, the latter being estimated from a synthetic analysis. This yields $\varepsilon_{g_{\rm II}} = 0.0036$. The discontinuity of the volume per particle at the transition is $\Delta v^{-1} = 15.84$. Finally, we obtain $\varepsilon_P = 0.23$ from Eq. (4.28). The same analysis will be applied hereafter for estimating the statistical error associated with transition pressures.

4.6 HGO model $\kappa = 2$

In Fig. 4.9 we show the equation of state of the HGO model for molecular elongation $\kappa = 2$ as obtained from computer simulation. For this value of κ the model exhibits isotropic and solid phases. A total of 21 state points are simulated in the fluid range $5 \leq P^* \leq 25$. Each point is equilibrated for 2×10^5 cycles and averages are collected over 2×10^5 additional cycles. No crystallization is observed when the system is compressed.

We perform two NPT series in the solid phase. A first series is started from a lattice configuration consisting on $N = 600$ particles with ABC stacking at $P^* = 41$. A total of 20 solid state points in the range $14 \leq P^* \leq 41$ are simulated. Each state point is equilibrated over 3×10^5 cycles and averages are taken over 3×10^5 additional cycles. A second series is started from a lattice with AB stacking at $P^* = 41$. Below $P^* = 14$ both crystal structures become mechanically unstable and melt into the fluid phase. According to the behaviour of the order parameters S and Ψ_6 during the simulations, no intermediate PS phase is observed.

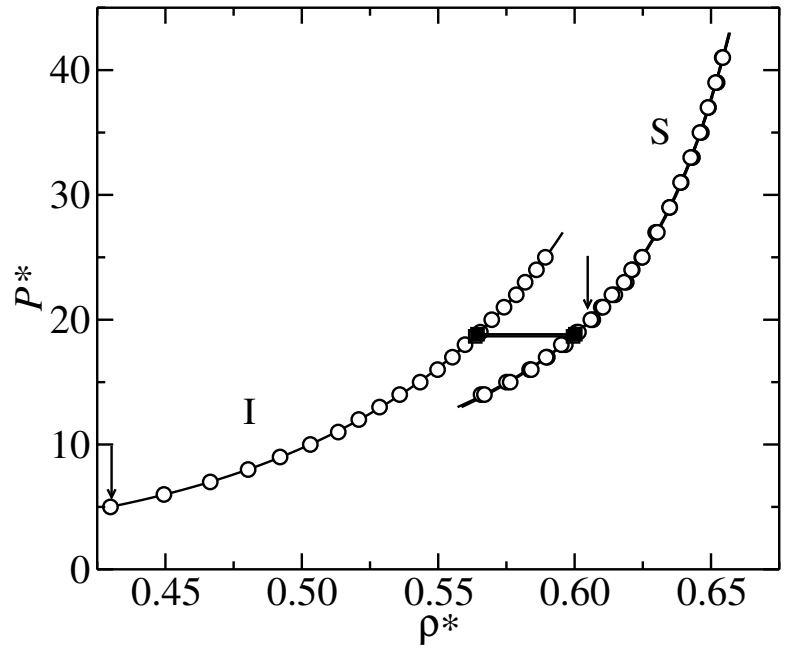

Figure 4.9: Pressure P^* vs density ρ^* for a system of HGO molecules with elongation $\kappa = 2$ in the isotropic (I) and solid (S) regions. Continuous lines are fits to the simulation data. Filled squares indicate the I–S transition. Arrows indicate the reference states considered for the free energy calculation of each phase. Pressure is expressed in units of $P^* = \beta P D^3$ and the density $\rho^* = \rho D^3$. Error bars are smaller than the size of the symbols.

Table 4.9: Fitting coefficients for the fluid and solid phases of a system of HGO molecules with molecular elongation $\kappa = 2$. Also included are the χ^2 values resulting from the fits.

a_m	fluid	solid (ABC)	solid (AB)
a_1	2.61515	5.73755	6.13313
a_2	1.90529	1.31393	1.27458
a_3	-0.02267	0.00310	0.00431
a_4	0.00053	-3.13×10^{-5}	-4.35×10^{-5}
a_5	-4.85×10^{-6}		
χ^2	10.7	23.9	57.6

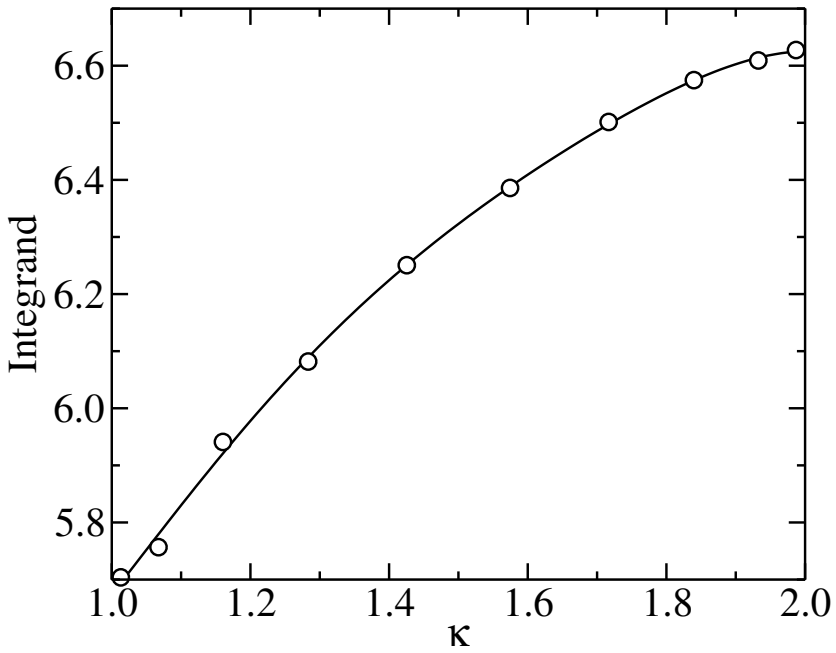

Figure 4.10: Behaviour of the integrand in Eq. (4.16) corresponding to the parametric integration in the fluid phase of the HGO system with $\kappa = 2$ starting from the HS fluid at pressure $P^* = 5$. Error bars are smaller than the size of the symbols.

4.6.1 Free energy calculations

The Gibbs free energy of the fluid and solid phases is computed from thermodynamic integration. For each phase, the compressibility factor is fitted to a polynomial in P^*. The corresponding fitting coefficients are given in Table 4.9.

We consider $P^* = 5$ as the reference fluid state. The corresponding Gibbs free energy is determined from parametric integration, using the molecular anisotropy κ as the integration parameter [see Eq. (4.16)]. For this purpose, we consider a constant-pressure path that links the fluid phase of the $\kappa = 2$ HGO system with the fluid phase of a system of hard spheres ($\kappa = 1$). A 10-point Gaussian quadrature is used to compute the integration appearing in Eq. (4.16). The variation of the integrand along the integration range is shown in Fig. 4.10.

We consider $P^*_{\rm ref} = 20$ as the reference solid state. The Helmholtz free energy of this state is computed by using the EC method appropriate for molecular crystals. First, we determine the equilibrium lattice parameters of the solid from a constant-pressure simulation at $P^*_{\rm ref}$ (we find $\rho^*_{\rm ref} = 0.60555$).

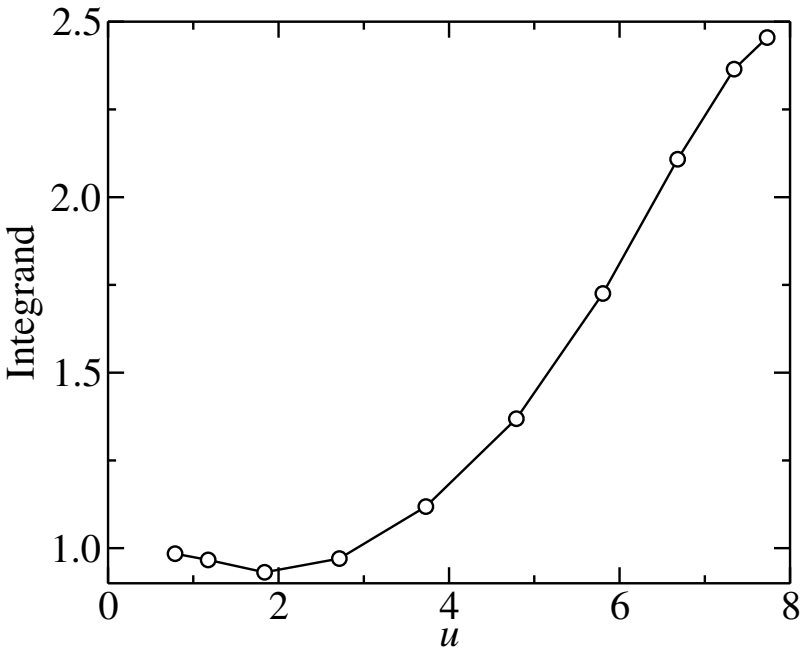

Figure 4.11: Variation of the integrand with the integration variable u in the 10-point Gaussian quadrature for the computation of $\Delta f_{\xi}^{\mathrm{CM}}$ for the $\kappa = 2$ HGO solid at $P^* = 20$. The line is a guide to the eye. The error bars are smaller than the size of the symbols.

The simulation consists on 6×10^5 cycles plus 3×10^5 cycles for collecting averages. As usual, a path at constant density which connects the solid under study with a non-interacting EC with fixed center of mass and with the same structure, is considered. The coupling constans are $\xi \equiv \lambda_t = 2500\, k_{\mathrm{B}}T$ and $\lambda_r = 10\xi$. The Helmholtz free energy of the reference solid state is then calculated from Eq. (4.27). Δf_{χ} is computed in an expanded ensemble simulation consisting on 5×10^5 after a previous equilibration stage of 5×10^4 cycles. The contribution $\Delta f_{\xi}^{\mathrm{CM}}$ is numerically calculated from a 10-point Gaussian quadrature. For this integration, we consider once again the same variable change considered before for the $\kappa = 1.25$ molecular solid. The variation of the integrand with the integration variable is depicted in Fig. 4.11. Each of the corresponding NVT simulations are first equilibrated for 5×10^4 cycles and then run for 5×10^5 cycles for calculating averages. The different contributions to the free energy of the reference solid state are gathered in Table 4.10.

Table 4.10: Relevant contributions to the free energy of the ABC and AB crystalline phase of the $\kappa = 2$ HGO model at the reference pressure $P^*_{\rm ref} = 20$. $f^{\rm CM}_{\rm EC}$ is the free energy of the non-interacting EC, $\Delta f^{\rm CM}_{\chi}$ is the free energy difference between the interacting and non-interacting EC with harmonic coupling constants $\lambda_t = 2500 k_{\rm B}T$ and $\lambda_r = 25000 k_{\rm B}T$. $\Delta f^{\rm CM}_{\xi}$ is the free energy difference between the HGO solid and the interacting EC. The ABC solid is more stable than the AB solid at this pressure.

	$\rho^*_{\rm ref}$	$f^{\rm CM}_{\rm EC}$	$\Delta f^{\rm CM}_{\chi}$	$\Delta f^{\rm CM}_{\xi}$	$\Delta f^{\rm CM}$	$f_{\rm ref}$	$g_{\rm ref}$
ABC	0.60555	20.8220	0.00654(5)	−10.177(4)	−0.0168	10.635(4)	43.663(4)
AB	0.60668	20.8220	0.00601(8)	−10.097(7)	−0.0168	10.714(7)	43.680 (7)

Table 4.11: Coexistence properties of the I–II transition, with I being the isotropic phase and II either the ABC or AB solid, for the HGO model (this work) and HE (Frenkel and Mulder [11]) with molecular elongation $\kappa = 2$. The pressure and density are given in standard reduced units of $P^* = \beta P D^3$ and $\rho^* = \rho D^3$. The last column includes the values of the reduced Gibbs free energy at the transition.

I–II	system	$\rho^*_{\rm I}$	$\rho^*_{\rm II}$	P^*	g
I–ABC	HGO	0.56357(10)	0.59942(11)	18.67(21)	41.450(22)
I–AB	HGO	0.56441(11)	0.60024(12)	18.84(24)	41.753(25)
I–AB	HE	0.5925	0.6262	23.48	49.03

4.6.2 Location of phase transitions

The corresponding coexistence values for the I–ABC and I–AB transitions are collected in Table 4.11 . For comparison, we also include data for systems of hard ellipsoids obtained by Frenkel and Mulder [11]. The I–AB transition pressure is found to be smaller for the HGO model than that corresponding to the HE model.

We have investigated the relative stability of the ABC and AB solid structures with respect to the fluid phase. According to the data included in Table 4.10, the Gibbs free energy of the ABC structure is lower than that of the AB structure at the reference pressure $P^*_{\rm ref} = 20$. A similar conclusion follows for pressures in the region where the melting transition takes place. As shown in Fig. 4.12, $\Delta g = g_{\rm ABC} - g_{\rm AB}$ is always negative in this region. On the other hand, Δf appears to increase with increasing pressure. This

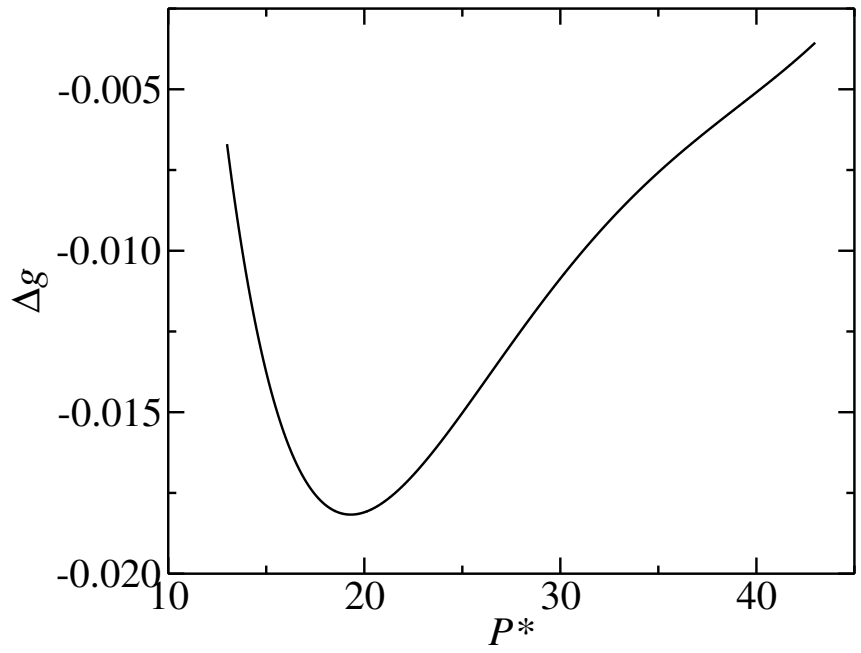

Figure 4.12: Gibbs free energy difference $\Delta g = g_{\rm ABC} - g_{\rm AB}$ between the ABC and AB crystalline structures for the HGO system with $\kappa = 2$ as a function of the reduced pressure.

Table 4.12: Coexistence properties for the ABC–AB transition of the HGO system with molecular elongation $\kappa = 2$.

$\rho^*_{\rm ABC}$	$\rho^*_{\rm AB}$	$f^*_{\rm ABC}$	$f^*_{\rm AB}$	P^*	g
0.66328(8)	0.66350(9)	15.001(20)	15.026(20)	50.4(3)	91.061(20)

behaviour seems to indicate that an ABC–AB transition might take place at sufficiently high pressure. This value, however, lies outside the range of pressures for which the solid phase is simulated. In order to check whether or not a structural transition takes place, we perform additional simulations involving a compression of the ABC and AB structures up to $P^* = 65$. We find an ABC–AB transition at $P^* = 50.4$ characterized by a very small relative density jump of $\Delta\rho^* = 2(\rho^*_{\rm AB} - \rho^*_{\rm ABC})/(\rho^*_{\rm ABC} + \rho^*_{\rm AB}) = 0.00033$. As expected, the ABC-AB structural transition is very weakly first order. The coexistence values at the ABC–AB transition are given in Table 4.12. The uncertainties in the I–ABC, I–AB, and ABC–AB transition pressures are estimated in a similar way as they were for molecular elongation $\kappa = 1.25$.

4.7 Phase diagram

Once the coexistence properties at a molecular elongation κ are determined, one can trace out the transition lines in the P^*–κ plane using the Gibbs-Duhem method. The method involves an integration of the Clausius-Clapeyron equation. We use for this purpose a fourth-order Runge-Kutta algorithm, as described in detail in chapter 2. The generalized Clausius-Clapeyron equation, Eq. (2.72), is written here as

$$\frac{d\ln P}{dx} = -\frac{\Delta\Omega}{P\Delta v} \equiv \Phi\,.$$

We choose $x = \ln D$ as the integration parameter. In practice, the integration of the above first-order differential equation is made by considering LD^2 as the unit of volume. In terms of this unit, we define $P^+ = \beta P L D^2$, and $v^+ = v/(LD^2)$. $\Omega^+ = (\partial g/\partial x)_{P^+}$ was already defined in Eq. (4.22). Here, $\Delta v^+ = v_{\rm I}^+ - v_{\rm II}^+$, and $\Delta\Omega^+ = \Omega_{\rm I}^+ - \Omega_{\rm II}^+$, where I and II denote the two coexisting phases. If the coexistence pressure is known for a value of x, the calculation of the coexistence pressure at $x' = x + \Delta x$ involves the following steps:[1]

1. Perform two independent NPT simulations of phases I and II at the coexisting pressure P_1 and molecular elongation κ. Run averages for Ω^+ and v^+ are computed in each phase. We recall from Eq. (4.26) that $\Omega^+ = -1 - (1/3)(\Omega_D^+ - 2\Omega_L^+)$, where Ω_D^+ and Ω_L^+ were defined in Eq. (4.24). For the calculation of Ω_L^+, we compute the number of overlaps resulting from a small perturbation involving a change of the molecular length from $\ln L$ to $\ln L + \xi$ at constant D and P^+. A total of 5 values of ξ are considered and the value of Ω_L^+ follows from extrapolation to $\xi \to 0$. A similar procedure is considered for the calculation of Ω_D^+, the perturbations now involving changes from $\ln D$ to $\ln D + \xi$ at constant L and P^+. By the end of this stage, $\Delta\Omega^+$ and Δv^+ are available and hence, $\Phi_1 \equiv \Phi(x, P_1^+)$.

2. Predict a value of the coexistence pressure, $P_2^+ = P_1^+ \exp(\Phi_1 \Delta x/2)$, at the midpoint $x_{\rm half} = x + \Delta x/2$ of the integration range. Two independent constant-pressure simulations of phases I and II are performed at pressure P_2^+ and elongation parameter $x_{\rm half}$. By the end of this stage, we compute Δv^+ and $\Delta\Omega^+$ and hence, $\Phi_2 = \Phi(x_{\rm half}, P_2^+)$.

[1] According to our choice of integration variable and unit of volume, $LD^2 = \kappa D^3 = 1$, it follows that x and the molecular anisotropy are related by $x = (-1/3)\ln\kappa$. Thus, the integration step is related to the old (κ) and new (κ') molecular elongations by $\Delta x = (1/3)\ln(\kappa/\kappa')$.

3. Correct the value of the pressure at $x_{\rm half}$ as $P_3^+ = P_1^+ \exp\left(\Phi_2 \Delta x/2\right)$. Two independent constant-pressure simulations of phases I and II are carried out at P_3^+ and elongation parameter $x_{\rm half}$, from which we get $\Phi_3 = \Phi(x_{\rm half}, P_3^+)$.

4. Predict the coexistence pressure at $x' = x + \Delta x$ as $P_4^+ = P_1^+ \exp(\Phi_3 \Delta x)$ and perform two independent constant-pressure simulations of phases I and II at P_4^+ and elongation parameter x' (i.e., molecular elongation κ'). The main output of the simulations is the corresponding value of $\Phi_4 = \Phi(x', P_4^+)$. The final value of the coexistence pressure at the new elongation κ' is obtained from

$$P^+(\kappa') = P^+(\kappa) \exp\left[\frac{1}{6}\left(\Phi_1 + 2\Phi_2 + 2\Phi_3 + \Phi_4\right)\Delta x\right] \tag{4.29}$$

   with $\Delta x = (1/3)\ln(\kappa/\kappa')$.

The above scheme is applied to determine the I–PS, I–S, and PS–S coexistence lines. An ABC stacking is always assumed for the PS and S phases. Starting from the appropriate transition point, two simulation series are performed: one increasing the value of the molecular elongation, and a second one decreasing κ. In all cases, the initial configuration for each step is taken from the final configuration of the previous step. When κ is increased, this is accompanied by a scaling transformation in steps 2 and 4 in order to prevent starting from a configuration containing overlaps. This scaling involves expanding the dimensions of the simulation box, as well as the molecular positions, by a factor greater than unity. For the fluid phase, we consider a scaling factor κ'/κ. For the translationally ordered phases, we find it more convenient to start from a lattice configuration. At each step, phases I and II are first equilibrated over 2×10^5 cycles and averages are calculated over 40 blocks, each consisting on 5×10^3 cycles.

We use the fluid-solid transition point of a system of hard spheres obtained in this work to determine the I–PS coexistence line by increasing κ. As an assessment of the validity of the integration method, the value of $P^* = 12.308$ obtained from Gibbs-Duhem integration at $\kappa = 1.25$ should be compared with the value of $P^* = 12.57(23)$ obtained from free energy calculations. The Clausius-Clapeyron equation is integrated along the I–PS line up to $\kappa = 1.40$. Beyond this molecular elongation, the difference in density between the two coexisting phases turns very small and difficult to measure.

As for the PS–S coexistence line, we consider $P^* = 62$, $\kappa = 1.25$, as the starting point for the Gibbs-Duhem integration. The decreasing-κ series is

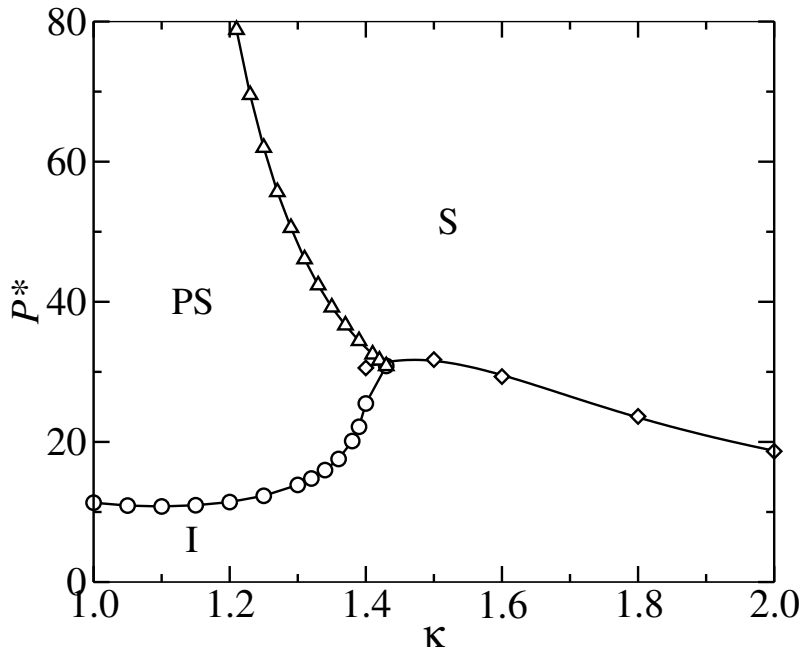

Figure 4.13: Phase diagram of the HGO model in the P^*–κ plane, showing the regions of stability of the isotropic fluid (I), plastic solid (PS), and solid (S) phases. Symbols correspond to results obtained from Gibbs-Duhem integration. Curves are included as a guide to the eye.

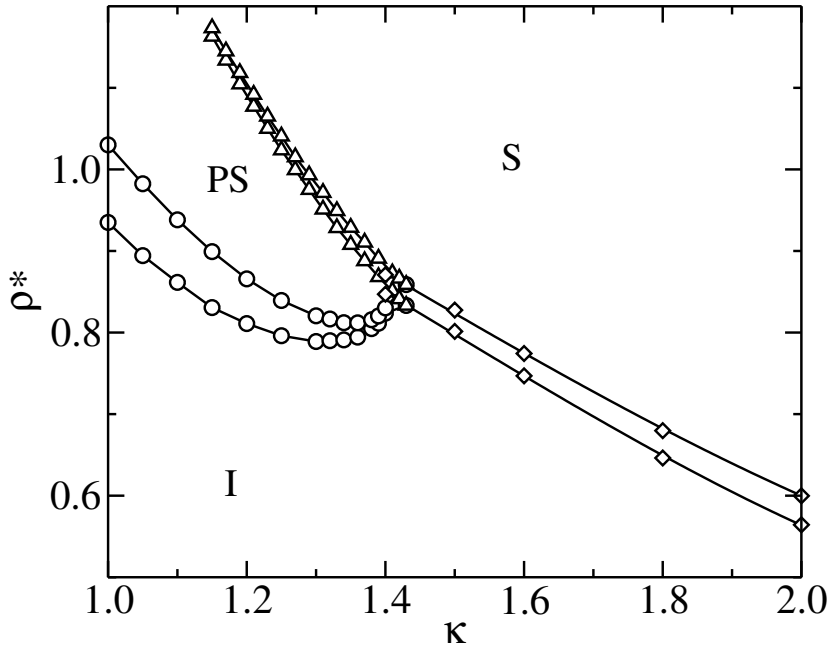

Figure 4.14: Phase diagram of the HGO model in the ρ^*–κ plane.

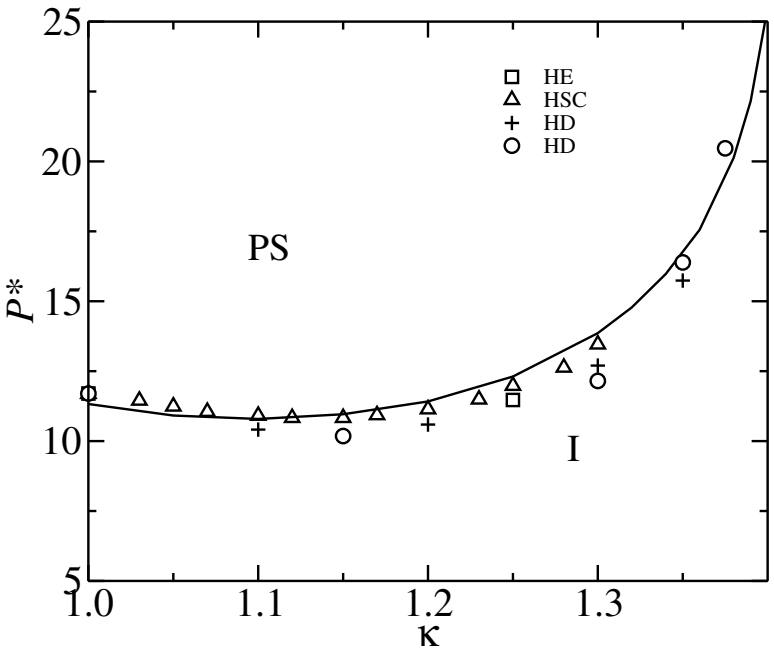

Figure 4.15: The I–PS coexistence line in the pressure-elongation plane for different hard-core models. The solid line is for the HGO model (this work). The symbols correspond to hard ellipsoids (HE, squares) [11], hard spherocylinders (HSC, up triangles) [70], and hard dumbbells (HD, circles) [75–77].

continued down to $\kappa = 1.19$, while the increasing-κ series is continued up to $\kappa = 1.43$. For the I–S coexistence line, we consider $\kappa = 2$ as the starting point for the integration. When κ is increased, we find that the fluid phase develops nematic ordering at about $\kappa = 2.3$. This will be discussed in the next chapter. On the other hand, we find that the orientational order of the solid phase along the decreasing-κ series is lost at $\kappa \approx 1.40$. At this elongation, the two coexisting phases actually correspond to a plastic solid and an isotropic fluid.

Our results are summarized in Figs. 4.13 and 4.14, where we show the phase diagram of the HGO model in the P^*–κ and ρ^*–κ plane, respectively. The phase behaviour of HGO systems is very similar to that reported for other hard-core models, such as the HE and HD models [see Fig. (4.15)]. This appears to indicate that it is the molecular anisotropy, and not the *molecular shape*, the relevant microscopic parameter that dictates the phase behaviour and phase stability for small non-sphericities. For small molecular anisotropies (close to $\kappa = 1$), the HGO solid melts into an orientationally disordered crystal when decreasing the pressure. This transition is weakly first order and the associated density change is small but measurable. The cor-

responding density change is found to be rather insensitive to the molecular anisotropy. At even lower pressures, the plastic solid looses the translational order and melts into an ordinary molecular fluid, the transition being accompanied by a density change that decreases with increasing κ. The range of stability of the plastic phase decreases rapidly with increasing molecular anisotropy, and the plastic phase becomes unstable beyond a certain value of κ. Beyond this value, the HGO solid melts directly into an isotropic fluid. The point where the I–PS, PS–S, and I–S coexistence lines meet defines a triple point in the model. From our simulation results, we infer that the triple point is approximately located at $\kappa \approx 1.43(1)$, the pressure being $P^* \approx 30.8(2)$.

4.8 Conclusions

A study of the phase diagram of the HGO model potential for small anisotropies ($1 \leq \kappa \leq 2$) has been reported in this chapter. In order to accomplish this goal, we have first determined the equations of state for selected values of κ using constant-pressure Monte Carlo simulation. The system is found to exhibit I, PS, and S phases, depending on the molecular anisotropy. Different simulation techniques, such as thermodynamic integration, parametric integration, Einstein crystal method, and expanded ensemble, have been used for the computation of the free energy of the different phases. All of the phases are separated by first-order transitions, which have been located by equating the Gibbs free energy of the phases. The obtained coexistence pressures have been used as starting points for an integration of the Clausius-Clapeyron equation. This has allowed us to obtain the full coexistence lines in the range of molecular elongations under consideration.

The plastic solid phase is found to be stable in the range $1 \leq \kappa \leq 1.43$. For larger molecular elongations, the HGO solid melts directly into an isotropic molecular fluid. We have shown that the ABC solid is more stable than the AB solid close to melting for $\kappa = 2$. This has not been explicitly checked for other elongations. Considering that for hard spheres the fcc (ABC) structure is more stable than the hcp (AB), it seems plausible to conclude that the ABC solid structure will be the most stable structure when melting takes place. We have also shown that the $\kappa = 2$ HGO solid undergoes an ABC–AB structural transition at sufficiently high pressure. This is expected to occur also for smaller elongations. We should mention that the plastic solid has always been assumed to have an ABC stacking. We have not explored whether other crystalline lattices are actually more stable.

A comparison with other hard-core models shows that all exhibit a similar phase behaviour for small non-sphericities. The PS–S transition for the HGO model is found to be first order. However, Frenkel and Mulder [11] report this transition to be continuous for HE. We believe that a more detailed analysis of this transition for a system of HE would probably reveal that this transition is actually first order. As for HSC, Bolhuis and Frenkel [70] have shown that the isotropic liquid freezes into a plastic solid phase for molecular elongations $\kappa \leq 1.35 \pm 0.05$. Moreover, the PS–S transition is reported to be first order. A similar conclusion is found for hard dumbbells. As far as the phase behaviour is concerned, this shows that the molecular shape is an irrelevant molecular parameter for hard-core models. This only holds true for small non-sphericities.

Chapter 5

HGO model: large molecular anisotropies

We analyze in this chapter the phase diagram of the HGO model in the region of large molecular elongations ($2 \leq \kappa \leq 10$). Our strategy is similar to the one used in the previous chapter. We start by computing the equation of state for selected values of κ and the appropiate phase transitions are then located from free energy calculations. The phase diagram is finally completed by using the Gibbs-Duhem integration method. We find that in this range of molecular elongations the system exhibits a nematic (N) phase between the isotropic and solid phases. A detailed analysis of the N–S transition is presented. In addition, two crystalline structures with AB and ABC stacking are considered and their relative stability with respect to the nematic phase is studied. We also investigate the solid-solid transition involving these two crystalline structures that takes place at high pressure. We give an estimation of the location of the I–N–S triple point.

5.1 Introduction

One of the most relevant features of the HGO model, for large non-sphericities, is that a *liquid crystal* phase becomes stable between the disordered (isotropic) and the fully ordered (solid) phases. This new phase is characterized by long-range orientational order but translational disorder. This fluid phase is known as nematic.

The nematic phase has been previously reported in hard-core systems such as hard ellipsoids (HEs), hard spherocylinders (HSCs), and hard cylinders (HCs) using theoretical as well as simulation approaches. The first simulations of liquid crystal phases in hard-particle systems were due to

Vieillard-Baron [93]. He considered a system of HEs and showed that the system exhibits two first-order phase transitions: I–N and N–S. That work suggested that excluded-volume effects might play an essential role in the orientational phase transition of nematic liquid crystals. The phase diagram of the HE model (for both oblate and prolate molecules) was later determined by Frenkel and co-workers [11,49,81], who concluded that the nematic phase is only stable for molecular elongations $\kappa \geq 2.75$ (for prolate molecules), and $\kappa \leq 1/2.75$ (for oblate molecules). No nematic phase was observed in the first simulations of systems of HSCs carried out by Vieillard-Baron [94]. This is probably due to an inappropriate choice of molecular elongation, as this system has been later shown to stabilize a nematic phase [70, 78, 95, 96, 101] for molecular elongations $\kappa \geq 4.7$. A theoretical study due to Holyst and Poniewierski [102] within the smoothed-density approximation arrived to the conclusion that, for systems of HEs and HSCs, the nematic phase is not stable for a range of molecular elongations close to $\kappa = 1$, while for HCs, the nematic phase is stable for all molecular elongations.

Much is known about the isotropic phase of the HGO model and some theoretical and simulation work has been done to investigate the nematic phase in this model. Padilla and Velasco [103] have investigated the I–N phase transition in a system of moderately long molecules interacting through the HGO potential within the decoupling approximation and several of its extensions. They have reported a comparison between theoretical and simulation results for $\kappa = 3$ and 5. More recently, de Miguel and del Río [16, 73] have carried out a study of the HGO model over a range of molecular elongations $3 \leq \kappa \leq 15$, determining the equations of state of the I and N phases from computer simulation, and performing free energy calculations. A comparison of the results with predictions from several theoretical approaches based on the decoupling approximation showed that none of the approximations are very satisfactory in the description of the isotropic phase; however, the simple Parsons-Lee approximation yields quantitative agreement with the simulation data in the nematic phase. They have considered a detailed analysis of the I–N transition and computed the corresponding transition line in the P^*–κ plane using the Gibbs-Duhem integration method. They have also given quantitative evidence of the differences between the HGO and HE models in the I–N region. According to their conclusions, the coexisting properties are significantly lower in the HGO model.

No study of the crystalline phase has been reported so far for the HGO model. This is one of the main goals of this chapter. The N–S coexistence line is determined by numerical integration of the (generalized) Clausius-Clapeyron equation. The starting point for the implementation of the in-

tegration is determined from free energy calculations at appropriate values of κ. Two crystalline stuctures (with ABC and AB stacking) are considered and their relative stability with respect to the nematic phase is investigated. Our results are expected to yield an estimate of the location of the I–N–S triple point.

5.2 Simulation details

As mentioned before, a nematic phase is expected between the I and S phases. This phase is characterized by the fact that the long axis of the molecules are, on average, aligned along an arbitrary direction (called the director of the phase). In practice, the director is computed from the eigenvector associated with the largest eigenvalue of the ordering tensor $Q_{\alpha\beta}$ defined in Eq. (4.4). In addition, we also compute the orientational order parameter S in order to distinguish between the isotropic and nematic phases. The strategy here is similar to the one considered in the previous chapter. First, we perform series of NPT simulations in order to study the equations of state at given values of the molecular elongation. In particular, we consider $\kappa = 3.5$, 5, 7.5, and 10. We consider systems of $N = 500$ molecules for the fluid phases. The solid phase is started from a lattice structure consisting on 6 layers with 10×10 molecules per layer, which gives a total of $N = 600$ molecules. We then perform thermodynamic integration along the equations of state according to the methods described in chapter 2. This allows us to compute the free energy of each phase. We finally make use of the Gibbs-Duhem integration method to trace out the full coexistence line in the range $2 \leq \kappa \leq 10$.

5.3 Isotropic-nematic transition

The I–N transition in the HGO model has recently been studied by de Miguel and del Río [16]. The equations of state of the fluid phases of the model with $\kappa = 5$ were determined from NPT simulations in a range of pressures $0.40 \leq P^* \leq 1.50$. $N = 500$ molecules placed in a cubic box were considered in the simulations. Thermodynamic integration was used to compute the free energy of the I and N phases. The ideal gas was chosen as reference state in the isotropic phase. In order to calculate the free energy of the reference nematic state point ($P^*_{\rm ref} = 1.50$), they used the method proposed by Frenkel and Mulder [11] which consists on suppressing the I–N transition by applying

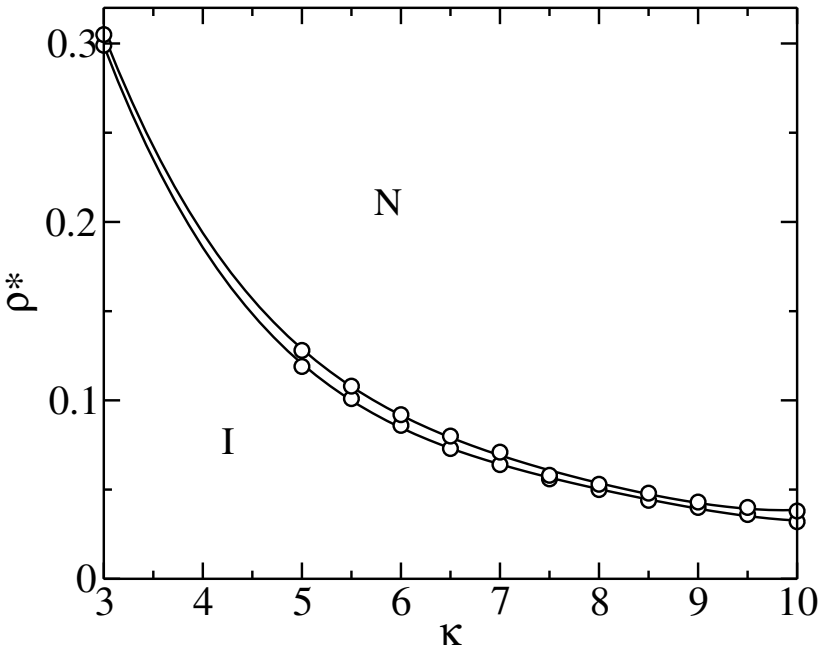

Figure 5.1: Coexistence densities ρ^* at the isotropic-nematic transition as a function of molecular elongation κ in the HGO model [16].

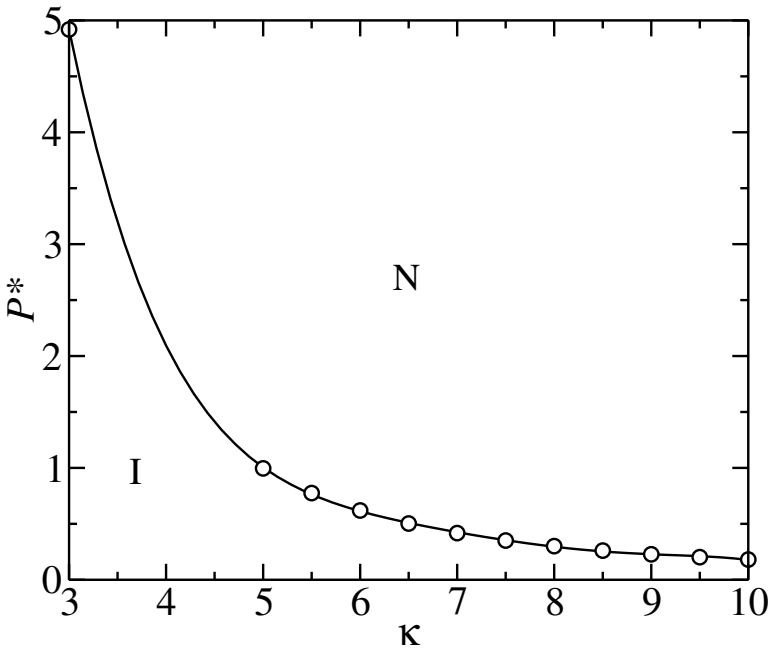

Figure 5.2: Coexistence pressure P^* at the isotropic-nematic transition as a function of molecular elongation κ in the HGO model [16].

an external orienting field $H_{\rm ext}$ [see chapter 2, Eq. (2.52)] of the form

$$H_{\rm ext} = \lambda \sum_{i=1}^{N} \sin^2 \theta_i \,,$$

where λ is the strength of the external field, and θ_i is the angle between the long molecular axis and the direction of the external field. A value $\lambda = 5\, k_{\rm B}T$ was seen to be large enough to suppress the I–N transition. By solving the coexistence condition Eq. (2.1), the I–N transition was found to take place at $P^* = 0.996$. The I–N coexistence line was determined by Gibbs-Duhem integration in the range $5 \leq \kappa \leq 10$. The resulting coexistence lines are shown in Fig. 5.1 (ρ^*–κ plane) and in Fig. 5.2 (P^*–κ plane). The I–N coexistence for molecular elongation $\kappa = 3$ was independently determined from thermodynamic integration methods. De Miguel and del Río compared their results with existing I–N coexistence data for the equivalent HE system. According to their results, the coexisting properties are lower in the HGO model than in the HE model.

5.4 Nematic-solid transition

5.4.1 Nematic phase

We show in Figs. 5.3 and 5.4 the equations of state of the HGO model for molecular elongations $\kappa = 3.5$, 5, 7.5, and 10 in the range of pressures where the system exhibits nematic and solid behaviour. For molecular elongation $\kappa = 3.5$, a total of 23 state points are simulated in the nematic phase, from $P^* = 3.25$ up to $P^* = 8.80$. For $\kappa = 5$, 21 state points are simulated in a range of pressures $1.50 \leq P^* \leq 6.25$. For both molecular elongations, each state point is equilibrated for 3×10^5 cycles and 2×10^5 further cycles are considered for computing averages over blocks of 2000 cycles. Constant-pressure simulations are performed from $P^* = 0.4$ up to $P^* = 5.5$, obtaining data for a total of 14 state points in the nematic phase for the HGO model with molecular anisotropy $\kappa = 7.5$. For $\kappa = 10$, we consider $N = 864$ molecules in the fluid phase. A total of 13 state points ranging from $P^* = 0.2$ up to $P^* = 5$ are simulated. For $\kappa = 7.5$ and $\kappa = 10$, each state point is equilibrated for 3×10^5 cycles and averages are determined over a further period of 3×10^5 cycles.

We use the thermodynamic integration method to determine the Gibbs

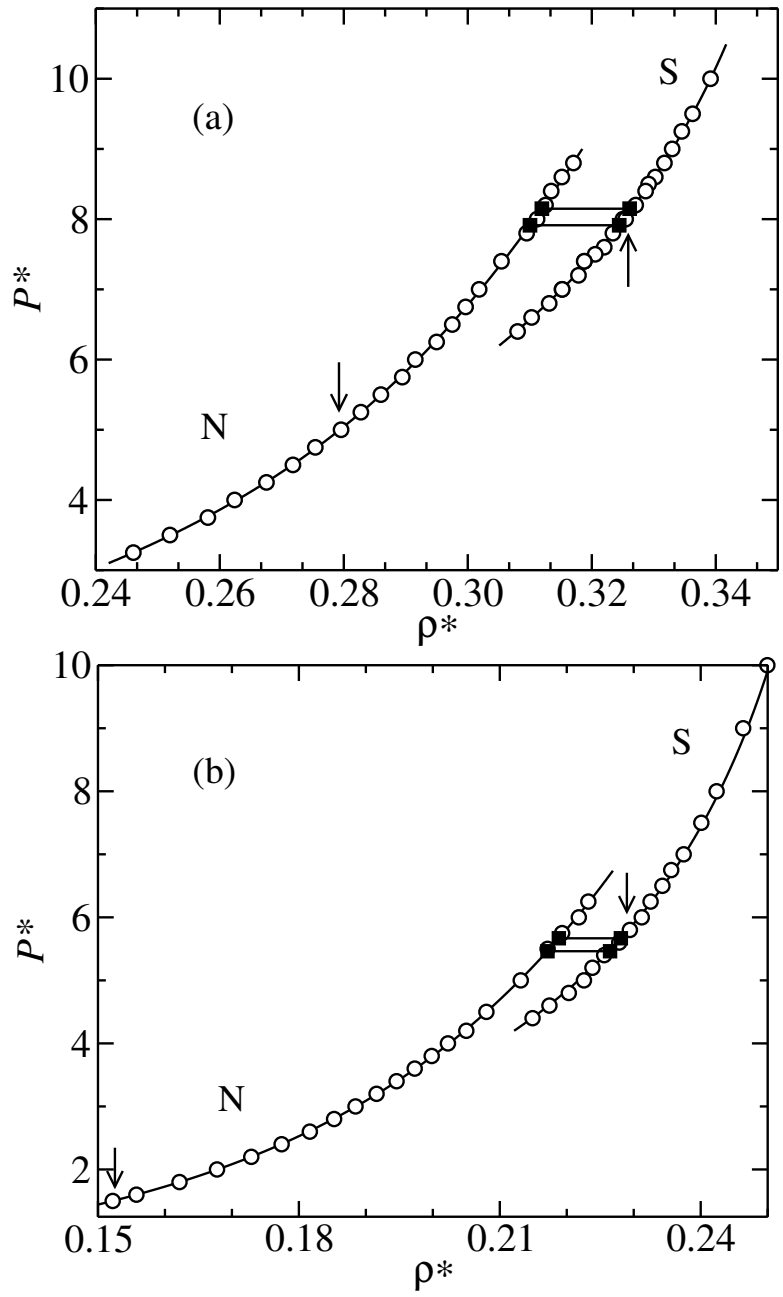

Figure 5.3: Pressure P^* vs density ρ^* for molecular elongation (a) $\kappa = 3.5$, and (b) $\kappa = 5$. in the nematic (N) and solid (S) region. Arrows indicate the states considered for the calculation of the free energy of each phase. We also indicate the location of the N–ABC (upper solid line) and N–AB (lower solid line) transitions. Reduced units are used, with $P^* = \beta P D^3$, and $\rho^* = \rho D^3$. The I–N transition takes place at $P^* = 4.919$ ($\kappa = 3.5$) and $P^* = 0.996$ ($\kappa = 5$). Error bars in the density are smaller than the symbol size.

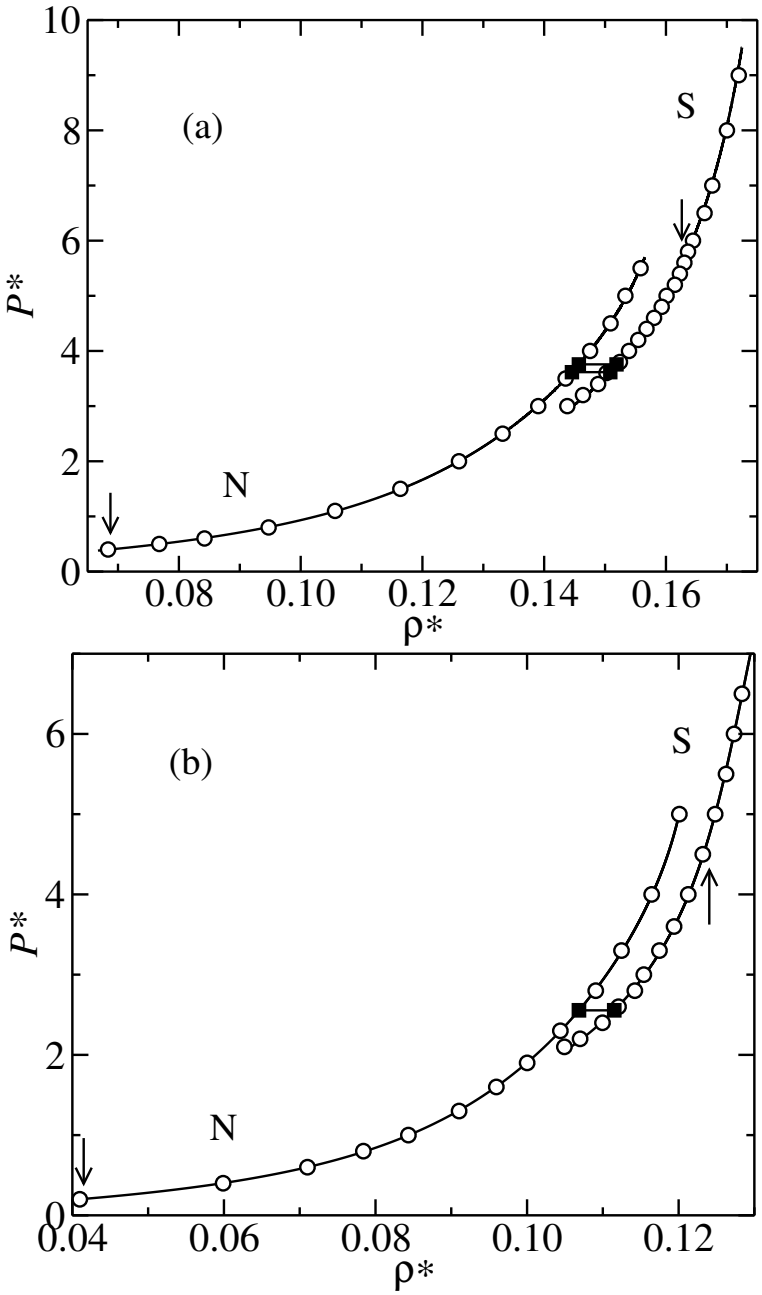

Figure 5.4: Pressure P^* vs density ρ^* for molecular elongation (a) $\kappa = 7.5$, and (b) $\kappa = 10$ in the nematic (N) and solid (S) region. Arrows indicate the states considered for the calculation of the free energy of each phase. We also indicate the location of the N–ABC (upper solid line) and N–AB (lower solid line) transitions. Reduced units are used, with $P^* = \beta P D^3$, and $\rho^* = \rho D^3$. The I–N transition takes place at $P^* = 0.351$ ($\kappa = 7.5$), and $P^* = 0.181$ ($\kappa = 10$). Error bars in the density are smaller than the symbol size.

Table 5.1: Fitting coefficients for the nematic phase corresponding to the HGO model with molecular elongations $\kappa = 3.5$, 5, 7.5, and 10. We include in the last row the range of pressures P_m^* up to P_M^* used in the fit.

a_n	$\kappa = 3.5$	$\kappa = 5$	$\kappa = 7.5$	$\kappa = 10$
a_1	4.54609	3.40577	3.08357	3.04704
a_2	2.62343	4.44752	7.00060	9.35241
a_3	0.01952	−0.10286	−0.35694	−0.60775
a_4	−0.00203	0.00326	0.02715	0.05621
(P_m^*, P_M^*)	(3.25, 8.80)	(1.50, 6.25)	(0.4, 5.5)	(0.2, 5)

free energy of the nematic phase

$$g(P^*) = g_{\rm ref} + \int_{P^*_{\rm ref}}^{P^*} Z(P^*) \frac{dP^*}{P^*} \,, \tag{5.1}$$

where $g_{\rm ref} \equiv g(P^*_{\rm ref})$. The integration in the above equation is performed by fitting the compressibility factor to a polynomial function in P^*. The fitting coefficients corresponding to each molecular elongation considered here are given in Table 5.1. In the following we give details of the calculation of $g_{\rm ref}$ for each molecular elongation considered. Further details can be found in §2.4.2.

For molecular elongation $\kappa = 5$, we use the method proposed by Frenkel and Mulder, and expand a (reference) nematic state at pressure $P^*_{\rm ref}$ to the ideal gas by applying an orienting external field. The Gibbs free energy of the reference nematic state point is given by (see Fig. 5.5)

$$g_{\rm ref} \equiv g_{\rm C} = g_{\rm B} + \Delta g_{\rm BC} \,, \tag{5.2}$$

where B corresponds to a nematic state at pressure $P^*_{\rm ref}$ with the external field switched on. We consider $P^*_{\rm ref} = 1.5$. The Helmholtz free energy of state B follows from Eq. (2.47)

$$f_{\rm B} = \ln \rho^*_{\rm B} - 1 + f_\lambda + \int_0^{\rho^*_{\rm B}} [Z(\rho^*) - 1] \frac{d\rho^*}{\rho^*} \,, \tag{5.3}$$

where Z is the compressibility factor of the HGO system under the presence of the external field, and f_λ is the contribution of the external field [cf. Eq. (2.54)]. A value $\lambda = 5\, k_{\rm B}T$ for the strength of the external field is found to be large enough to avoid a transition to an isotropic fluid at low

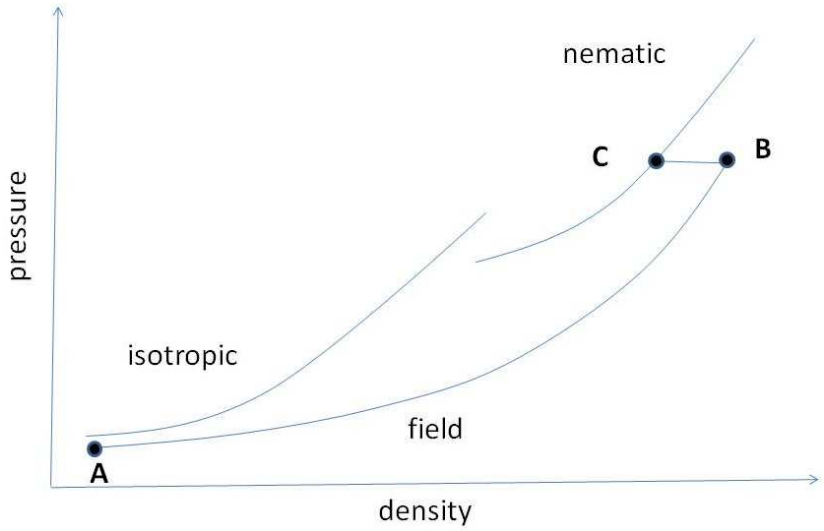

Figure 5.5: Schematic representation of the thermodynamic path used to compute the free energy of a reference nematic state.

pressures. We obtain in this case that $f_\lambda = 2.15671066$. The integration in the above expression requires Z to be known. For this purpose, the equation of state of the HGO system in the presence of the external field is determined from constant-pressure simulations for a total of 20 state points in the range $0.025 \leq P^* \leq 1.50$. We fit the simulation data of $Z(\rho^*)$ to a polynomial of order $M-1$ in ρ^*. Once $f_{\rm B}$ is calculated, the corresponding Gibbs free energy follows from $g_{\rm B} = f_{\rm B} + P^*_{\rm ref}/\rho^*_{\rm B}$. This value is seen to depend on the number of fitting coefficients. We find $g_{\rm B} = 13.855$, 13.856, and 13.841 when using $M = 6$, 7, and 8 coefficients, respectively. A similar dependence on the degree of the fitting polynomial was discussed in chapter 4 for the fluid phase of hard spheres. The impact of this systematic error on $g_{\rm ref}$ will be analyzed later for the present case. The scatter in the values of the Gibbs free energy arising from different choices of M is small, so we take the average value $g_{\rm B} = 13.851(36)$. The quoted error is estimated from a synthetic analysis, as detailed in chapter 4. The last step involves switching off the external field at constant pressure. As explained in §2.4.2, the corresponding change in Gibbs free energy is given by

$$\Delta g_{\rm BC} = \int_\lambda^0 d\lambda' \left\langle \frac{u(\lambda')}{\lambda'} \right\rangle ,$$

where $u(\lambda)$ is the interaction energy per particle. In practice, the integration is calculated by using a 10-point Gaussian quadrature. Such a numerical integration will work only if the integrand varies smoothly with λ. The behaviour

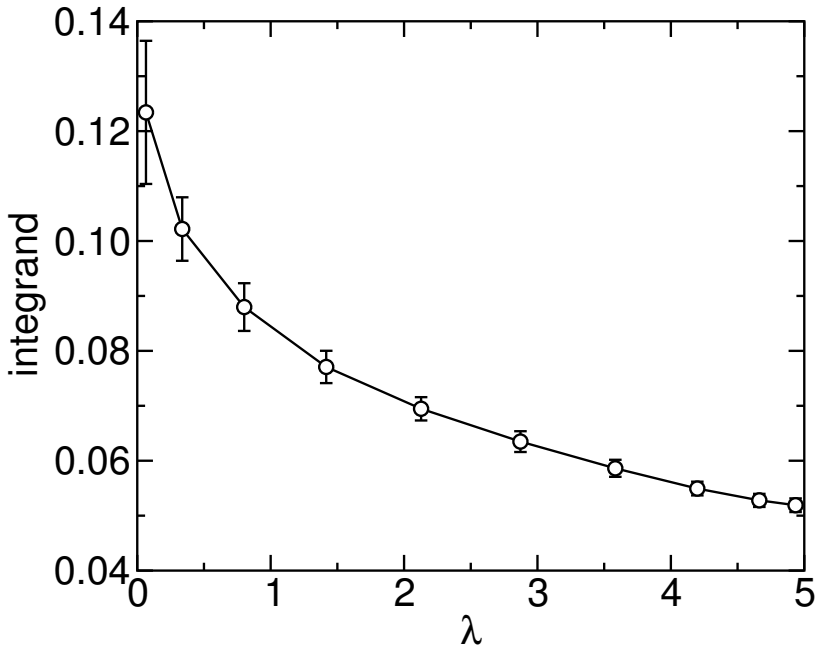

Figure 5.6: Gaussian integration for the calculation of the change in Gibbs free energy in the process of switching off the external field for a system of HGO molecules with $\kappa = 5$ at constant pressure $P^*_{\rm ref} = 1.5$.

of the integrand is shown in Fig. 5.6. We find a value $\Delta g_{\rm BC} = -0.355(5)$. Using Eq. (5.2), we find $g_{\rm C} \equiv g_{\rm ref} = 13.496(36)$ for the Gibbs free energy of the reference nematic state.

The above calculation is a bit lengthy, and one may wonder whether the calculated value of $g_{\rm ref}$ is actually correct. As an independent check, it was decided to compute $g_{\rm ref}$ from a totally different approach. For this purpose, we make use of the test-particle insertion method using the weighted implementation detailed in §2.3.4. We carry out a total of 10 independent runs at constant pressure $P^*_{\rm ref} = 1.5$, each consisting on 10^6 cycles, and 5000 particle insertions per cycle. We obtain a value of $g_{\rm ref} = 13.52(3)$. This value is fully consistent with the value obtained from thermodynamic integration.

We next turn to analyze the systematic errors associated with the integration in Eq. (5.3). Our approach is similar to the one used for investigating this source of errors when computing the free energy of the HS fluid. Rather than using the full integration in Eq. (5.3), we consider a restricted integration range and obtain $g_{\rm B}$ from

$$g_{\rm B} = g_0 + \int_{P^*_0}^{P^*_{\rm ref}} Z(P^*) \frac{dP^*}{P^*} \,, \tag{5.4}$$

Table 5.2: Values of the Gibbs free energy $g_{\rm ref}$ at a nematic reference state characterized by its pressure $P^*_{\rm ref}$, as calculated from different approaches: TI (thermodynamic integration), W(P^*_0) (Widom method applied at a pressure $P^*_0 = 0.5$, followed by a TI from $P^* = 0.5$ up to $P^* = 1.5$), and W($P^*_{\rm ref}$) (Widom method applied at the reference nematic pressure $P^*_{\rm ref} = 1.5$).

method	$g_{\rm ref}$
TI	13.496(36)
$W(P^*_0)$	13.507(6)
$W(P^*_{\rm ref})$	13.52(3)

where g_0 is the Gibbs free energy of the HGO system in the presence of the external field at some intermediate pressure P^*_0. We consider $P^*_0 = 0.5$. g_0 is now computed using the weighted particle-insertion method. At this pressure, the corresponding average density $\rho^*_0 = 0.10495(17)$ is low enough and the orientational order parameter $S = 0.85593(3)$ large enough for the particle-insertion method to be efficient. A total of 20 simulations consisting on 10^6 cycles with 1000 insertion attempts per cycle, are performed at $P^*_0 = 0.5$. The integration in Eq. (5.4) is performed after fitting Z to a polynomial of order $M - 1$ in P^*. We find $g_{\rm B} = 13.8622$, 13.8624, and 13.8624 when considering $M = 3$, 4, and 5 coefficients. As reported earlier for hard spheres, the systematic error associated with the fitting procedure is significantly reduced when the integration range is reduced. The value of $g_{\rm ref}$ follows from Eq. (5.2), using the value of $\Delta g_{\rm BC}$ previously computed. The value of the Gibbs free energy of the reference nematic state obtained from the three different routes are compared in Table 5.2.

For the calculation of the Gibbs free energy at reference nematic states for molecular elongations $\kappa = 7.5$ and 10, we use the weighted implementation of the particle-insertion method. According to Fig. 5.3, nematic ordering is found at relatively low densities, so the direct method is expected to perform efficiently. We consider $P^*_{\rm ref} = 0.4$ for $\kappa = 7.5$, and $P^*_{\rm ref} = 0.2$ for $\kappa = 10$. A total of 10 constant-pressure simulations consisting on 10^6 cycles are performed, with 2000 ($\kappa = 7.5$) and 1000 ($\kappa = 10$) particle insertions per cycle. The corresponding values of the Gibbs free energy are given in Table 5.3.

For the calculation of the Gibbs free energy of the reference state point at molecular elongation $\kappa = 3.5$ we use the parametric integration method (considering κ as the integration parameter) along a constant-pressure starting from a nematic state of the $\kappa = 5$ HGO system. We consider $P^*_{\rm ref} = 5$.

Table 5.3: Values of the Gibbs free energy $g_{\rm ref}$ of the nematic reference states characterized by their pressure, $P^*_{\rm ref}$, for different values of the molecular elongation κ as calculated from different methods: PI (parametric integration), TI (thermodynamic integration), and W (Widom insertion method).

κ	method	$P^*_{\rm ref}$	$g_{\rm ref}$
3.5	PI	5	24.322(19)
5	TI	1.5	13.496(36)
7.5	W	0.4	7.136(7)
10	W	0.2	5.353(6)

The Gibbs free energy of the $\kappa = 5$ HGO nematic fluid at this pressure is simply obtained from thermodynamic integration using Eq. (5.1). Referring back to Eq. (4.16), it follows that

$$g(P^*_{\rm ref}, \kappa = 3.5) = g(P^*_{\rm ref}, \kappa = 5) - \int_{3.5}^{5} \frac{d\kappa}{\kappa} \left(\frac{\partial g}{\partial \ln \kappa} \right)_{P^*} .$$

The above integration is carried out by using a 10-point Gaussian quadrature.

The values of the Gibbs free energy of the chosen reference nematic states corresponding to each value of κ are gathered in Table 5.3. Once the free energy of the reference nematic state is obtained, the free energy at any nematic pressure follows from Eq. (5.1).

5.4.2 Solid phase

We perform two simulation series for the solid phase of HGO models with $\kappa = 3.5, 5, 7.5$, and $\kappa = 10$. The initial configuration of the first series consists on a crystalline structure with the densest layers parallel to the xy plane, and in-layer hexagonal arrangement of the centers of mass of the molecules. The layers are stacked following an ABC structure. Six layers are considered, each one consisting on 10×10 molecules. A second series is started from a similar arrangement, but with an AB stacking of the layers. It is our purpose to investigate the relative stability of these crystalline structures with respect to the nematic phase.

For the $\kappa = 3.5$ HGO model, we first equilibrate a solid structure at $P^* = 10$. The system is then slowly expanded down to $P^* = 6.4$. A total of 22 state points are simulated along the solid branch. For molecular elongation $\kappa = 5$, we perform constant-pressure simulations in the range of pressures

Table 5.4: Fitting coefficients for the solid ABC structure of the HGO model for molecular elongations $\kappa = 3.5$, 5, 7.5, and 10. We include in the last row the range of pressures $P_m^* \leq P^* \leq P_M^*$ used in the fit.

a_n	$\kappa = 3.5$	$\kappa = 5$	$\kappa = 7.5$	$\kappa = 10$
a_1	6.43092	5.32159	5.13272	6.43250
a_2	2.13510	3.40731	5.17810	5.98425
a_3	0.01703	0.00637	0.00848	0.21907
a_4				−0.01431
(P_m^*, P_M^*)	(6.4, 10)	(4.4, 10)	(3, 9)	(2.1, 7.0)

Table 5.5: Fitting coefficients for the solid AB structure of the HGO model for molecular elongations $\kappa = 3.5$, 5, 7.5, and 10. We include in the last row the range of pressures $P_m^* \leq P^* \leq P_M^*$ used in the fit.

a_n	$\kappa = 3.5$	$\kappa = 5$	$\kappa = 7.5$	$\kappa = 10$
a_1	6.18850	5.52716	5.51538	5.22939
a_2	2.21146	3.36524	5.05059	6.91181
a_3	0.01173	0.00778	0.01735	−0.00206
a_4				0.00187
(P_m^*, P_M^*)	(6.8, 10)	(4.4, 10)	(3, 9)	(2.2, 7.0)

$4.4 \leq P^* \leq 10$. A total of 17 state points are simulated. For both elongations, each state point is first equilibrated for 2×10^5 cycles and averages are taken over 2×10^5 additional cycles. Averages are taken over blocks of 5000 cycles. For molecular elongation $\kappa = 7.5$, we consider 20 state points in the range of pressures $3 \leq P^* \leq 9$. Finally, a total of 15 solid states are simulated in the range $2.1 \leq P^* \leq 7.0$ for $\kappa = 10$. For the latter two elongations, the equilibration is extended to 3×10^5 cycles and the calculation of averages to 3×10^5 additional cycles. For all of the molecular elongations investigated here, the compressibility factors are fitted to a polynomial function in P^*. The corresponding fitting coefficients can be found in Tables 5.4 and 5.5.

We use the EC method to compute the absolute Helmholtz free energy of a reference state point in the solid phase for each value of the molecular anisotropy. NPT simulations at the appropriate reference pressure are performed to determine the average density of the solid, as well as its equilibrium structure. The free energy of the reference solid state is calculated

Table 5.6: Relevant contributions to the free energy of the solid phase at the corresponding reference pressure $P^*_{\rm ref}$. $f^{\rm CM}_{\rm EC}$ is the free energy of the non-interacting Einstein crystal with fixed center of mass, $\Delta f^{\rm CM}_{\chi}$ is the free energy difference between the interacting and non-interacting Einstein crystal with harmonic coupling constants $\lambda_t = \xi_{\rm max}$ and $\lambda_r = 10\xi_{\rm max}$ (in units of $k_{\rm B}T$). $\Delta f^{\rm CM}_{\xi}$ is the free energy difference between the HGO solid and the interacting Einstein crystal, and $\Delta f^{\rm CM}$ is the difference in free energy due to the constraint on the center of mass. In the last column is given the absolute free energy at the reference solid state.

κ	phase	$P^*_{\rm ref}$	$\rho^*_{\rm ref}$	$\xi_{\rm max}$	$f^{\rm CM}_{\rm EC}$	$\Delta f^{\rm CM}_{\chi}$	$\Delta f^{\rm CM}_{\xi}$	$\Delta f^{\rm CM}$	$f_{\rm ref}$	$g_{\rm ref}$
3.5	ABC	8	0.32549	1500	19.5462	0.00154(2)	−9.672(4)	−0.01786	9.857(4)	34.435(4)
	AB	8	0.32499	1500	19.5464	0.00158(9)	−9.677(9)	−0.01786	9.853(9)	34.469(9)
5	ABC	6	0.23112	1500	19.5462	0.00504(2)	−8.866(6)	−0.01843	10.666(6)	36.626(6)
	AB	6	0.23098	1500	19.5462	0.00610(6)	−8.845(6)	−0.01843	10.689(6)	36.665(6)
7.5	ABC	6	0.16433	3500	21.6624	0.0070(1)	−8.561(9)	−0.01900	13.090(9)	49.602(9)
	AB	6	0.16456	3500	21.6624	0.0090(2)	−8.480	−0.01900	13.172(18)	49.684(18)
10	ABC	4.5	0.12320	4000	21.9959	0.00571(7)	−8.601(10)	−0.01948	13.381(10)	49.908(10)

from [see chapter 2, Eq. (2.63); see also Eq. (4.27)]

$$f = f^{\rm CM}_{\rm EC} + \Delta f^{\rm CM}_{\chi} + \Delta f^{\rm CM}_{\xi} + \Delta f^{\rm CM}\,, \tag{5.5}$$

where $f^{\rm CM}_{\rm EC}$ and $\Delta f^{\rm CM}$ are calculated analitically. $\Delta f^{\rm CM}_{\xi}$ is calculated using a 10-point Gaussian quadrature. For this purpose, we run NVT simulations at values of the parameter ξ, with $\xi \equiv \lambda_t$, and $\lambda_r = 10\xi$, in the range $0 \leq \xi \leq \xi_{\rm max}$ consisting on 5×10^5 cycles after an equilibration of 5×10^4 cycles. $\Delta f^{\rm CM}_{\chi}$ is calculated from a simulation in the expanded ensemble (see chapter 2) consisting on 5×10^5 cycles. Here, a cycle involves N attempts to translate and rotate the molecules followed by an attempt to drive the non-interacting Einstein crystal into the interacting Einstein crystal (or viceversa).

The different contributions to the free energy of the reference solid state for the values of molecular elongations considered here, are collected in Table 5.6.

Table 5.7: Coexistence properties of the N–ABC and N–AB transitions for the HGO system with molecular elongations $\kappa = 3.5, 5, 7.5$ and 10. The N–AB transition is metastable with respect to the N–ABC transition.

transition	properties	$\kappa = 3.5$	$\kappa = 5$	$\kappa = 7.5$	$\kappa = 10$
N–ABC	$P^*_{\mathrm{N-ABC}}$	7.913	5.47(23)	3.62(13)	2.55(7)
	ρ^*_{N}	0.31003	0.2171(19)	0.1445(11)	0.1068(6)
	ρ^*_{ABC}	0.32442	0.2265(19)	0.1509(11)	0.1115(8)
	$g_{\mathrm{N-ABC}}$	34.169	34.291(43)	34.555(37)	33.450(29)
N–AB	$P^*_{\mathrm{N-AB}}$	8.15(21)	5.67(23)	3.76(16)	2.58
	ρ^*_{N}	0.3119(17)	0.2188(21)	0.1457(10)	0.1070
	ρ^*_{AB}	0.3261(18)	0.2281(21)	0.1519(14)	0.1118
	$g_{\mathrm{N-AB}}$	34.928(29)	35.220(48)	35.530(46)	33.688

5.4.3 Location of phase transitions

The location of the different transitions is accomplished by finding the pressure at which the Gibbs free energies of two phases become equal. The coexistence properties of the N–ABC and N–AB transitions for each value of κ considered here are given in Table 5.7. The uncertainties in the transition pressures are estimated in the same manner as in the previous chapter.

At a given pressure, the most stable phase is the one characterized by the lowest Gibbs free energy. The variation of the Gibbs free energy with pressure in the solid-nematic region is shown in Fig. 5.7. According to our results, the ABC crystalline structure is seen to be more stable than the AB structure when the solid phase melts into a nematic liquid. Furthermore, the ABC structure is more stable than the AB structure over the whole range of pressures studied here. This can be seen in Fig. 5.8, where we show the difference in Gibbs free energy, Δg, between the ABC and AB crystalline structures as a function of the reduced pressure P^*. Though Δg is seen to be negative at all pressures (this indicating that the ABC solid is more stable than the AB), there seems to be a strong indication that Δg may change sign at higher pressures: a transition between both structures will take place at a pressure such that $\Delta g = 0$. However, the resulting pressure lies outside the range of pressures considered for fitting the equations of state[1]. We then decided to slowly compress the ABC and AB solids up to

[1]Strictly speaking, the values of the free energies are valid for the range of pressures over which the fit was implemented. Extrapolation outside this range may give rise to inconsistent free energy values and is a bit risky.

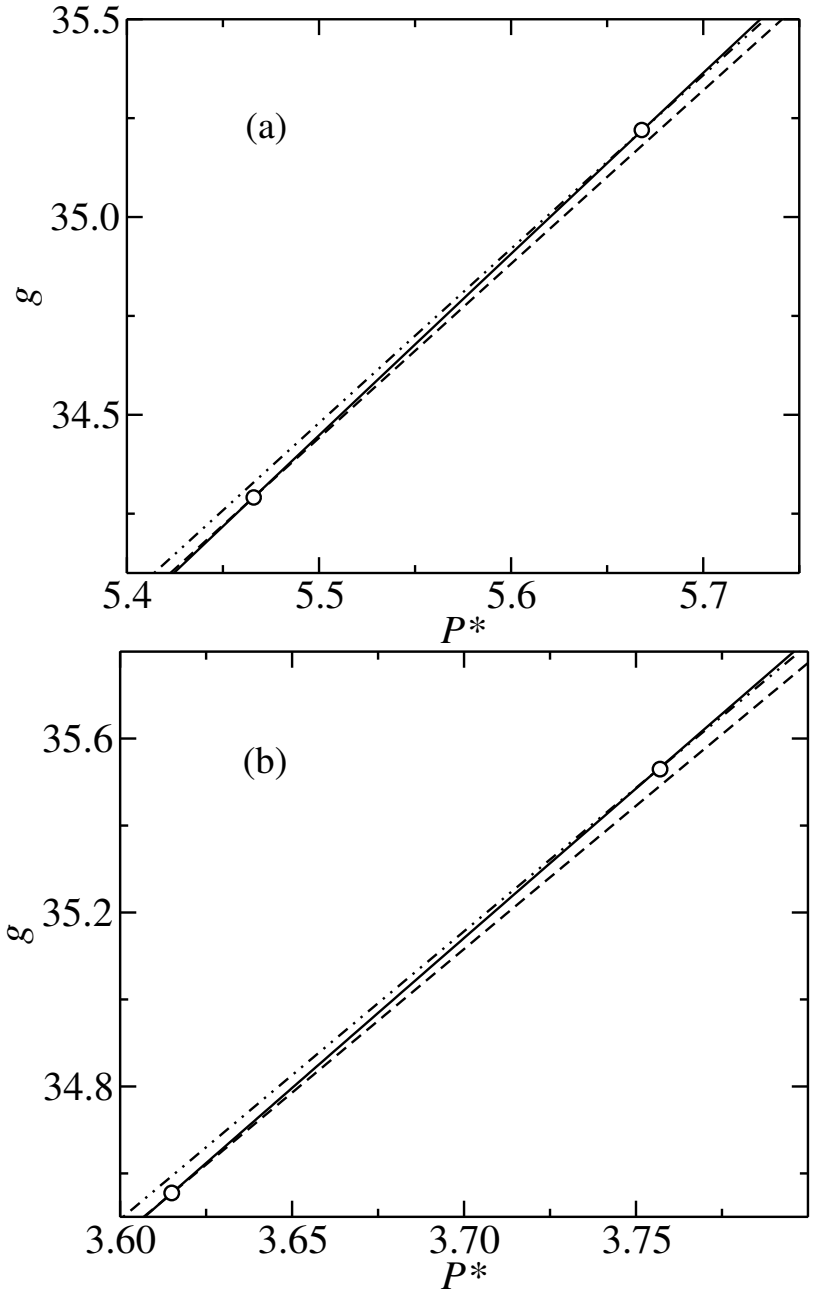

Figure 5.7: Gibbs free energy vs pressure in the nematic (continuous line), solid ABC (dashed line), and solid AB (dashed-dotted line) phases, in the neighbourhood of the nematic-to-solid transition. The points indicate the location of the N–ABC and N–AB transitions for: (a) $\kappa = 5$ ($P^* = 5.466$, and $P^* = 5.668$, respectively), and (b) $\kappa = 7.5$ ($P^* = 3.615$, and $P^* = 3.757$, respectively). The ABC structure turns out to be more stable than the AB structure.

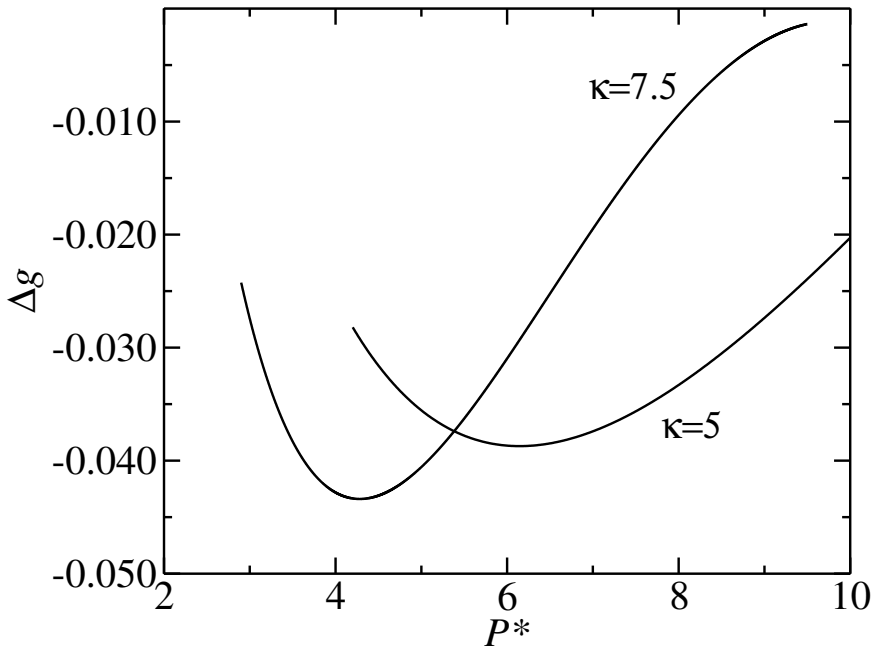

Figure 5.8: Gibbs free energy difference $\Delta g = g_{\rm ABC} - g_{\rm AB}$ between the ABC and AB crystalline structures for HGO models with $\kappa = 7.5$ (top curve) and $\kappa = 5$ (lower curve) as a function of the reduced pressure in the solid range considered here.

sufficiently high pressures in small jumps of pressures. The whole set of solid state points corresponding to each molecular elongation is then refitted to a polynomial in P^*, and expressions for the Gibbs free energy as a function of P^* are obtained following the same protocol as that used before. The corresponding properties at the ABC–AB transition are given in Table 5.8, where we also include the discontinuity of the packing fraction $\Delta\eta$ at the ABC–AB transition. As expected, $\Delta\eta$ increases with increasing molecular elongation.

5.5 Phase diagram

Having the coexistence properties of the N–S transition at the molecular elongations $\kappa = 3.5$, 5, 7.5, and 10, we have determined the location of the melting transition at intermediate molecular elongations using the Gibbs-Duhem method. As explained elsewhere, this method involves a numerical integration of the generalized Clausius-Clapeyron equation. For the present

Table 5.8: Coexistence properties for the ABC–AB transition of HGO systems with molecular elongations $\kappa = 3.5$, 5, 7.5, and 10.

κ	structure	P^*	ρ^*	η	$\Delta\eta$	f	g
3.5	ABC	42.206	0.38656	0.70840	0.00048	9.857	126.92
	AB		0.38682	0.70888		9.853	
5	ABC	22.458	0.26697	0.69894	0.00054	10.666	101.01
	AB		0.26718	0.69948		10.689	
7.5	ABC	9.411	0.17247	0.67729	0.00091	15.227	69.790
	AB		0.17270	0.67820		15.300	
10	ABC	5.673	0.12657	0.49705	0.00118	14.469	59.288
	AB		0.12687	0.49823		14.574	

application, this equation can be cast in the form

$$\frac{d\ln P}{dx} = -\frac{\Delta\Omega}{P\Delta v}\,, \tag{5.6}$$

where the parameter x is taken here as $x = \ln D$, $\Delta v = v_1 - v_2$, and $\Delta\Omega = \Omega_1 - \Omega_2$. A detailed explanation of the practical implementation of the fourth-order Runge-Kutta algorithm used for the numerical solution of Eq. (5.6) was given in § 4.7. Here, we consider two systems representing the two coexisting (nematic and ABC solid) phases, and independent NPT simulations are carried out for both systems. Typically, the systems are first equilibrated over 2×10^5 cycles and averages are collected over 2×10^5 additional cycles. The coexistence pressure at a new value of the molecular elongation is computed from Eq. (4.29).

We use the N–S coexistence pressure at $\kappa = 5$ as the starting point for an integration series where κ is decreased. In order to check the quality of the Gibbs-Duhem integration, a second simulation series is performed from $\kappa = 7.5$ down to $\kappa = 4.5$. Along this sequence, we find a N–S transition pressure of $P^*_{\rm NS} = 5.53$ at $\kappa = 5$, which is in good agreement with the value of $P^*_{\rm NS} = 5.47(23)$ obtained from thermodynamic integration. We show in Fig. 5.9 the phase diagram of the HGO model in the pressure-molecular elongation plane. We have also included the I–N coexistence line taken from Ref. [16]. According to our results, the I–N–S triple point is estimated to be located at $\kappa \approx 2.3$. For comparison, we also include data for the nematic-to-solid transition as obtained from Frenkel and Mulder [11] for the related HE

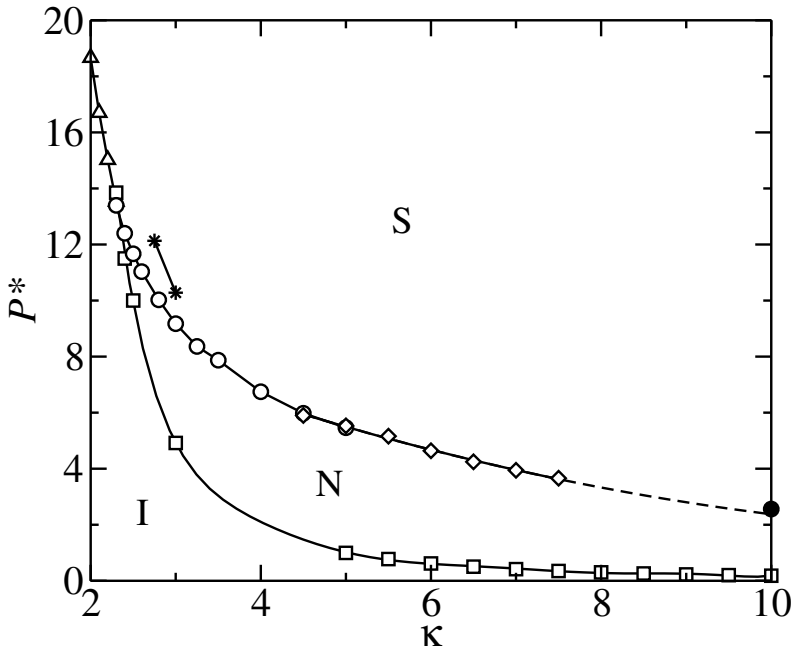

Figure 5.9: The phase diagram of the HGO model in the P^*–κ plane showing the I–N and N–S coexistence lines. The filled circle locates the N–S transition at $\kappa = 10$ as obtained from free energy calculations. The stars correspond to N–S coexistence values obtained by Frenkel and Mulder [11] for the HE model with molecular elongations $\kappa = 2.75$ and 3.

model with molecular elongations $\kappa = 2.75$ and 3. As found for the I–N transition, the N–S transition pressure is seen to be higher in the HE than in the HGO model. The full phase diagram of the HGO model is shown in Fig. 5.10 in the range of molecular elongations $1 \leq \kappa \leq 10$. As expected, the behaviour is similar to that exhibited by the HE model. A crystal phase is stable at high pressures. For hard spheres, the stable crystalline structure is known to correspond to an ABC stacking of the dense molecular planes. According to our results, it seems that a small degree of non-sphericity is sufficient to promote the stability of the AB stacking at high pressure. Upon expansion from high pressure, the solid undergoes a structural transition involving an AB-to-ABC restacking of the molecular planes. This transition is found to be first order and accompanied by a very small density discontinuity. The difference in free energy between these two structures is correspondingly small at the transition. For small molecular anisotropies, the ABC solid undergoes a further transition involving an orientational melting. The translational order, as well as the structure, is preserved in the low-pressure plastic solid phase. The stability of this phase is limited to the range $\kappa \leq 1.43$. For larger

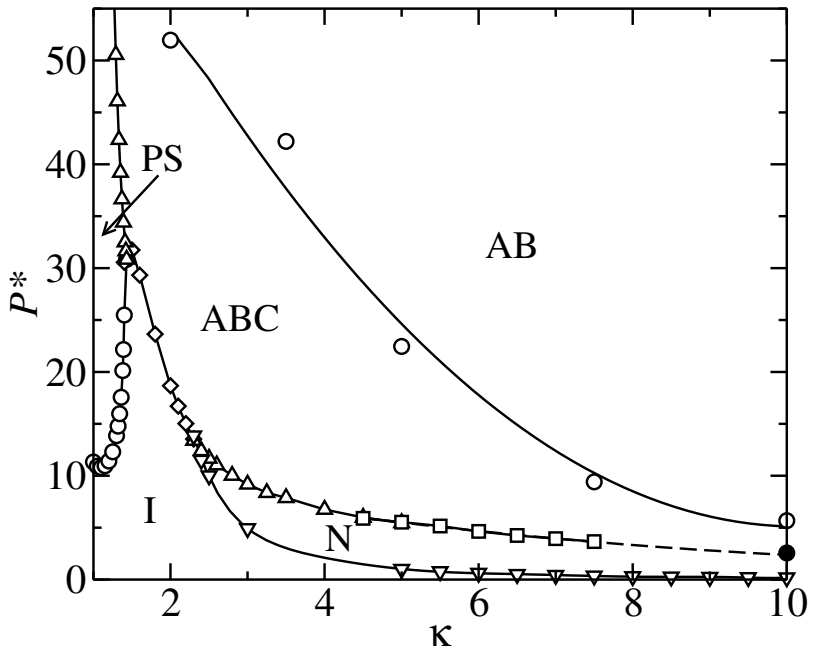

Figure 5.10: The phase diagram of the HGO model in the P^*–κ plane. The filled circle locates the N–S transition at $\kappa = 10$ as obtained from free energy calculations.

molecular anisotropies, the ABC crystal melts directly into a fluid phase. The nature of this fluid phase depends on the molecular elongation. It is a usual (orientationally disordered) molecular fluid phase if $\kappa \leq 2.3$, and nematic for larger elongations. These two particular values of the molecular elongation define the location of the I–PS–S ($\kappa = 1.43$) and I–N–S ($\kappa = 2.3$) triple points.

5.6 Conclusions

It was concluded in the previous chapter that the phase diagram of the HGO model includes regions of stability of I, PS, and S phases for small molecular elongations in the range $\kappa \leq 2$. The PS phase was found to be stable for $\kappa \leq 1.43(1)$, while for larger values of κ, the solid phase was found to melt directly into an isotropic fluid. In the present chapter we have shown that the HGO model exhibits a nematic phase between the I and S phases for molecular elongations $\kappa \geq 2.3$. The main goal in this chapter has been to investigate the nematic-solid transition in this range. We have first determined the equations of state at appropriate values of

the molecular elongation from MC simulation in the NPT ensemble. The corresponding N–S transitions have then been located from the computation of the free energy of each phase, using for this purpose different techniques. Two possible crystalline structures, with ABC and AB stacking, have been considered for the solid phase. The relative stability of these structures has been investigated. We have found that the difference in free energy between these two structures is small, as expected. The AB structure is stable at high pressure and the ABC structure turns more stable at lower pressures, where the melting to the nematic phase takes place. Finally, the N–S coexistence line has been traced out for different values of the molecular elongation in the range of interest by using the Gibbs-Duhem method.

A nematic phase has been previously reported in simulation studies of closely related hard-core systems of HEs, and HSCs. However, there are significant quantitative and qualitative differences among these models whenever the molecules become increasingly non-spherical. Frenkel and Mulder [11] report that the nematic phase becomes stable for elongations larger than $\kappa \approx 2.75$ for a system of HEs; by contrast, significantly larger elongations ($\kappa \geq 4.7$) are required to stabilize the nematic phase in a system of HSCs. Moreover, this phase is preempted by the onset of smectic-like ordering for elongations $\kappa \geq 4.1$. This is in sharp contrast with the phase behaviour of the HE and HGO models, for which no smectic phase has ever been reported. According to theoretical predictions of Holyst and Poniewerski [102], a system of HCs will exhibit nematic behaviour at all values of the molecular elongation.

According to the above discussion, it becomes apparent that not only the molecular elongation, but also the molecular shape is a relevant molecular parameter that determine the phase behaviour of hard-core models. This is to be compared with the conclusion of the previous chapter, where the molecular shape was quoted to play a secondary role for small molecular elongations. Finally, the results included in this chapter emphasize even more the similarities (as well as the differences) between the HE and HGO models.

Chapter 6

HGO model with attractive interactions

A computer simulation study of a thermotropic liquid crystal model appropriate for elongated molecules is presented in this chapter. The repulsive interactions are represented by the HGO model, already described in previous chapters, while the attractive interactions are modelled by a spherically symmetric square well. This model will be referred to hereafter as the HGOSW model. This model reduces to the HGO model when the attractive interactions are turned off. For the particular set of molecular parameters considered here, the HGOSW model is found to exhibit isotropic fluid, nematic, smectic, and solid phases depending on the thermodynamic conditions. We find that the nematic range increases with increasing temperature. However, the smectic phase only appears to be stable over a limited region in the phase diagram.

It should be stressed that, according to the results described in the preceding chapters, the HGOSW model does not give rise to smectic behaviour in the absence of attractive interactions. Though the model includes the attractive interactions at a very basic level, we hope to assess the relative importance of the attractive interactions in stabilizing liquid crystal phases.

6.1 Introduction

It was argued for some time that attractive interactions were the only responsible for the formation of the smectic phase. This was probably based on the fact that most smectics in Nature are strongly polar. This view was reinforced by one of the first molecular theories due to McMillan [104]. This is an extension of the successful Maier-Saupe theory of nematics to include

a description of the positional ordering that characterizes the smectic phase. McMillan's theory neglects repulsive interactions and therefore arrives to the conclusion that the formation of the smectic phase is exclusively due to anisotropic attractive interactions. One of the most salient features of McMillan's theory is that the nematic-to-smectic transition is predicted to be either first order or continuous depending on the temperature and model parameters. Though McMillan's theory makes a number of numerical approximations, we have recently shown that a full version of the theory leads to similar conclusions [105]. We should mention that phase diagrams qualitatively similar to those emerging from McMillan's theory have been reported in experiments [106].

On the other hand, computer simulation studies of hard-core molecular models performed in the mid 80s, had clearly demonstrated that systems with purely repulsive interactions are able to stabilize the nematic phase. The seminal work by Frenkel and Mulder [11] on simulation of HEs gave way to a renewed interest on liquid crystals, particularly in the theoretical community. Though a certain degree of non-sphericity was seen to be required to stabilize the nematic phase,[1] it soon became clear that the particular molecular shape also played an important role. Simulation of freely rotating HSCs [70, 95, 96, 101] demonstrated that the smectic phase can be stabilized in systems characterized by purely repulsive interactions. The full phase diagram of the HSC model was determined by Bolhuis *et al.* [70], who stablished that the smectic phase becomes stable for molecular elongations $\kappa \geq 4.1$; in addition, the nature of the nematic-to-smectic transition was found to change from first order to continuous at $\kappa \approx 6$ (tricritical point). These observations were the starting point of a number of theoretical investigations (mostly based on a density functional approach) that attempt to understand the nematic-smectic transition in terms of excluded-volume effects [107–112].

Molecular models that include anisotropic repulsions as well as attractive interactions have also been considered for the investigation of liquid crystals, the Gay-Berne model [86] probably being one of the most succesful [97–100]. However, the attractive and repulsive contributions in the model can not be separated in a simple way. As a result, it is not straightforward to understand what effects should be ascribed to one or the other of the contributions. Related molecular models consider a hard core with ellipsoidal or spherocylindrical shape embedded in a spherical square well [113–119] (these are sometimes known as "convex-peg" models). The range of the attractive

[1] So far, no smectic phase has ever been reported for a system of HEs. Though this observation is not theoretically forbidden, it seems very unlikely that a smectic phase is stable in such a system.

interactions λ in these models is always taken to be $\lambda \geq L$, with L being the long molecular axis. In spite of their simplicity, these models split the repulsive and attractive contributions of the interactions in a natural way. Tjipto-Margo and Evans [113] have incorporated the convex-peg model into a van der Waals theory and determined the global phase diagram, which is characterized by nematic-vapour, nematic-isotropic and vapour-isotropic coexistence. This model has also been considered by Williamson [115] in a perturbation theory, finding good agreement with Gibbs ensemble simulation data of de Miguel and Allen [120]. No smectic phase has been reported for these models.

A recent study of a thermotropic model consisting of parallel hard ellipsoids with square-well attractive interactions has been undertaken by del Río and de Miguel [13]. At variance with the previously considered convex-peg models, these authors consider shorter attractive ranges $D \leq \lambda \leq L$ They use a density functional theory in which the hard-core contributions to the free energy functional are treated within a non-local weighted density approximation and the attractive contributions are considered at a mean-field level. The smectic phase is predicted to be stable for sufficiently large values of the range of the attractive interactions. The nematic-to-smectic transition is found to be first order at low temperatures and continuous at high temperatures. Also, the range of the smectic phase is seen to decrease with increasing pressure. No smectic phase is predicted if the pressure is too large or the attractive range is made too large. These results highlight the importance of the attractive interactions in stabilizing the smectic phase.

6.2 Model potential

We consider a system of N axially symmetric molecules characterized by pair interactions of the form

$$u(\mathbf{r}) = u_{\text{rep}}(\mathbf{r}) + u_{\text{att}}(\mathbf{r})$$

where $\mathbf{r}$ is the intermolecular vector. $u(\mathbf{r})_{\text{rep}}$ and $u(\mathbf{r})_{\text{att}}$ represent the repulsive and attractive interaction energy, respectively. A schematic representation of the model is given in Fig. 6.1. The repulsive part is represented by the HGO model, already described in chapter 4. The explicit expression of the repulsive pair interactions is

$$u_{\text{rep}}(\mathbf{r}) = \begin{cases} \infty & \text{if } r \leq \sigma(\hat{\mathbf{r}}, \hat{\mathbf{u}}_i, \hat{\mathbf{u}}_j)\,, \\ 0 & \text{if } r > \sigma(\hat{\mathbf{r}}, \hat{\mathbf{u}}_i, \hat{\mathbf{u}}_j)\,, \end{cases} \tag{6.1}$$

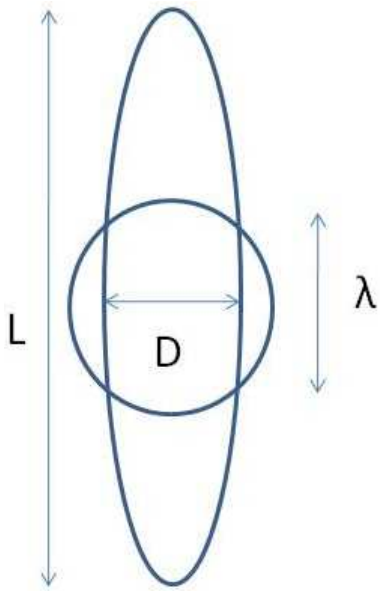

Figure 6.1: Schematic representation of the HGOSW model.

where $\sigma(\hat{\mathbf{r}}, \hat{\mathbf{u}}_i, \hat{\mathbf{u}}_j)$ is the distance of closest approach between a pair of molecules, which was defined in chapter 4 [c.f. Eq. (4.3)].

The attractive interactions are modelled by a spherically symmetric square well

$$u_{att}(\mathbf{r}) = \begin{cases} -\varepsilon & \text{if } \sigma(\hat{\mathbf{r}}, \hat{\mathbf{u}}_\mathbf{i}, \hat{\mathbf{u}}_\mathbf{j}) < r < \lambda\,, \\ 0 & \text{if } r \geq \lambda\,, \end{cases} \tag{6.2}$$

where λ is the range of the attractive interactions, and ε represents the strength of the attractive interactions, which sets a natural energy scale of the interactions. As a consequence, and at variance with the HGO model, the temperature will become a relevant thermodynamic parameter that enters into the description of the phase behaviour of the HGOSW model. Considering that D is the minimum distance between a pair molecules, the range of the attractive interactions is subject to the constraint $\lambda > D$.

We limit ourselves to model parameters $\kappa = 5$, and $\lambda/D = 1.5$. For comparison, we recall that in the absence of attractive interactions, the system shows isotropic, nematic, and solid phases depending on the value of the pressure: the I–N transition takes place at $\beta P D^3 = 0.996$, and the N–S transition occurs at $\beta P D^3 = 5.47(23)$.

6.3 Simulation details

6.3.1 Generalities

All the simulations are performed in the NPT ensemble. The Metropolis algorithm used to sample this ensemble was described in §2.2.3. This sampling involves translational, rotational, and volume moves. Depending on the nature of the phase, we use different algorithms to sample the volume according to the input pressure. We use LVOL1 for the isotropic and nematic phases, LVOL2 for the smectic phase, and LVOL3 for the solid phase. The corresponding acceptance probabilities for the volume moves are given in Eqs. (2.17) and (2.19). The algorithm is essentially the same as the one used for the simulation of HGO systems, the main difference being that the temperature enters explicitly into the probability of generating microstates.

We consider systems consisting of $N = 1008$ HGOSW molecules with $\kappa = 5$ and $\lambda/D = 1.5$. The phase behaviour of the HGOSW model has been explored by changing the pressure along a constant-temperature path. For each isotherm, a low-density isotropic configuration is first equilibrated and subsequently compressed up to high pressures. A second sequence of simulations is started at high pressure where the solid phase is expected to be thermodynamically stable. The initial solid configuration is generated from an ideal lattice consisting of 6 layers, each with 12×14 molecules, parallel to the x-y plane of the simulation box with in-layer hexagonal order of the molecular centers of mass. The layers are stacked along the z axis following an ABC pattern. No simulations have been performed for other crystalline structures. After equilibration, the initial crystalline configuration is slowly expanded at constant temperature. A number of simulations along constant-pressure paths has also been considered. In this case, simulations are started from a crystalline structure at low temperature, and the system is subsequently heated at constant pressure in small jumps in temperature.

The simulations are organized in cycles, each cycle consisting of N attempts to translate the molecules, N rotational attempts, and several volume moves depending on the particular phase. At any input pressure and temperature, the system is first allowed to equilibrate for at least 2×10^5 cycles, followed by a further stage of 2×10^5 cycles where properties of interest are monitored, including the number density, configurational energy, enthalpy, and order parameters.

All quantities are reported in reduced (dimensionless) units, using D and ε as the length and energy scales. Explicitly, we define the reduced pressure, $P^* = PD^3/\varepsilon$; temperature, $T^* = k_{\mathrm{B}}T/\varepsilon$; number density, $\rho^* = \rho D^3$;

configurational energy per particle, $u^* = U/(N\varepsilon)$; and enthalpy per particle, $h^* = H/(N\varepsilon)$. The reduced range of the attractive interactions is defined as $\lambda^* = \lambda/D$.

6.3.2 Order parameters

The HGOSW model is expected to exhibit orientational order at appropriate thermodynamic conditions. The onset of orientational order is analyzed in terms of the orientational order parameter S defined in Eq. (4.4). Monitoring S will allow us to determine whether the isotropic phase ($S \approx 0$) turns into an orientationally ordered phase ($S \neq 0$).

An additional order parameter must be defined to characterize the smectic phase.[2] In addition to the orientational order, this phase exhibits a layered structure with no in-plane positional order of the molecular centers of mass. The smectic layers are perpendicular to the director (average direction of molecular alignment). There is no unique definition for the smectic order parameter. Our definition is based on the fact that the smectic phase is characterized by a density modulation along the director. This density wave can be characterized by a translational order parameter $\tau(q)$ defined as

$$\tau(q) = \mid \langle \exp(iqr_{\parallel}) \rangle \mid , \tag{6.3}$$

where $q = 2\pi/d$ is the wavevector associated with the wave modulation, with d being its spatial periodicity (i.e., the spacing between consecutive smectic layers). $r_{\parallel}$ in Eq. (6.3) corresponds to the projection of the intermolecular vector onto the director. The angular brackets involve an ensemble average, as well as an average over all molecular pairs of the system. The main problem with expression (6.3) is that d is not known beforehand. This is avoided by calculating $\tau(q)$ for a set of values of q (we typically use 50 values of q). If $q_{\max}$ is the value of q that maximizes (6.3), the smectic order parameter, τ, is defined as $\tau = \tau(q_{\max})$; the associated value $d_{\max} = 2\pi/q_{\max}$ corresponds to the smectic spacing. This definition ensures that $\tau = 1$ for a perfectly layered phase along the director, and $\tau = 0$ in the absence of translational order along the director.

One should note that the smectic order parameter τ allows one to discriminate between nematic and smectic behaviour, but does not distinguish between the smectic and solid phases (both phases are characterized by a

[2]There are many types of smectic phases which differ in a number of subtleties. We are describing here the simplest smectic phase, which is denoted as SmA. Additional order parameters are required to characterize other smectic phases.

density modulation along the director). For this purpose, we monitor the bond orientational order parameter Ψ_6 defined in Eq. (4.6). Values of Ψ_6 close to one are appropriate for a solid with hexagonal in-plane order, while values of $\Psi_6 \approx 0$ are the signature of the SmA phase (no in-plane translational order). We also keep track of the order parameter $(\Psi_6)^l$, defined in Eq. (4.5), in order to check for possible partial (incomplete) melting of the crystalline layers.

6.4 Isotherm $T^* = 2$

Two series of NPT simulations are performed in order to investigate the phase behaviour of the HGOSW model with parameters $\kappa = 5$ and $\lambda^* = 1.5$ along the isotherm $T^* = 2$. One series is started from a low-density isotropic configuration equilibrated at a pressure of $P^* = 0.05$. A second series is started from a crystalline configuration equilibrated at a pressure of $P^* = 15$. We next analyze our simulation results.

6.4.1 Isothermal compression

The compression series is started from a random configuration at a pressure of $P^* = 0.05$. The system is found to be orientationally disordered, as expected at such low pressure, with a value of $S = 0.0265(1)$. We show in Fig. 6.2(a) the behaviour of the order parameter S upon isothermal compression of the initial isotropic fluid configuration in small jumps in pressure. The order parameter is seen to undergo a sudden jump at a value of the pressure of $P^* = 1.95$; beyond this pressure, S increases with pressure from a value of $S \approx 0.60$. This is an indication that an orientational disorder-order transition has taken place in the system. The nature of the ordered phase is identified as nematic after noticing that the system does not develop a layered structure along the director, i.e., $\tau \approx 0$ in this region. The isotropic-to-nematic (I–N) transition also shows up as a discontinuity in the pressure vs density representation of the simulation data. This is shown in Fig. 6.2(b). The density change at the transition is small, as expected for a weakly first-order transition. Also as expected, histeresis effects are observed at the I–N transition: when a nematic fluid configuration is slowly expanded from $P^* = 2.30$, the orientational order parameter vanishes at a pressure of $P^* \approx 1.85$. The exact location of the transition pressure requires computation of the free energy of the isotropic and nematic phases. We will come to this point later.

When the nematic phase is further compressed, a new transition seems

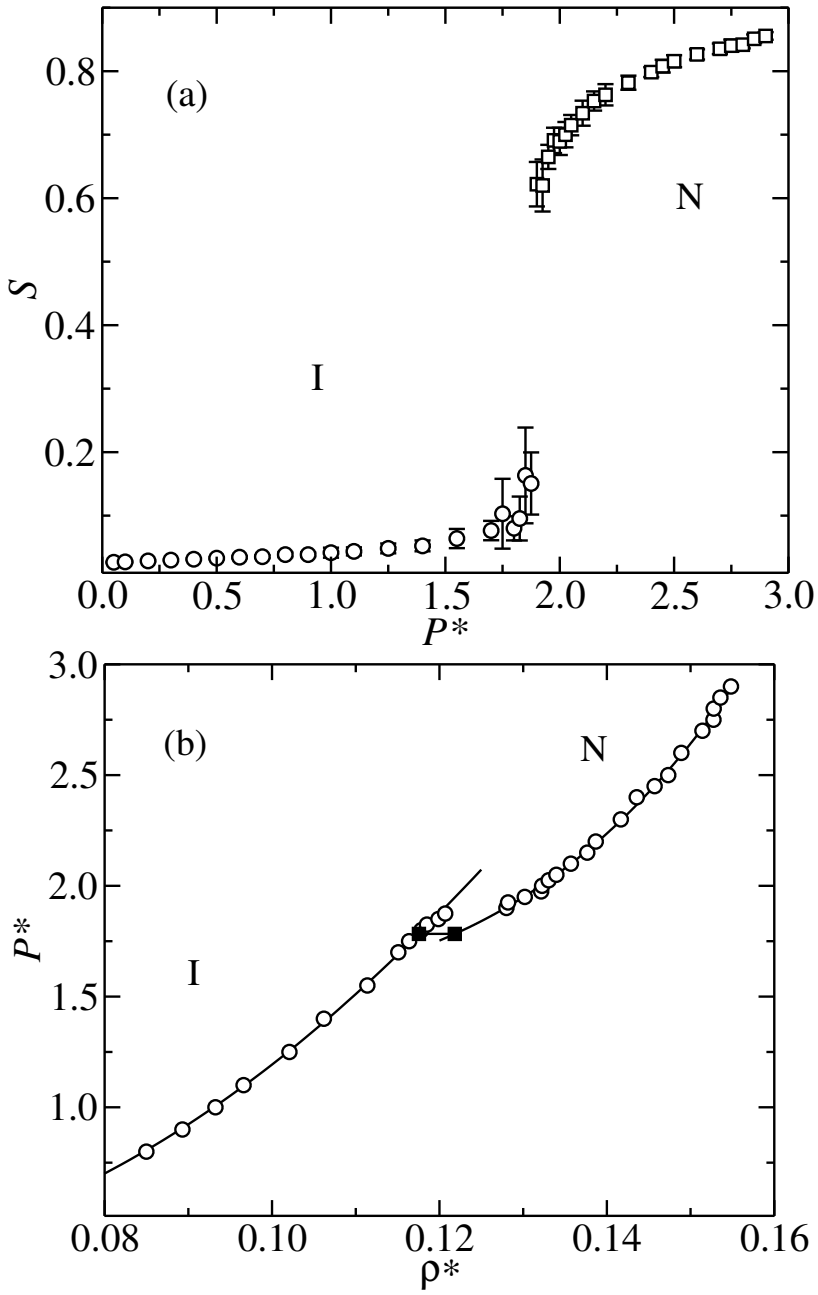

Figure 6.2: (a) Variation of the orientational order parameter S vs pressure P^*, and (b) P^* vs density ρ^* for the HGOSW model with parameters $\kappa = 5$ and $\lambda^* = 1.5$ at temperature $T^* = 2$ in the I and N regions. Continuous lines are fits to the simulation data. Filled squares indicate the location of the I–N transition.

to take place at about $P^* \approx 2.90$. The variation of the pressure with density upon compression in this region is shown in Fig. 6.3(a). The signature of this transition is a discontinuity in the slope of the equation of state, which becomes evident in the scale of the figure. The behaviour of the smectic order parameter τ in this region is shown in Fig. 6.3(b). This indicates that the nematic phase gives way to a layered structure at $P^* \approx 2.90$. The bond-orientational order (not shown in the plot) is seen to be $\Psi_6 \approx 0$ in the high-pressure side of the transition. We therefore conclude that the nematic phase develops smectic ordering upon compression.

According to our simulation data, we are not able to find a measurable density change at the N–SmA transition.[3] In addition, our simulation results obtained along the expansion series (to be discussed later) do not show any (measurable) sign of histeresis about the N–SmA transition. Thus, the transition appears to occur in a continuous way. The approximately continuous behaviour of τ in the transition region [see Fig. 6.3(b)] seems to support our conclusion. From our simulation results, the N–SmA transition takes place at $P^* = 2.90(2)$, $\rho^* = 0.15482(23)$. We also note that no change in the orientational order parameter S is detected at the N–SmA transition.

We now proceed to the computation of the free energy of the isotropic and nematic phases in order to locate the I–N transition. Thermodynamic integration is used to calculate the absolute Helmhotlz free energy of the isotropic phase at an arbitrary density. Referring to Eq. (2.47),

$$f\left(\rho^*\right) = \ln \rho^* - 1 + \int_0^{\rho^*} \left[Z(\rho^{*\prime}) - 1\right] \frac{d\rho^{*\prime}}{\rho^{*\prime}} \,. \tag{6.4}$$

A total of 21 state points in the range of pressures $0.05 \leq P^* \leq 1.875$ is used to fit the simulation values of Z in the isotropic branch to a polynominal in ρ^* of the form

$$Z\left(\rho^*\right) = \sum_{i=1}^{m} a_i (\rho^*)^{i-1}$$

In order to reproduce the low-density limit of Z, we set $a_1 = 1$ and determine the rest of coefficients from a linear least-square method [24]. The fitting coefficients are given in Table 6.1.

We are assuming in Eq. (6.4) that the reference state is the ideal-gas state. As explained elsewhere in this work, this choice is not appropriate for the nematic phase. Our calculation of $f_{\rm ref}$ at a nematic reference state $\rho^*_{\rm ref}$ involves

[3] If there were a finite density jump at the N–SmA transition, it would be smaller than ≈ 0.0003, which is the typical error associated with the densities in this region.

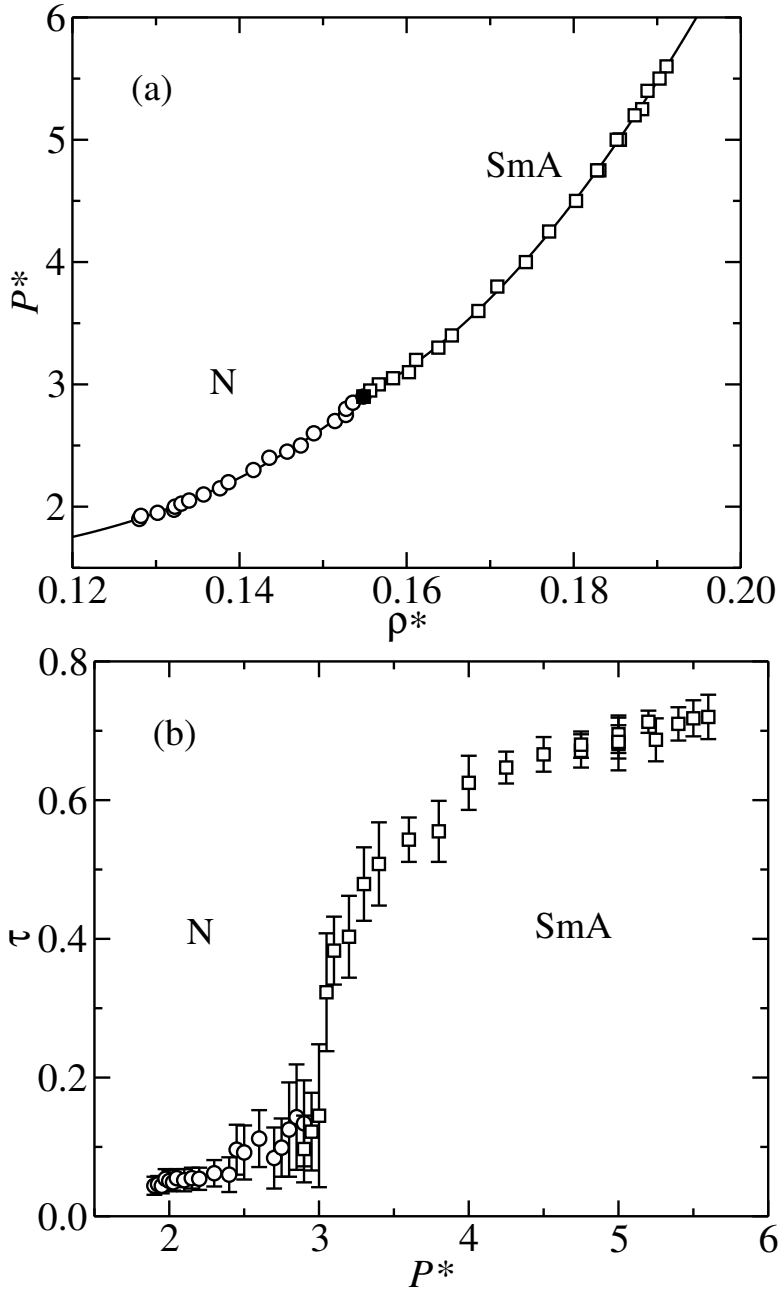

Figure 6.3: (a) Variation of pressure P^* vs density ρ^*, and (b) smectic order parameter τ vs P^* for the HGOSW model with $\kappa = 5$ and $\lambda^* = 1.5$ at temperature $T^* = 2$ in the N and SmA regions. Continuous lines are fits to the simulation data. The filled square indicates the location of the N–SmA transition.

Table 6.1: Fitting coefficients of the simulation data for the compressibility factor Z to a polynomial function of ρ^* for the different phases observed for the HGOSW model at $T^* = 2$.

a_m	isotropic	nematic	smectic A	solid
a_1	1	18.99178	143.59042	−584.447872
a_2	6.10995	−136.55019	−2229.15028	8946.36318
a_3	−9.68480	−199.80886	11639.9234	−45534.4867
a_4	65.04879	4383.47891	−18346.849	78916.766
a_5	−149.74838			

the computation of the change in free energy along the following artificial path: (a) slow application of an external orienting field [see Eq. (2.52)] of intensity λ_c at constant density $\rho^*_{\rm ref}$; (b) expansion of the system at constant T^* and λ_c down to low densities (or pressures). The value of λ_c is chosen so that the low-density state exhibits nematic behaviour in the presence of the external field. For the present application, the choice $\lambda_c = 4\varepsilon$ guarantees that no transition from the nematic phase takes place along the above path.[4] $f_{\rm ref}$ is given by

$$f_{\rm ref} = \ln \rho^*_{\rm ref} - 1 + 1.13945 + \int_0^{\rho^*_{\rm ref}} [Z(\rho^*) - 1] \frac{d\rho^*}{\rho^*} - \frac{1}{N k_{\rm B} T} \int_0^{\lambda_c} d\lambda \left\langle \sum_{i=1}^{N} \sin^2 \theta_i \right\rangle_\lambda , \tag{6.5}$$

where the first line includes the extra (analytical) contribution due to an external field of intensity $\lambda_c = 4\,\varepsilon$ [see Eq. (2.56)]. We choose $\rho^*_{\rm ref} = 0.14584$. The integration of $Z(\rho^*)$ in the presence of the external field is computed by considering a fit of the simulation data (total of 24 state points in the integration range) to a polynomial in ρ^*. We find a similar problem here to the one already discussed in other parts of this work: there is a systematic error in this calculation associated with the particular number of terms considered in the fit. We find a value of 3.061(19), where the error accounts for the systematic error. The final contribution in Eq. (6.5) corresponds to the reversible work when the external field is switched off at constant density $\rho^*_{\rm ref}$; this is computed from a Gaussian quadrature, with a total of 10

[4] The choice of λ_c has to be made with some care. Too large a value of λ_c may promote the formation of a SmA phase somewhere along the path. We have carefully checked that the system does not exhibit a transition to the SmA phase along the artificial path.

Table 6.2: Coexistence properties at the I–N transition of the HGOSW fluid model at $T^* = 2$.

$\rho_{\rm I}^*$	$\rho_{\rm N}^*$	P^*	g
0.11755	0.12183	1.783	8.793

constant-density simulations being performed in the integration range. We find a value of $-0.1986(28)$. Adding up all of the contributions, we obtain $f_{\rm ref} = 2.862(19)$.

Once we have the free energy of the nematic reference state at our disposal, the free energy of the nematic phase at any density ρ^* follows from the usual relation

$$f(\rho^*) = f_{\rm ref} + \int_{\rho_{\rm ref}^*}^{\rho^*} Z(\rho^{*\prime}) \frac{d\rho^{*\prime}}{\rho^{*\prime}} \,. \tag{6.6}$$

The above integration is performed by fitting the values of Z in the nematic branch to a polynomial expression in ρ^*. A total of 20 nematic states have been simulated in the range $1.90 \leq P^* \leq 2.90$. The corresponding coefficients have been collected in Table 6.1. The I–N transition properties are obtained after solving the coexistence conditions

$$\begin{aligned} g(\rho_{\rm I}^*) &= g(\rho_{\rm N}^*) \,, \\ P^*(\rho_{\rm I}^*) &= P^*(\rho_{\rm N}^*) \,, \end{aligned} \tag{6.7}$$

for the coexistence densities $\rho_{\rm I}^*$ and $\rho_{\rm N}^*$, where we have considered the thermodynamic relation $g(\rho^*) = f(\rho^*) + Z(\rho^*)$ for each phase. The corresponding transition properties are gathered in Table 6.2. According to the data included in that table, the I–N transition at $T^* = 2$ is accompanied by a density gap of about 3.5%. This is larger than the values typically found in experiments, but quantitatively similar to the value found in computer simulation of related molecular models.

6.4.2 Isothermal expansion

In principle, one might expect the onset of crystalline order if the SmA phase is compressed up to sufficiently high pressures. However, we have not observed spontaneous freezing of the SmA liquid. In order to investigate the stability of the SmA phase relative to the solid, we start from a crystalline configuration at high pressure and follow the behaviour of the system upon

expansion. This expansion series is started at $P^* = 15$. Details about the initial configuration were given earlier in §6.3.1.

The equation of state (pressure vs density) resulting from the isothermal expansion of the solid phase at $T^* = 2$ is shown in Fig. 6.4(a). No structural transition to a different crystal structure is observed along the simulation series. The solid structure turns mechanically unstable at pressures below $P^* = 5.25$. The nature of the low-pressure phase becomes apparent after analyzing the variation of the order parameters along the expansion series. This is shown in Fig. 6.4(b). Ψ_6 is seen to vanish discontinuously at $P^* = 5.25$; the low-pressure phase exhibits orientational order ($S \approx 0.94$) and also smectic-like order ($\tau \approx 0.70$). According to our data, the solid gives way to a SmA liquid, and the corresponding melting transition is first order. We find that the director does not change orientation across the transition; moreover, it keeps the same (0,0,1) orientation as the SmA is further expanded. The order parameter τ is seen to decrease steadily as the input pressure decreases. Interestingly, we find that smectic ordering is lost (values of $\tau \approx 0$) at the same thermodynamic conditions at which the N–SmA was located in the compression series: no histeresis seems to accompany this transition.

The location of the SmA–S transition requires the calculation of the free energy of each phase. As the N–SmA transition is continuous, one may get the free energy of the SmA phase directly from the free energy of the nematic phase. More explicitly, we write for the SmA phase

$$g(P^*) = g_{\rm ref} + \int_{P^*_{\rm ref}}^{P^*} Z(P^{*\prime})\, \frac{dP^{*\prime}}{P^{*\prime}}\,, \tag{6.8}$$

where the N–SmA transition pressure $P^*_{\rm ref} = 2.9$ is chosen as reference state. The free energy at this pressure is obtained from the corresponding nematic expression given in Eq. (6.6). Data from 23 constant-pressure simulations in the range $2.9 \leq P^* \leq 5.6$ are used to fit the compressibility factor of the SmA phase to a polynomial in P^*. The fitting coefficients are given in Table 6.1.

$P^* = 12$ is selected as the reference state for the solid phase. The EC method is used to compute the free energy at this pressure. Owing to the presence of the attractive interactions, the practical implementation of the method differs slightly from the way it was used in previous chapters for the HGO model. An schematic representation of the integration path that links the target solid with the ideal EC is depicted in Fig. 6.5.

One starts from the non-interacting EC with the same structure as the target equilibrium solid, and with fixed center of mass. We recall that this state is parametrically defined in terms of a single parameter ξ, such that the

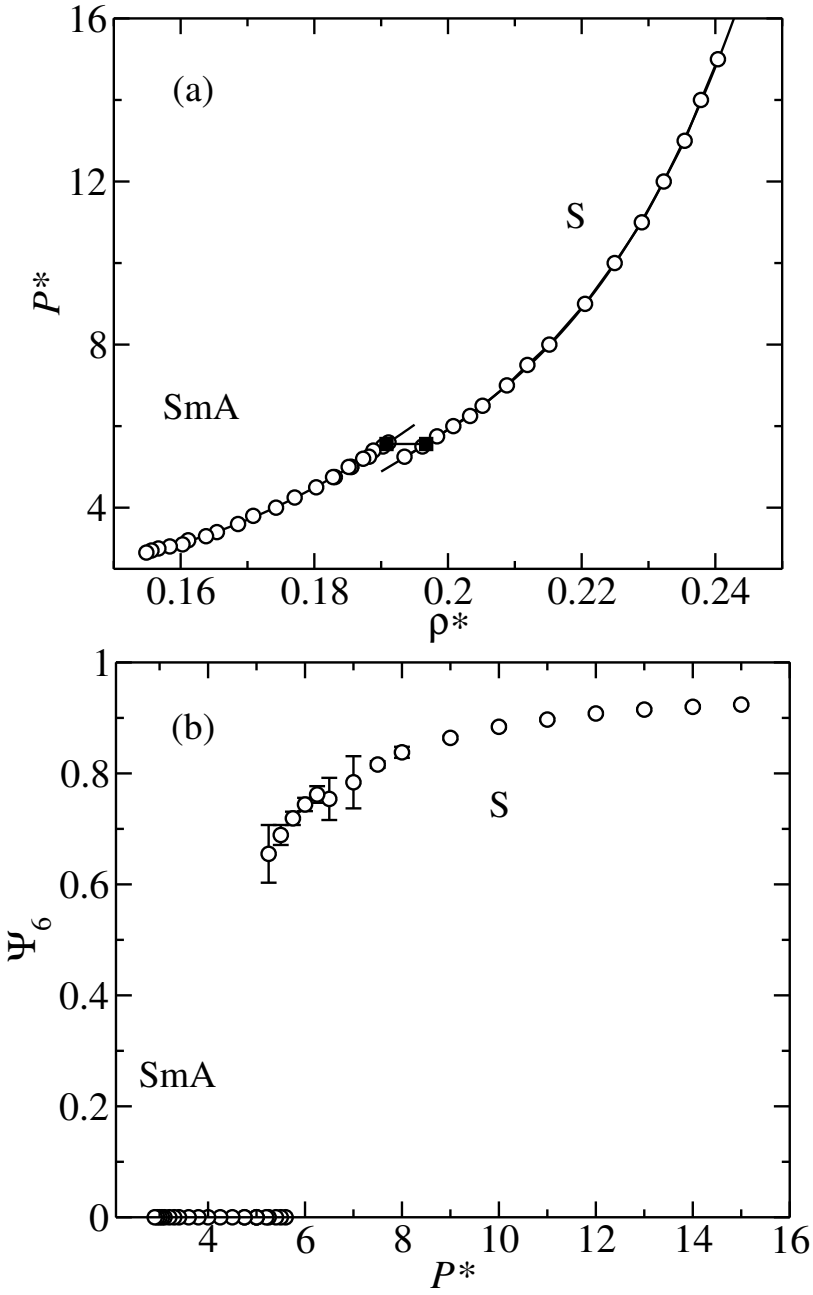

Figure 6.4: (a) P^* vs density ρ^* for a system of HGOSW molecules with model parameters $\kappa = 5$ and $\lambda^* = 1.5$ at temperature $T^* = 2$. Continuous lines are fits to the simulation data. Filled squares indicate the SmA-S transition. (b) Variation of the bond orientational order Ψ_6 with pressure.

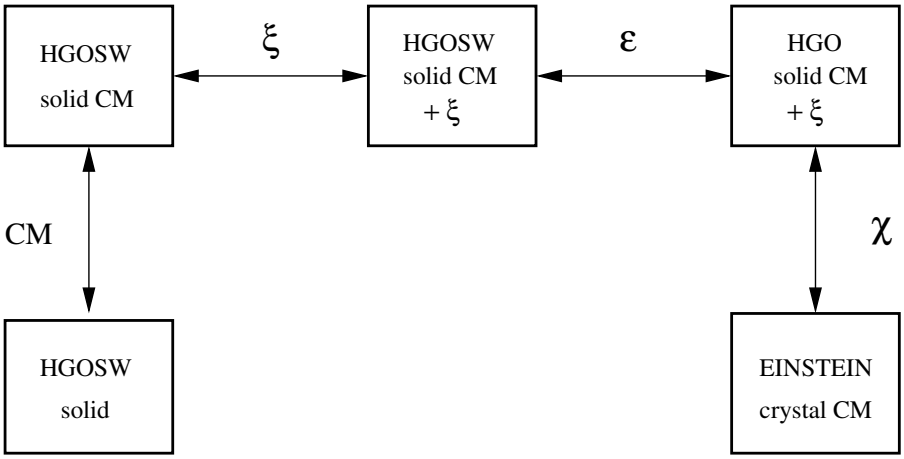

Figure 6.5: Schematic representation of the integration path that links the HGOSW solid with a non-interacting EC with fixed center of mass (reference state).

translational and rotational couplings are written as $\lambda_t = \xi$ and $\lambda_r = 10\xi$, respectively. The thermodynamic path involves the following steps:

1. Connecting the hard-core interactions (parameter χ). The corresponding free energy difference Δf_χ is calculated in an expanded ensemble simulation, as done in previous chapters for the HGO solid.

2. Switching on the attractive interactions (parameter ε). The free energy difference Δf_ε is computed from parametric integration, using ε as the integration parameter. As shown next, this contribution can be considered analytical for the present application.

3. Switching off the translational and rotational couplings (parameter ξ). The free energy difference Δf_ξ is computed from parametric integration, with ξ being the integration parameter. This contribution is calculated from a 10-point Gaussian quadrature.

4. Correcting for having fixed the center of mass. The corresponding contribution $\Delta f^{\rm CM}$ is analytical [see Eq.(2.61)].

When comparing with the implementation of the EC method for the HGO solid, the only new contribution involves Δf_ε. We define the (dimensionless) energy parameter $\varepsilon^* = \varepsilon/(k_{\rm B}T)$.[5] Using parametric integration (see §2.3.1),

[5] ε^* is nothing else but the inverse of the reduced temperature, $\varepsilon^* = 1/T^*$. This parameter is introduced for convenience.

one can write for the Helmholtz free energy

$$F(\varepsilon^*) = F(0) + \int_0^{\varepsilon^*} d\varepsilon^{*\prime} \left(\frac{\partial F}{\partial \varepsilon^{*\prime}} \right) .$$

The above derivative is taken at constant density and keeping fixed the rest of parameters upon which the interaction potential $\mathcal{U}$ may depend. Using the fundamental relation $F = -k_{\rm B}T \ln Q$, it is straightforward to arrive to

$$\Delta f_\varepsilon \equiv f(\varepsilon^*) - f(0) = \int_0^{\varepsilon^*} d\varepsilon^* \langle u^* \rangle \,, \tag{6.9}$$

where, as usual, $f = F/(Nk_{\rm B}T)$, and $u^* = U/(N\varepsilon)$ is the reduced energy per particle. The angular brackets denote an ensemble average at fixed ε^*.[6] In principle, the integrand in Eq. (6.9) depends on ε^*. However, $\langle u^* \rangle$ is not expected to change if one recalls that the attractive interactions are switched on for the interacting EC system. Using n to denote the number of molecules that are within the range λ of the attractive interactions from any arbitrary molecule of the system, one should expect $U \equiv \langle \mathcal{U} \rangle = (-n/2)N\varepsilon$. As discussed above, the reduded energy $\langle u^* \rangle = -n/2$ must remain constant along the integration path, which allows us to express Eq. (6.9) as

$$\Delta f_\varepsilon = -(n/2)\varepsilon^* \,.$$

For the present application, where the attractive interactions are short ranged with $\lambda^* = 1.5$, it is easy to realize that $n = 6$.

Finally the free energy of the reference solid state point can be expressed as:

$$f = f_{\rm EC}^{\rm CM} + \Delta f_\varepsilon^{\rm CM} + \Delta f_\chi^{\rm CM} + \Delta f_\xi^{\rm CM} + \Delta f^{\rm CM} \,.$$

$\Delta f_\xi^{\rm CM}$ is calculated from a 10-point Gaussian quadrature. We show in Fig. 6.6 the variation of the integrand in $\Delta f_\xi^{\rm CM}$ with the variable u defined in Eq. (4.12) as obtained from NVT simulation. $\Delta f_\chi^{\rm CM}$ is calculated in an expanded ensemble simulation consisting of 5×10^4 cycles for equilibration and 5×10^5 cycles for accumulating run averages.

The contributions to the free energy of the reference solid state point are given in Table 6.3. By solving the coexistence conditions we obtain the coexistence properties at the S–SmA transition. In Table 6.4 we give the corresponding coexistence values.

[6] This expression is fully equivalent to the expression that gives the free energy difference between two states at different temperatures linked by a constant-density path [see for example Eq. (2.65) in Allen and Tildesley [4]].

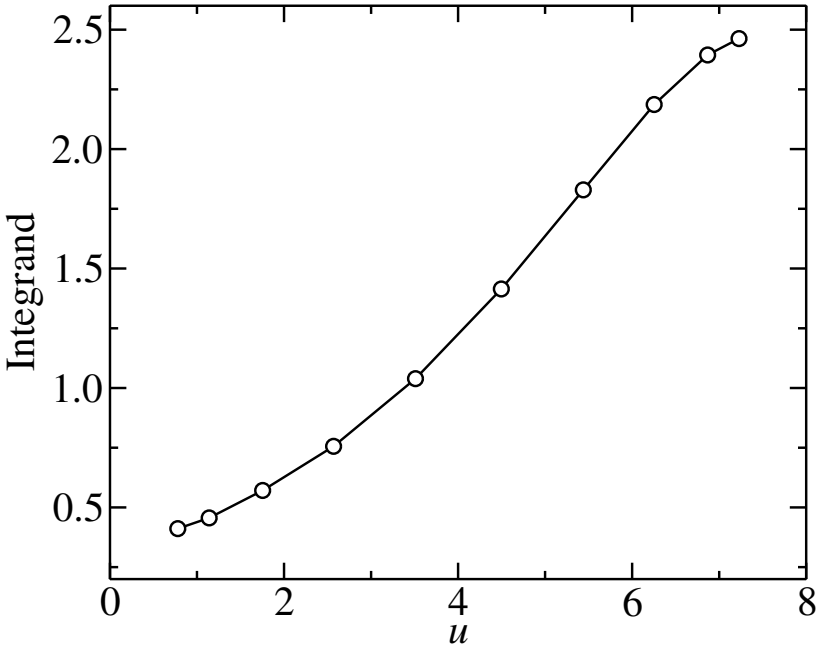

Figure 6.6: Variation of the integrand with the integration variable u in the 10-point Gaussian quadrature for the computation of $\Delta f_\xi^{\mathrm{CM}}$ for the HGOSW solid. The line is a guide to the eye. Error bars are smaller than the size of the symbols.

Table 6.3: Contributions to the free energy of a HGOSW solid at $P^*_{\mathrm{ref}} = 12$ and $T^* = 2.0$. $f_{\mathrm{EC}}^{\mathrm{CM}}$ is the free energy of the ideal EC with fixed center of mass, and coupling constants $\lambda_t = 1500\varepsilon$ and $\lambda_r = 10\lambda_t$. The meaning of each term is given in the main text.

λ_t	$f_{\mathrm{EC}}^{\mathrm{CM}}$	$\Delta f_\chi^{\mathrm{CM}}$	$\Delta f_\xi^{\mathrm{CM}}$	Δf^{CM}	Δf_ϵ	f_{ref}
1500	19.5525	0.00626	−8.7495(75)	−0.0117	−1.5	9.2976(75)

Table 6.4: Coexistence values at the S–SmA transition of a system of HGOSW molecules with $\kappa = 5$, and $\lambda^* = 1.5$ at $T^* = 2$.

ρ_{A}^*	ρ_{S}^*	P^*	g
0.19079	0.19674	5.562	20.355

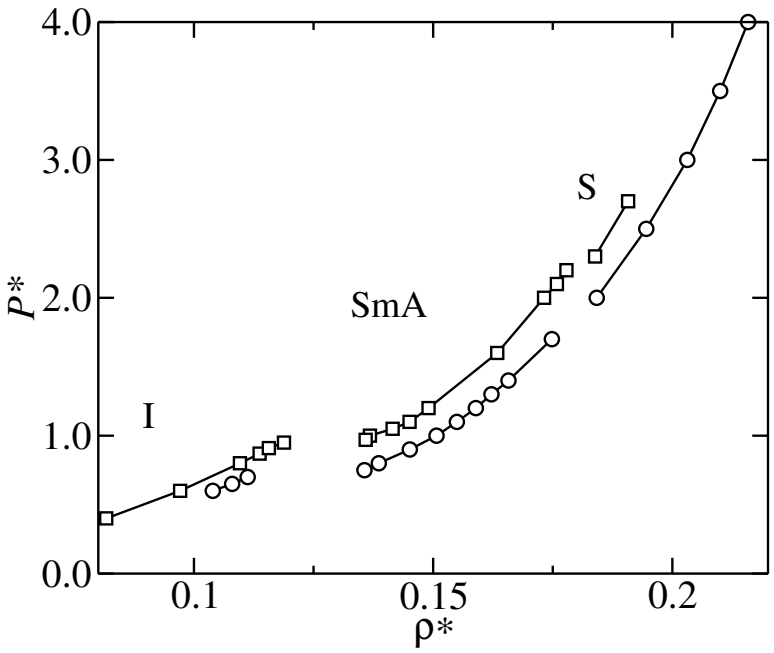

Figure 6.7: Pressure P^* vs density ρ^* at temperatures $T^* = 1$ (circles) and $T^* = 1.15$ (squares). Pressure is expressed in units of $P^* = PD^3/\epsilon$, the density $\rho^* = \rho D^3$, and the temperature $T^* = k_{\rm B}T/\epsilon$. The error bars are smaller than the size of the symbols. The solid lines are a guide to the eye.

6.5 Other isotherms

In Fig. 6.7 we present the simulation results along the isotherms $T^* = 1$ and 1.15. The equation of state (P^* vs ρ^*) at temperature $T^* = 1$ is determined by expanding the system from a solid configuration at $P^* = 4$ down to pressure $P^* = 0.60$. The solid structure turns mechanically unstable at $P^* = 1.75$ and gives way to a smectic-like phase. The bond orientational order parameter Ψ_6 is seen to vanish discontinuously at this pressure, as shown in Fig. 6.8. On further expanding the system, the smectic ordering turns unstable at $P^* = 0.70$. Below this pressure, both S and τ are approximately zero, which indicates that the low-pressure phase is an isotropic fluid (see Fig. 6.8). At variance with the results included in the preceding section, no nematic phase is observed when the SmA is expandend isothermically at low temperature.

The behaviour of the system at $T^* = 1.15$ is seen to be very similar to that observed at $T^* = 1$. The simulation series is started from a solid configuration at $P^* = 2.70$. The solid phase is seen to become mechanically unstable at $P^* = 2.30$. Below this pressure, the system develops smectic-like ordering. When the smectic phase is further expanded, a melting transition is

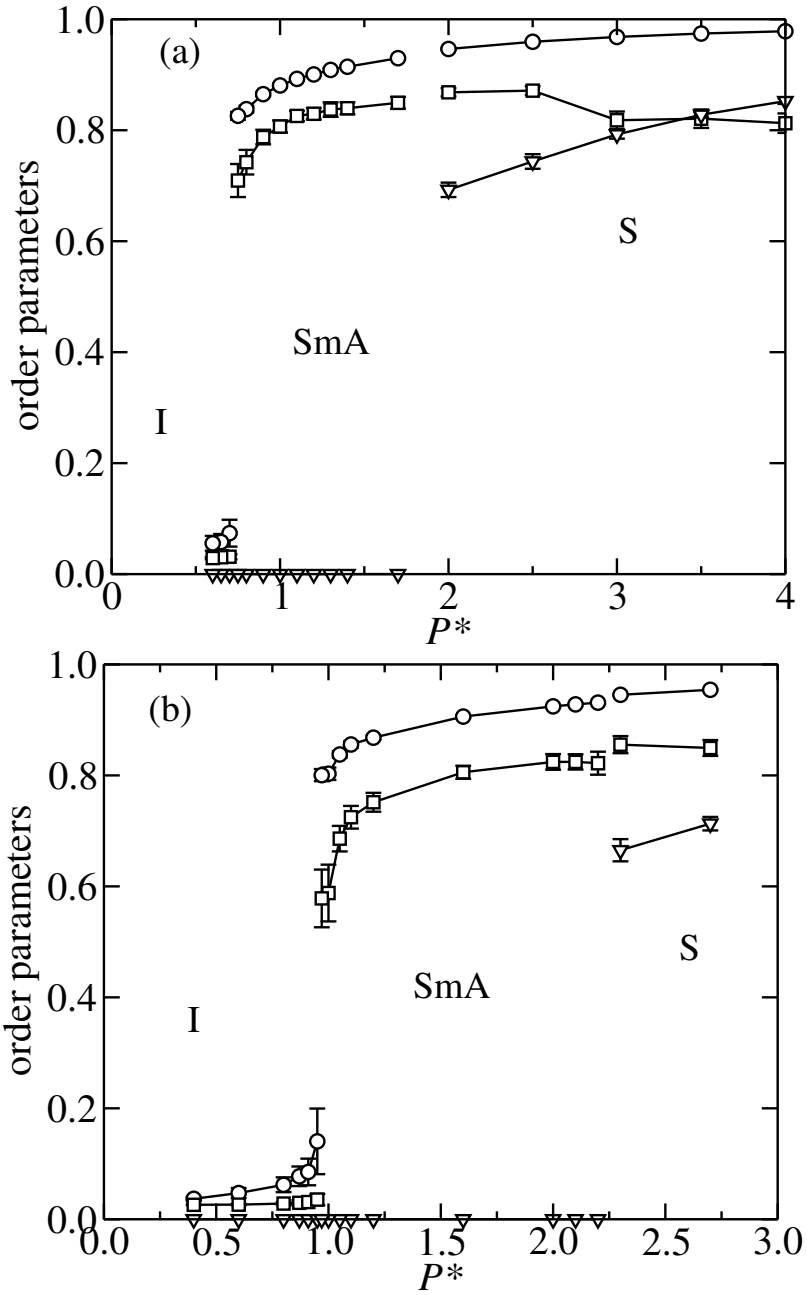

Figure 6.8: Variation of the orientational order parameter S (circles), positional order parameter τ (squares), and bond orientational order Ψ_6 (triangles) vs pressure P^* along the isotherms (a) $T^* = 1$, and (b) $T^* = 1.15$. The solid lines are a guide to the eye.

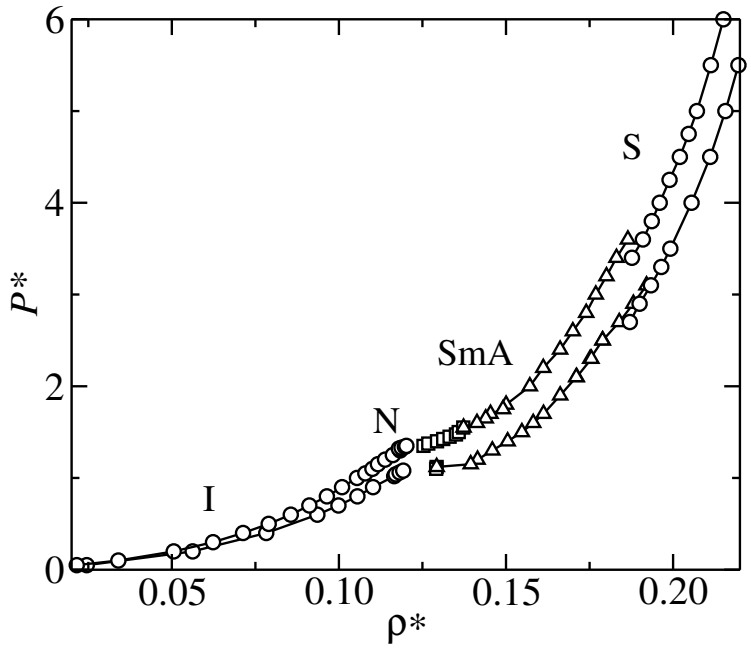

Figure 6.9: Pressure P^* vs density ρ^* at temperatures $T^* = 1.25$ (lower curve) and $T^* = 1.5$ (upper curve). Pressure is expressed in units of $P^* = PD^3/\epsilon$, the density $\rho^* = \rho D^3$, and the temperature $T^* = k_{\rm B}T/\epsilon$. Solid lines are a guide to the eye. The error bars are smaller than the size of the symbols.

observed to occur at $P^* = 0.97$, the low-pressure phase being identified once again as an isotropic fluid. We show in Fig. 6.8 the corresponding variation of the order parameters with pressure.

The equations of state at slightly higher temperatures, $T^* = 1.25$ and $T^* = 1.5$, are presented in Fig. 6.9. At these temperatures the nematic phase becomes stable between the isotropic and smectic phases. The equation of state along the isotherm $T^* = 1.25$ is obtained from expansion of a solid configuration at pressure $P^* = 6$ down to pressure $P^* = 1.06$. The solid phase becomes unstable at $P^* = 2.70$, giving way to a SmA fluid. The system keeps a layered structure down to a value of the pressure of $P^* = 1.15$. At this pressure, the system turns nematic, as is indicated by the fact that the positional order parameter τ vanishes (see Fig. 6.10) but the orientational order parameter is non-zero. The director of the phase remains aligned with the z direction of the simulation box along the SmA phase; its direction is seen to change when the melting to the nematic phase takes place. The nematic phase is observed over a very short range of pressures. In particular, an isotropic fluid is observed at pressures below $P^* = 1.08$. Whether or not the nematic phase is actually stable at this temperature can only be

determined from free energy considerations. We have performed a second simulation series compressing the system from a low-density isotropic fluid configuration at pressure $P^* = 0.05$ up to $P^* = 1.16$. The isotropic phase develops nematic ordering at pressures above $P^* = 1.10$. As expected, we find histeresis around the I–N transition.

A very similar behaviour is found at $T^* = 1.5$. Expanding the system from the solid phase at $P^* = 10$, the bond orientational order parameter vanishes at pressure $P^* = 3.20$ but the positional order parameter, $\tau = 0.764(29)$, is still high, which indicates a solid-to-smectic transition. Smectic ordering is observed down to a pressure of $P^* = 1.55$, where the SmA phase becomes unstable against the N phase. At this temperature, the nematic range is slightly wider than that reported earlier for the isotherm $T^* = 1.25$. In particular, the nematic liquid gives way to an isotropic liquid at $P^* = 1.30$, this being accompanied by a discontinuous jump of the orientational order parameter to $S \approx 0$. According to our results, the system only develops nematic ordering above a certain temperature that sets the location of an I–N–SmA triple point. This point should be located around $T^* \approx 1.15$.

We infer from Fig. 6.10 that the nematic-to-smectic transition is first order along the isotherm $T^* = 1.25$. At this temperature, the positional order parameter τ seems to undergo a discontinuous jump at the transition. On the other hand, the N–SmA transition appears to proceed in a continuous way at a higher temperature of $T^* = 1.5$, as is inferred from the behaviour of τ in the neighbourhood of the transition. We recall that a similar behaviour was quoted before at even higher temperature ($T^* = 2$). According to these results, the HGOSW model exhibits a tricritical point ($T_{\rm tc}$) along the N-SmA coexistence line where the transition changes from being first order (if $T < T_{\rm tc}$) to continuous (if $T > T_{\rm tc}$). The tricritical point must be located somewhere in the range $1.25 \leq T^*_{\rm tc} \leq 1.50$.

The smectic range is seen to decrease with increasing temperature; as a consequence, one might anticipate that the SmA phase will disappear at high temperatures or high pressures. This should not be surprising considering that the repulsive interactions are expected to dominate over the attractions in the high-temperature regime. In this limit, the HGOSW model should behave in a similar way as it does the HGO model[7]. This point has been explicitly corroborated from simulations of HGOSW systems at $T^* = 3.75$ (Fig. 6.11). We start from a solid configuration at pressure $P^* = 15$ and expand the system in small pressure steps. Ψ_6 and τ are found to vanish

[7] As argued in previous chapters, no smectic behaviour is expected in a system of HGO molecules.

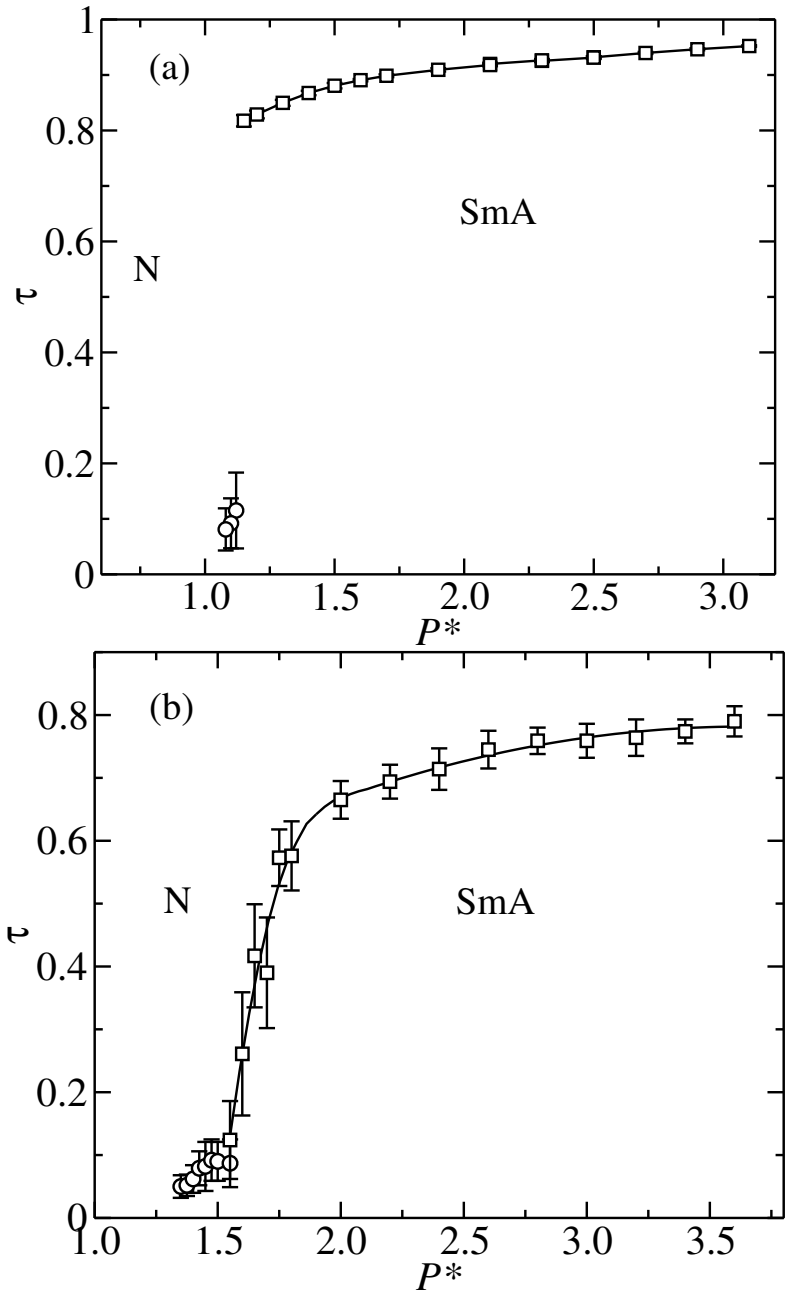

Figure 6.10: Variation of the positional order parameter τ with pressure in the region where the SmA–N transition takes place along the isotherms (a) $T^* = 1.25$, and (b) $T^* = 1.5$. The solid lines are a guide to the eye.

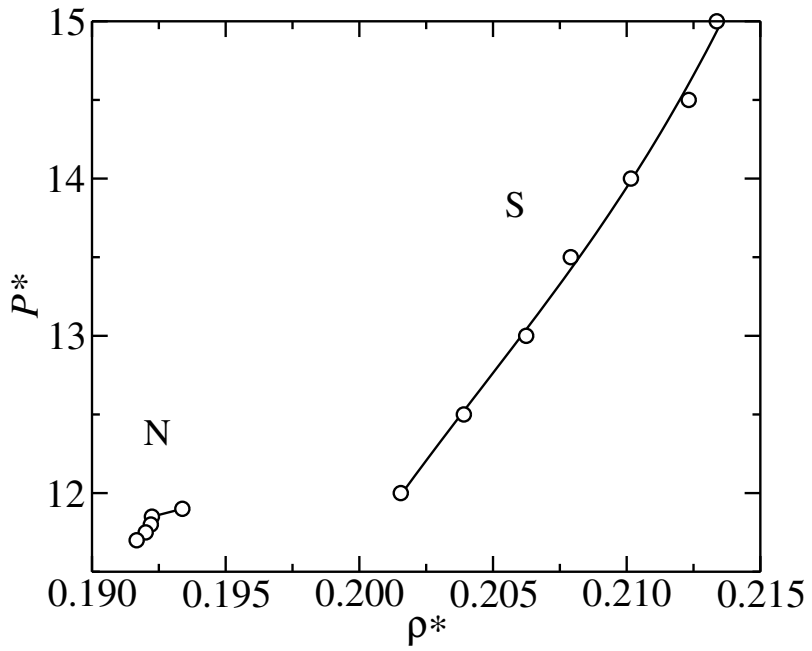

Figure 6.11: Pressure P^* vs density ρ^* at temperature $T^* = 3.75$. The pressure is expressed in units of $P^* = PD^3/\epsilon$, the density $\rho^* = \rho D^3$, and the temperature $T^* = k_{\rm B}T/\epsilon$. Solid lines are a guide to the eye.

simultaneously at $P^* = 11.70$, while S is non-zero. Thus, the solid has not melted into a SmA liquid, but into a nematic liquid. Further evidence follows from series of NPT simulations performed along constant-pressure paths. We show in Fig. 6.12 the simulation results obtained along the isobars $P^* = 8$, 10, and 12. In all cases, we start from a solid configuration[8] and heat the system in small steps in temperature, focusing on the solid-to-smectic transition. According to our results, the solid melts into a SmA fluid at temperature $T^* \approx 2.7$ ($P^* = 8$), and $T^* \approx 3.2$ ($P^* = 10$). At higher temperatures, the SmA phase melts into the nematic phase. At the highest pressure considered here ($P^* = 12$) the HGOSW solid does not melt into the smectic phase, but it does into a nematic liquid at $T^* = 3.7$. At this temperature, both Ψ_6 and τ jump simultaneously to zero in a discontinuous manner.

[8]We took care that these were well-equilibrated configurations deep in the solid phase, far from the transition

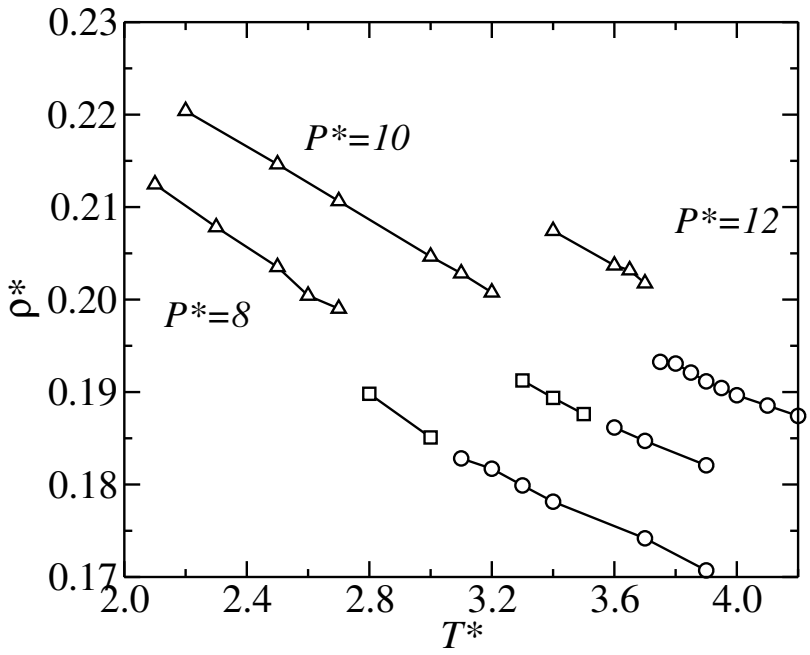

Figure 6.12: Variation of the number density ρ^* with temperature T^* along the isobars $P^* = 8$, 10, and 12 showing the solid (up triangles), smectic (squares), and nematic (circles) phases. The solid lines are a guide to eye.

6.6 Solid-smectic A transition

According to our simulation results, the solid-to-smectic transition is first order, as expected. In order to determine the SmA–S coexistence line in the P^*–T^* plane, we integrate the Clausius-Clapeyron equation along the coexistence line. As shown in §2.6.1 [cf. Eq. (2.69)], this equation can be written as

$$\frac{dP}{dT} = \frac{\Delta h}{T\Delta v} \equiv \Phi(P,T)\,, \tag{6.10}$$

where Δh and Δv are the change in enthalpy and volume per particle at the transition. We consider simultaneous NPT simulations of the two coexisting (SmA and S) phases consisting on 2×10^5 cycles for equilibration and 2×10^5 additional cycles to accumulate averages of h and v. The above first-order differential equation is numerically integrated by using a fourth-order Runge-Kutta algorithm. If ΔT is the integration temperature step, the solution can be expressed as [cf. Eq. (2.70)]

$$P_{\rm n} = P_{\rm o} + \frac{\Delta T}{6}(\Phi_1 + 2\Phi_2 + 2\Phi_3 + \Phi_4)\,,$$

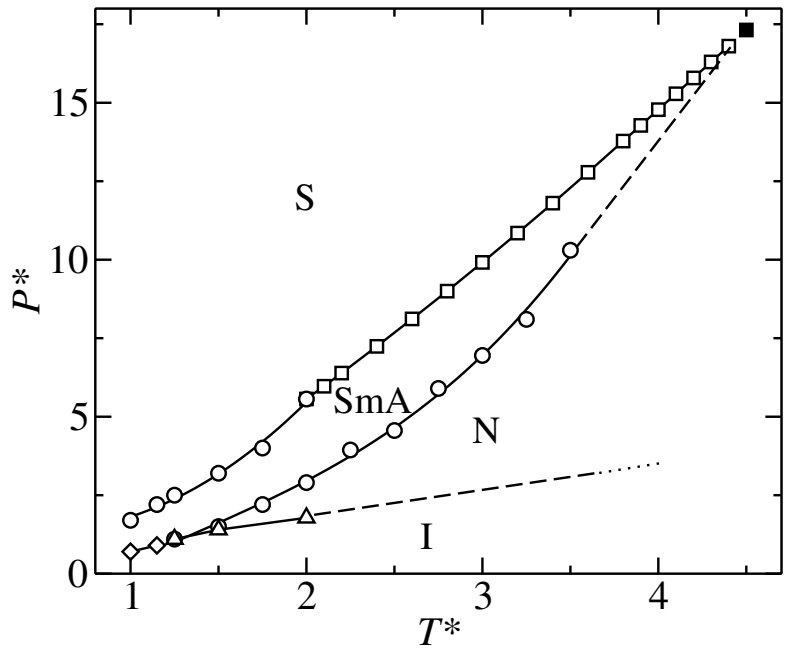

Figure 6.13: Partial phase diagram of the HGOSW model in the P^*–T^* plane showing the I–SmA, I–N, N–SmA, and SmA–S coexistence lines for molecular parameters $\kappa = 5$, and $\lambda^* = 1.5$. The filled square represents the S–SmA–N triple point.

where P_o and P_n are the old and new pressures at temperatures T_o and $T_\mathrm{n} = T_\mathrm{o} + \Delta T$, respectively. As explained in §2.6.1, Φ_i $(i = 1, \ldots, 4)$ are the right-hand side of Eq. (6.10) evaluated at appropriate temperatures (see further details in §2.6.1).

The starting point for the Gibbs-Duhem integration is chosen to be the SmA–S transition pressure at $T^* = 2$. The integration is performed by considering small temperature steps ΔT for increasing ($\Delta T > 0$). It is observed that the translational order parameter τ of the SmA phase decreases smoothly with increasing temperature along the coexistence line. At $T^* = 4.4$, τ vanishes but the system preserves the orientational order. This point sets the location of a S–SmA–N triple point: for higher temperatures, the SmA phase is no longer stable and the solid phase melts directly into the nematic phase. This finding may seems at odds with the data included by the end of the previous section. We claimed there that no SmA phase is observed at a temperature $T^* = 3.75$, which is below the quoted value of the triple-point temperature. There is no contradiction if one bears in mind that a solid can be overheated beyond the melting transition. As a result, the line that sets the limit of mechanical stability of the solid phase is shifted

towards higher temperatures relative to the actual coexistence line.

The simulation results obtained in this chapter for the HGOSW model with molecular parameters $\kappa = 5$, and $\lambda^* = 1.5$ are summarized in Fig. 6.13, where we show (a partial) phase diagram of the model in the P^*–T^* plane. In addition to the S-SmA coexistence line, we have included the line of N–SmA transitions as estimated from the pressure at which the transition takes place along different isotherms.

6.7 Conclusions

In the previous chapters we determined the phase diagram of the HGO model. It was concluded that the model exhibits isotropic, plastic solid, nematic, and solid phases depending on the molecular elongation. In this chapter we have focused on the effect of the attractive interactions, modelled by square-well interactions, on the phase behaviour of the HGO model. The temperature now enters into the description of the phase behaviour and, as a consequence, the stability of the different phases will depend on temperature. This study has been limited to the HGOSW model with molecular elongation $\kappa = 5$, and range of attractive interactions $\lambda^* = 1.5$. The phase sequence of the model has been investigated from NPT simulations performed along different isotherms. The simulations have consisted in expansion series from the solid phase down to low pressure, and compression from a low-pressure isotropic liquid. Additional simulations along different isobars have also been performed, where the phase sequence has been investigated by heating a solid configuration.

The most relevant feature of the HGOSW model is the presence of the smectic phase. The stability of this phase is entirely due to the attractive interactions. At temperatures below $T^* \leq 1.15$ the only stable phases are the isotropic, smectic, and solid phases. Above this temperature the nematic phase is stable between the isotropic and smectic phases. We conclude that the I-N-SmA triple point is located at $T^* \approx 1.15$. We have inferred from our results that the nematic-to-smectic transition changes from first order to continuous at a tricritical point located somewhere in between $1.25 \leq T_c^* \leq 1.50$. This point is such that the N–SmA transition is first order at lower temperatures and continuous above the tricritical temperature. Free energy calculations have been performed in the isotropic, nematic, smectic, and solid phases for the isotherm $T^* = 2$, and the corresponding first-order I–N and SmA–S transitions have been located by solving the coexistence conditions. Once the SmA–S transition has been located at this temperature, we have

used the Gibbs-Duhem integration method, considering the temperature as the integration variable, in order to obtain the SmA–S transition properties at high temperatures. We have established that the region of stability of the SmA phase is bounded by a S–SmA–N triple point, located at $T^* = 4.4$, and $P^* = 17.5$. At higher temperatures or pressures, smectic order is no longer promoted.

Chapter 7

Conclusions

The main conclusions of this investigation can be summarized as follows:

- Our investigation of the system-size dependence of the free energy of a hard-sphere solid allows us to conclude that this dependence is not weak, as claimed by some authors, but strong, as reported by others. A similar conclusion is seen to apply for a HGO molecular solid and, possibly, for most molecular solids.

- The dependence of the free energy of a solid with the particular (cubic vs non-cubic) shape of the simulation box is found to be negligible. We do find, however, a non-negligible dependence with the orientation of the close-packed planes with respect to the simulation box. Crystalline structures with tilted planes are found to yield higher values of the free energy than structures with dense planes parallel to the faces of the simulation box.

- We have carried out a thorough investigation of the phase behaviour of a molecular model (HGO) from computer simulation. The model only includes repulsive interactions. It is defined in terms of the distance of closest approach between a pair of molecules and depends on a single microscopic parameter, κ, related with the molecular anisotropy. The HGO model is expected to be qualitatively similar to the hard-ellipsoid model, though the mathematical form of the interactions are considerably simpler in the former.

- For small molecular anisotropies, the HGO model exhibits a plastic solid phase at intermediate pressures, and an orientationally ordered solid phase at higher pressures in addition to the low-density isotropic fluid phase. The various transitions are always found to be first order and their location is accomplished from the computation of the

free energy of all the phases. The integration of a generalized Clausius-Clapyeron equation has allowed us to establish the corresponding phase boundaries. We have found that the plastic solid phase becomes unstable for $\kappa \geq 1.43(1)$. The topology of the phase diagram in this region has been found to be very similar to that found for related hard-core models. This underlines the fact that in this region, the phase behaviour of hard-core models is mainly determined by the molecular anisotropy and not by the particular molecular shape.

– For large molecular anisotropies, the HGO model exhibits nematic behaviour. This is found to occur for $\kappa \geq 2.3$. The stability of the nematic phase relative to the solid has been proved from free energy calculations. Two crystalline structures have been considered. According to our simulation results, the ABC structure is more stable in the region where the solid melts into a nematic liquid. At higher pressures, the solid undergoes a weak first-order structural transition to a molecular solid with AB structure. The free energy difference between these structures is small but measurable within the precision of our free energy computations.

– The explicit consideration of attractive interactions in the HGO model results in the stabilization of the smectic phase. No smectic phase should be observed at sufficiently high temperatures or pressures, where the repulsive interactions dominate over the attractions. This has been explicitly demonstrated by showing that the region of stability of the smectic phase is bounded by an (upper) S–SmA–N triple point. Evidence has been given of the existence of another (lower) SmA–N–I triple point, below which the nematic phase becomes unstable.

From a methodological point of view, the most relevant aspects of this work can be summarized as follows.

– We have setup a full range of non-trivial simulation techniques for the calculation of free energies of fluid and solid phases from computer simulation, including thermodynamic integration, parametric integration, Einstein crystal, and particle-insertion. These have been applied to specific molecular models, but can be easily generalized to arbitrary interaction models. The coexistence boundaries of the models considered here have been established from the integration of a generalized Clausius-Clapeyron equation.

- We have made use of a general perturbative approach for the computation of the first-order derivative of the free energy with respect to an arbitrary parameter. The approach is based on the numerical estimate of the change in free energy associated with small variations of the parameter which in turn can be expressed as an ensemble average of the corresponding Boltzmann factor. This has been explicitly used here for the evaluation of the change in free energy under a change of the molecular elongation at constant pressure. This approach is particularly useful for molecular models with impulsive interactions, where the average of the Boltzmann factor can be expressed in terms of the average number of overlaps generated by the perturbation. This quantity is directly accesible in a simulation.

- A variant of the particle-insertion (Widom) method has been developed for the computation of the chemical potential. The method involves the generation of the molecular orientations of the ghost particles from a non-uniform distribution. The method has been shown to be efficient in the nematic phase, where the standard Widom method would fail, with increasing efficiency for larger molecular elongations. The implementation of this method has allowed us to assess the consistency of the free energy values obtained from other routes.

- A synthetic analysis has been devised for the estimation of the stastical uncertainties associated with free energy calculations from thermodynamic integration using fitted data. This procedure has allowed us to estimate the statistical uncertainties in the computed transition pressures.

- We have found that the systematic errors associated with the particular form of the fitting function used for the numerical integration of the compressibility factor can be large and may be even larger than the statistical uncertainties. The former can be made vanishingly small if the integration domain is restricted to values sufficiently close to the pressure (or density) of interest. This is particularly useful for fluid phases where the data are generally obtained from simulations performed over a wide range of thermodynamic conditions.

Appendix A

Free energy of the Einstein crystal

We consider here the derivation of the Helmholtz free energy of an atomic Einstein crystal (EC) at a fixed value of N, V, and T. For simplicity, we shall consider that all particles of the system are identical, with m being the mass. The potential energy is of the form

$$\mathcal{U}_{\mathrm{EC}}(\mathbf{r}^N;\lambda) = \lambda \sum_{i=1}^{N} (\mathbf{r}_i - \mathbf{r}_i^0)^2/D^2 \tag{A.1}$$

where D is some arbitrary length scale, $\mathbf{r}_i$ is the position of particle i, and $\mathbf{r}_i^0$ corresponds to the positions of the underlying lattice structure. The vectors $\mathbf{r}_i^0$ will be different for different crystalline structures.

The canonical partition function of the ideal EC is given by

$$Q_{\mathrm{EC}} = \frac{1}{h^{3N}} \int d\mathbf{p}^N \exp\left(-\beta \sum_{i=1}^{N} \frac{\mathbf{p}_i^2}{2m}\right) \int d\mathbf{r}^N \exp(-\beta \mathcal{U}_{\mathrm{EC}}) \tag{A.2}$$

The partition function can be expressed as $Q_{\mathrm{EC}} = P_{\mathrm{EC}} Z_{\mathrm{EC}}$, where P_{EC} and Z_{EC} are the kinetic and configurational contributions, respectively. The kinetic contribution can be expressed as a $3N$ multidimensional Gaussian integral. This yields

$$\begin{aligned} P_{\mathrm{EC}} &= \frac{1}{h^{3N}} \int d\mathbf{p}^N \exp\left(-\beta \sum_{i=1}^{N} \frac{\mathbf{p}_i^2}{2m}\right) \\ &= \left[\frac{1}{h} \int dp_x \exp\left(-\beta \frac{p_x^2}{2m}\right)\right]^{3N} = \left(\frac{2\pi m}{\beta h^2}\right)^{3N/2} = \frac{1}{\Lambda_t^{3N}} \end{aligned} \tag{A.3}$$

Similarly, the configurational contribution can be expressed as a $3N$ multidimensional Gaussian integral after changing to $\mathbf{R}_i = (\mathbf{r}_i - \mathbf{r}_i^0)/D$ ($d\mathbf{R}_i = d\mathbf{r}_i/D^3$). It then follows that

$$Z_{\rm EC} = \int d\mathbf{r}^N \exp\left(-\beta\lambda \sum_{i=1}^{N} (\mathbf{r}_i - \mathbf{r}_i^0)^2/D^2\right) = D^{3N} \int d\mathbf{R}^N \exp\left(-\beta\lambda \sum_{i=1}^{N} \mathbf{R}_i^2\right)$$
$$= \left[D \int dR_x \exp\left(-\beta\lambda R_x^2\right)\right]^{3N} = \left(\frac{\pi D^2}{\beta\lambda}\right)^{3N/2} \tag{A.4}$$

The reduced Helmholtz free energy of the ideal EC is thus given by

$$f_{\rm EC} = -\frac{3}{2}\ln\left(\frac{\pi D^2}{\Lambda_t^2 \beta\lambda}\right) = -\frac{3}{2}\ln\left(\frac{\pi}{\beta\lambda}\right)$$

where we have set Λ_t equal to the unit of length D.

As mentioned in the main text, it turns out to be more convenient to work under conditions of fixed center of mass. If $\mathbf{r}_{\rm CM}$ is used to denote the center of mass of the system, this constraint is expressed as

$$\mathbf{r}_{\rm CM} = \mathbf{r}_{\rm CM}^0 \tag{A.5}$$

where $\mathbf{r}_{\rm CM}$ is given by

$$\mathbf{r}_{\rm CM} = \frac{1}{N}\sum_{i=1}^{N} \mathbf{r}_i \tag{A.6}$$

and $\mathbf{r}_{\rm CM}^0$ is the center of mass of the underlying ideal lattice. The constraint on the center of mass poses an additional constraint on the total momemtum of the system. Differentiating Eq. (A.5) with respect to time, it follows that

$$\sum_{i=1}^{N} \mathbf{p}_i = \mathbf{0} \tag{A.7}$$

which expresses the fact that there is no overall translation of the system. Conditions given in Eqs. (A.5) and (A.7) pose restrictions on the kinetic and configurational contributions of the partition function. In particular, the kinetic contribution under the constraint on the momemtum is now given by[1]

$$P_{\rm EC}^{\rm CM} = \frac{1}{h^{3(N-1)}} \int d\mathbf{p}^N \exp\left(-\beta \sum_{i=1}^{N} \frac{\mathbf{p}_i^2}{2m}\right) \delta\left[\sum_{i=1}^{N} \mathbf{p}_i\right] \tag{A.8}$$

[1]Due to the constraint on the center of mass, the system loses 3 degrees of freedom. The total number of degrees of freedom of the system is no longer $3N$, but $3(N-1)$. This explains the new exponent that accompanies Planck constant.

Considering the Fourier representation of the delta function

$$\delta\mathbf{p} = \frac{1}{(2\pi)^3}\int d\mathbf{k}\exp\left(i\mathbf{k}\cdot\mathbf{p}\right)$$

Eq. (A.8) becomes

$$P_{\mathrm{EC}}^{\mathrm{CM}} = \frac{1}{h^{3(N-1)}}\frac{1}{(2\pi)^3}\int d\mathbf{p}^N\int d\mathbf{k}\exp\left[-\beta\sum_{i=1}^{N}\frac{1}{2m}\left(\mathbf{p}_i^2 - \frac{2im\mathbf{k}\cdot\mathbf{p}_i}{\beta}\right)\right] \tag{A.9}$$

The exponent in the above integral can be manipulated and written as a perfect square, which allows us to express the integral as a Gaussian integral. Noting that

$$\left(\mathbf{p}_i - \frac{im\mathbf{k}}{\beta}\right)^2 = \mathbf{p}_i^2 - \frac{2im\mathbf{k}\cdot\mathbf{p}_i}{\beta} - \frac{m^2\mathbf{k}^2}{\beta^2}$$

and introducing a new variable $\mathbf{f}_i$, defined as

$$\mathbf{f}_i \equiv \mathbf{p}_i - \frac{im\mathbf{k}}{\beta}$$

(note that $d\mathbf{f}_i = d\mathbf{p}_i$), allows us to express Eq. (A.9) as

$$P_{\mathrm{EC}}^{\mathrm{CM}} = \frac{1}{h^{3(N-1)}}\frac{1}{(2\pi)^3}\int d\mathbf{f}^N\exp\left(-\beta\sum_{i=1}^{N}\frac{\mathbf{f}_i^2}{2m}\right)\int d\mathbf{k}\exp\left(-\frac{mN}{2\beta}\mathbf{k}^2\right)$$

and we finally get

$$P_{\mathrm{EC}}^{\mathrm{CM}} = \frac{1}{h^{3(N-1)}}\left(\frac{2\pi m}{\beta}\right)^{3N/2}\left(\frac{\beta}{2m\pi}\right)^{3/2}\left(\frac{1}{N}\right)^{3/2} = P_{\mathrm{EC}}\Lambda_t^3\left(\frac{1}{N}\right)^{3/2} \tag{A.10}$$

where we have expressed $P_{\mathrm{EC}}^{\mathrm{CM}}$ in terms of P_{EC} as given in Eq. (A.3). Similarly, the configurational integral under the constraint on the center mass is given by

$$Z_{\mathrm{EC}}^{\mathrm{CM}} = \int d\mathbf{r}^N\exp\left(-\beta\lambda\sum_{i=1}^{N}\left(\mathbf{r}_i - \mathbf{r}_i^0\right)^2/D^2\right)\delta\left[\sum_{i=1}^{N}\left(\frac{1}{N}\right)\left(\mathbf{r}_i - \mathbf{r}_i^0\right)\right]$$

Changing variables to $\mathbf{R}_i = (\mathbf{r}_i - \mathbf{r}_i^0)/D$ ($d\mathbf{R}_i = d\mathbf{r}_i/D^3$), and using the Fourier representation of the delta function, the configurational integral becomes:

$$Z_{\mathrm{EC}}^{\mathrm{CM}} = \frac{D^{3N}}{(2\pi)^3}\int d\mathbf{R}^N\int d\mathbf{k}\exp\left[-\beta\lambda\sum_{i=1}^{N}\left(\mathbf{R}_i^2 - \frac{i\mathbf{k}\cdot\mathbf{R}_i}{\beta\lambda N}\right)\right] \tag{A.11}$$

Once again, writing the exponent as a perfect square allows us to express the above integral as a Gaussian integral. Noting that

$$\mathbf{R}_i^2 - \frac{i\mathbf{k}\cdot\mathbf{R}_i}{\beta\lambda N} = \left(\mathbf{R}_i - \frac{i\mathbf{k}}{2\beta\lambda N}\right)^2 + \frac{\mathbf{k}^2}{4\beta^2\lambda^2 N^2}$$

and considering a new variable $\mathbf{g}_i$, defined as

$$\mathbf{g}_i \equiv \mathbf{R}_i - \frac{i\mathbf{k}}{2\beta\lambda N}$$

($d\mathbf{R}_i = d\mathbf{g}_i$), allows us to write Eq. (A.11) as

$$Z_{\mathrm{EC}}^{\mathrm{CM}} = \frac{D^{3N}}{(2\pi)^3}\int d\mathbf{g}^N \exp\left(-\beta\lambda\sum_{i=1}^{N}\mathbf{g}_i^2\right)\int d\mathbf{k}\exp\left(\frac{-\mathbf{k}^2}{4\beta\lambda N}\right)$$

The configurational integral can be finally expressed as

$$Z_{\mathrm{EC}}^{\mathrm{CM}} = Z_{\mathrm{EC}}\left(\frac{\beta\lambda N}{\pi}\right)^{3/2} \tag{A.12}$$

where Z_{EC} is given by Eq. (A.4). From Eqs. (A.10) and (A.12), it follows that the reduced Helmholtz free energy of the ideal EC with fixed center of mass is given by

$$f_{\mathrm{EC}}^{\mathrm{CM}} = -\frac{3}{2}\ln\left(\frac{\pi}{\beta\lambda}\right) - \frac{3}{2N}\ln\left(\frac{\beta\lambda}{\pi}\right) \tag{A.13}$$

Bibliography

[1] M. P. Allen, G. T. Evans, D. Frenkel, and B. M. Mulder, *Adv. Chem. Phys.* **86**, 1 (1993).

[2] N. Metropolis, A. W. Rosenbluth, M. N. Rosenbluth, A. H. Teller, and E. Teller, *J. Chem. Phys.* **21**, 1087 (1953).

[3] B. J. Alder and T. E. Wainwrigh, *J. Chem. Phys.* **27**, 1208 (1957).

[4] M. P. Allen and D. J. Tildesley, *Computer Simulation of Liquids* (Clarendon Press, Oxford, 1987).

[5] P. J. Collings and M. Hird, *Introduction to liquid crystals* (Taylor & Francis, London, 1997).

[6] S. Singh, *Phys. Rep.* **324**, 107 (2000).

[7] P. G. de Gennes, *The Physics of Liquid Crystals* 2nd ed., (Clarendon, Oxford, 1993).

[8] L. Onsager, *Ann. N. Y. Acad. Sci* **51**, 627 (1949).

[9] W. Maier and A. Saupe, *Z. Naturforsch. A* **13**, 568 (1958); **14a**, 882 (1959) ; **15a**, 287 (1960).

[10] N. V. Madhusudana, *Theories of liquid crystals*, in B. Bahadur (ed.), Liquid Crystals: Applications and uses, vol. 1, (World Scientific, Singapore, 1990).

[11] D. Frenkel and B. M. Mulder, *Mol. Phys.* **55**, 1171 (1985).

[12] D. Frenkel, *J. Chem. Phys.* **92**, 3280 (1988).

[13] E. M. del Río and E. de Miguel, *Phys. Rev. E* **71**, 051710 (2005).

[14] M. J. Maeso and J. R. Solana *Mol. Phys.* **79**, 449 (1993).

[15] M. Rigby, *Mol. Phys.* **68**, 687 (1989).

[16] E. de Miguel and E. M. del Río, *J. Chem. Phys.* **115**, 9072 (2001).

[17] D. Frenkel and B. Smit, *Understanding Molecular Simulation* (Academic, New York, 1996).

[18] M. J. Newman and G. T. Barkema, *Monte Carlo Methods in Statistical Physics* (Clarendon Press, Oxford, 1999).

[19] M. H. Kalos and P. A. Whitlock, *Monte Carlo methods, vol. I* (John Wiley, New York, 1986).

[20] H. Müller-Krumbhaar and K. Binder, J. Stat. Phys. **8**, 1 (1973).

[21] H. Flyvbjerg and H. G. Petersen, J. Chem. Phys. **91**, 461 (1989).

[22] A. P. Lyuvartsev, A. A. Martsinovski, S. V. Shevkunov, and P. N. Vorontsov-Vel'yaminov, *J. Chem. Phys.* **96**, 1776 (1992).

[23] B. Widom, *J. Chem. Phys.* **39**, 2808 (1963).

[24] W. H. Press, B. P. Flannery, S. A. Teukolsky, and W. T. Vetterling, *Numerical Recipes* (Cambridge University, Cambridge, 1986).

[25] J. Chang, A. M. Lenhoff, and S. I. Sandler, *J. Chem. Phys.* **120**, 3003 (2004).

[26] E. de Miguel and R. G. Marguta, E. M. del Río, *J. Chem. Phys.*, **127**, 154512 (2007).

[27] A. P. Lyuvartsev, A. Laaksonen, and P. N. Vorontsov-Vel'yaminov, *Mol. Phys.* **82**, 455 (1994).

[28] A. P. Lyuvartsev, A. Laaksonen, and P. N. Vorontsov-Vel'yaminov, *Molec. Simulat.* **18**, 43 (1996).

[29] M. K. Tej and J. C. Meredith, *J. Chem. Phys.* **117**, 5443 (2002).

[30] N. B. Wilding and M. Muller, *J. Chem. Phys.* **101**, 4324 (1994).

[31] F. A. Escobedo and J. J. de Pablo, *J. Chem. Phys.* **103**, 2703 (1995).

[32] A. P. Lyuvartsev, O. K. Forrisdahl, and A. Laaksonen, *J. Chem. Phys.* **108**, 227 (1998).

[33] E. de Miguel, *J. Chem. Phys.* **129**, 214112 (2008).

[34] W. G. Hoover and F. H. Ree, *J. Chem. Phys* **49**, 3609 (1968).

[35] W. G. Hoover, M. Ross, K. W. Jhonson, D. Henderson, J. A. Barker, and B. C. Brown, *J. Chem. Phys.* **52**, 4931 (1970).

[36] W. G. Hoover, S. G. Gray, and K. W. Jhonson, *J. Chem. Phys.*, **55**, 1228 (1971).

[37] D. Frenkel and A. J. C. Ladd, *J. Chem. Phys.* **81**, 3188 (1984).

[38] J. M. Polson, E. Trizac, S. Pronk, and D. Frenkel, *J. Chem. Phys.* **112**, 5339 (2000).

[39] C. Vega and E. G. Noya, *J. Chem. Phys*, **127**, 154113 (2007).

[40] N. G. Almarza, *J. Chem. Phys*, **126**, 211103 (2007).

[41] N. B. Wilding, *Comp. Phys. Comm.* **146**, 99 (2002).

[42] N. B. Wilding and A. D. Bruce, *Phys. Rev. Lett.* **85**, 5138 (2000).

[43] D. A. Kofke, *Mol. Phys.* **78**, 1331 (1992).

[44] D. A. Kofke, *J. Chem. Phys.* **98**, 4149 (1993).

[45] P. J. Camp, *Phys. Rev. E.* **67**, 011503 (2003).

[46] M. Lisal, K. Aim, and J. Fischer, *Mol. Sim.* **23**, 363 (2000).

[47] D. L. Pagan and J. D. Gunton, *J. Chem. Phys.* **122**, 184515 (2005).

[48] H. Liu, S. Garde, and S. Kumar, *J. Chem. Phys.* **123**, 174505 (2005).

[49] P. J. Camp, C. P. Mason, M. P. Allen, A. A. Khare, and D. A. Kofke, *J. Chem. Phys.* **105**, 2837 (1996).

[50] P. J. Camp and M. P. Allen, *J. Chem. Phys.* **106**, 6681 (1997).

[51] H. -S. Nam, M. I. Mendelev, and D. J. Srolovitz, *Phys. Rev. B* **75**, 014204 (2007).

[52] J. M. Polson and D. Frenkel, *J. Chem. Phys.* **109**, 318 (1998).

[53] J. M. Polson and D. Frenkel, *J. Chem. Phys.* **111**, 1501 (1999).

[54] M. H. Lamm and C. K. Hall , *Fluid Phase Equilibria* **194-197**, 197 (2002).

[55] A. Galindo, C. Vega, E. Sanz, L. G. McDowell, E. de Miguel, F. J. Blas, *J. Chem. Phys.* **120**, 3957 (2004).

[56] M. R. Hitchcock and C. K. Hall, *J. Chem. Phys.* **110**, 11433 (1999).

[57] A. Z. Panagiotopoulos, *J. Phys. Condens. Matter* **12**, R25 (2000).

[58] W. W. Wood and J. D. Jacobson, *J. Chem. Phys.* **27**, 1207 (1957).

[59] E. G. Noya, C. Vega, and E. de Miguel, *J. Chem. Phys.* **128**, 154507 (2008).

[60] R. L. Davidchack and B. B. Laird, *J. Chem. Phys.* **108**, 9452 (1998).

[61] A. J. C. Ladd and L. V. Woodcock, *Chem. Phys. Lett.* **51**, 155 (1977).

[62] J. N. Cape and L. V. Woodcock, *Chem. Phys. Lett.* **59**, 271 (1978).

[63] J. Chang and S. I. Sandler, *J. Chem. Phys.* **125**, 054705 (2006).

[64] J. Chang, A. M. Lenhoff and S. I. Sandler, *J. Phys. Chem. B* **109**, 19507 (2005).

[65] J. Chang and S. I. Sandler, *J. Chem. Phys.* **118**, 8390 (2003).

[66] A. D. Bruce, N. B. Wilding, and G. J. Ackland, *Phys. Rev. Lett.* **79**, 3002 (1997).

[67] A. D. Bruce, A. N. Jackson, G. J. Ackland, and N. B. Wilding, *Phys. Rev. E* **61**, 906 (2000).

[68] P. G. Bolhuis, D. Frenkel, S.-C. Mau, and D. A. Huse, *Nature* (London) **388**, 235 (1997).

[69] C. Vega, E. Sanz, J. L. F. Abascal, and E. G. Noya, *J. Phys. Condens. Matter*, **20**, 153101 (2008).

[70] P. Bolhuis and D. Frenkel, *J. Chem. Phys.* **106**, 666 (1997).

[71] S. Pronk and D. Frenkel, J. Chem. Phys. **110**, 4589 (1999).

[72] L. V. Woodcock, Nature (London) **384**, 141 (1997).

[73] E. de Miguel and E. M. del Río, *J. Chem. Phys.* **118**, 1852 (2003).

[74] J. P. Hansen and I. R. McDonald, *Theory of Simple Liquids* (Academic, London, 1986).

[75] C. Vega, E. P. A. Paras, and P. A. Monson, *J. Chem. Phys.* **96**, 9060 (1992).

[76] C. Vega, E. P. A. Paras, and P. A. Monson, *J. Chem. Phys.* **97**, 8543 (1992).

[77] S. J. Singer and R. Mumaugh, *J. Chem. Phys.* **93**, 1278 (1990).

[78] J. A. C. Veerman and D. Frenkel, *Phys. Rev. A* **41**, 3237 (1990).

[79] T. Boublik, *Mol. Phys.* **42**, 209 (1981).

[80] G. A. Few and M. Rigby, *Chem. Phys. Lett.* **20**, 433 (1973).

[81] D. Frenkel, B. Mulder, and J. P. McTague, *Phys. Rev. Lett.* **52**, 287 (1984).

[82] D. Frenkel, *Comp. Phys. Comm.* **44**, 243 (1987).

[83] M. P. Allen, *J. Mol. Liq.* **85**, 161 (2000).

[84] B. J. Berne and P. Pechukas, *J. Chem. Phys.* **56**, 4213 (1972).

[85] V. R. Bhethanabotla and W. Steele, *Mol. Phys.* **60**, 249 (1987).

[86] J. G. Gay and B. J. Berne, *J. Chem. Phys.* **74**, 3316 (1981).

[87] Y. Singh, *Phys. Rev. A* **30**, 583 (1984).

[88] U. P. Singh and Y. Singh, *Phys. Rev. A* **30**, 2725 (1986).

[89] C. Zannoni, in *The molecular Physics of liquid crystals*, edited by G. R. Luckhurst and G. W. Gray (Academic New York, 1979), p. 191.

[90] K. J. Strandburg, in *Bond-orientational Order in Condensed Matter Systems* , edited by K. J. Strandburg (Springer New York, 1992), Chap2.

[91] M. A. Bates and G. R. Luckhurst, *J. Chem. Phys.* **110**, 7087 (1999).

[92] J. R. Errington , *J. Chem. Phys.* **120**, 3130 (2004).

[93] J. Vieillard-Baron, *J. Chem. Phys.* **56**, 4729 (1972).

[94] J. Vieillard-Baron, *Mol. Phys.* **28**, 809 (1974).

[95] A. Stroobants, H. N. W. Lekkerkerker, and D. Frenkel, *Phys. Rev. A* **36**, 2929 (1987).

[96] A. Stroobants, H. N. W. Lekkerkerker, and D. Frenkel, *Phys. Rev. Lett* **57**, 1452 (1986).

[97] E. de Miguel, L. F. Rull, M. K. Chalam, and K. E. Gubbins, *Mol. Phys.* **74**, 405 (1991).

[98] E. de Miguel, E. M. del Río, J. T. Brown, and M. P. Allen, *J. Chem. Phys.* **105**, 4234 (1996).

[99] J. T. Brown, M. P. Allen, E. M. del Río, and E. de Miguel, *Phys. Rev. E* **57** 6685 (1998).

[100] E. de Miguel and C. Vega, *J. Chem. Phys.* **117** 6313 (2002).

[101] S. C. McGrother, D. C. Williamson and G. Jackson, *J. Chem. Phys.* **104**, 6755 (1996).

[102] R. Holyst and A. Poniewierski, *Mol. Phys.* **68**, 381 (1989).

[103] P. Padilla and E. Velasco, *J. Chem. Phys.* **106**, 10299 (1997).

[104] W. L. McMillan, *Phys. Rev. A* **4**, 1238 (1971).

[105] R. G. Marguta, E. Martín del Río, and E. de Miguel *J. Phys. Condens. Matter* **18**, 10335 (2006).

[106] J. W. Doane, R. S. Parker, and B. Cvikl, *Phys. Rev. Lett.* **26**, 1694 (1972).

[107] A. M. Somoza and P. Tarazona, *Phys. Rev. A* **41**, 965 (1990).

[108] A. Poniewierski and R. Holyst, *Phys. Rev. A* **41**, 6871 (1990).

[109] A. Poniewierski and T. J. Sluckin, *Phys. Rev. A* **43**, 6837 (1991).

[110] A. Poniewierski, *Phys. Rev. A* **45**, 5605 (1992).

[111] H. Xu, H. N. W Lekkerkerker, and M. Baus, *Europhys. Lett.* **17**, 163 (1992).

[112] M. P. Taylor, R. Hentschke, and J. Herzfeld, *Phys. Rev. Lett.* **62**, 1989 (1989).

[113] B. Tjipto-Margo and G. T. Evans, *Mol. Phys.* **74**, 85 (1991).

[114] P. I. C. Texeira, *Mol. Phys.* **92**, 167 (1997).

[115] D. C. Williamson, *Mol. Phys.* **95**, 319 (1998).

[116] D. C. Williamson and F. del Río, *J. Chem. Phys.* **109**, 4675 (1998).

[117] D. C. Williamson and Y. Guevara, *J. Phys. Chem. B* **103**, 7522 (1999).

[118] E. Garcia, D. C. Williamson, and A. Martinez-Richa, *Mol. Phys.* **98**, 179 (2000).

[119] S. Varga, D. C. Williamson, and I. Szalai, *Mol. Phys.* **96**, 1695 (1999).

[120] E. de Miguel and M. P. Allen, *Mol. Phys.* **76**, 1275 (1992).

[121] E. de Miguel and E. M. del Río, *Phys. Rev. Lett.* **95**, 217802 (2005).